Visual Comfort Control Strategy for an Advanced Fenestration System in an Office Space

Iheb Ben Sassi

A Thesis
in the Department
of
Building, Civil and Environmental Engineering

Presented in Partial Fulfillment of the Requirements
for the Degree of Master of Applied Science (Building Engineering) at

Concordia University

Montréal, Québec, Canada

June 2024

CONCORDIA UNIVERSITY

School of Graduate Studies

This is to certify that the thesis prepared

By: Iheb Ben Sassi

Entitled: Visual Comfort Control Strategy for an Advanced Fenestration System in an Office Space

and submitted in partial fulfillment of the requirements for the degree of

Master of Applied Science (Building Engineering)

complies with the regulations of the University and meets the accepted standards with respect to originality and quality.

Signed by the final Examining Committee:

Hua Ge ______________________________ Chair

Caroline Hachem-Vermette ________________ Examiner

______________________________________ Examiner

Andreas Athienitis & Mohamed Ouf __________ Supervisor

Approved by ____ Chair of Department or Graduate Program Director

____ Dean of Faculty

Date 08/24/2024__________________________________

Abstract

Visual Comfort Control Strategy for an Advanced Fenestration System in an Office Space.

Iheb Ben Sassi

Because of the current trends in buildings which favor a higher window to wall area ratio, the impact of fenestration on the indoor environment has become crucial. New technologies appearing in the market make windows an active tool in controlling visual and thermal comfort, while allowing for energy generation through renewable sources such as photovoltaics.

The goal of this study is to present a control strategy for an integrated venetian blinds system within a triple glazed window with bifacial silicon photovoltaic cells on the outer glazing to optimize occupant visual comfort within a one-person office space. To achieve this, four objectives were considered. First, a visual transmittance model was developed to mimic the real-life behavior of the window under clear and cloudy conditions. The model was then integrated into a control strategy that uses the fenestration as an active tool for ensuring optimal visual comfort for office related activities, while reducing the energy used for heating by controlling passive solar gains. The control strategy determines the optimal blind tilt angle at each time step based on the outdoor climate conditions and occupancy schedule of the space. Next, the model and control strategy output were validated using measured data from an outdoor test-room representing an office space in Montreal, Quebec. Finally, a sensitivity analysis was conducted to determine the impact of physical parameters of the indoor environment on the visual comfort of the occupants. The window to wall ratio, the reflectance of the surfaces, and the room geometry were analyzed through simulation.

Using the control strategy, the results show that under clear sky conditions, the space can be self-sufficient in terms of illuminance levels but deals with certain levels of glare throughout the day. However, even though glare is imperceptible throughout the occupancy period under cloudy sky conditions, the illuminance levels do not reach the required 300 lux threshold for 23% of the day, requiring the integration of an artificial lighting source to fill in the missing gap to achieve the needed levels. In terms of physical properties of the space, it was found that an increase in the

room dimensions leads to a decrease in illuminance levels, while a decrease in window to wall ratio also has the same impact. The surfaces reflectance also affects visual comfort, since highly reflective surfaces increase the work plane illuminance compared to more opaque surfaces. Overall, the control strategy presented in this work can be scalable and applicable to any type of office space that uses a similar advanced fenestration system.

Acknowledgments

I would like to start by thanking my advisors, Dr. Mohamed Ouf and Dr. Andreas Athienitis for their guidance and their support throughout this research journey. Their expertise and input were essential to completing this work and helped me grow as an engineer. I appreciate their effort to assist me grow in a field that is new to me and expand my horizons through constant encouragement and motivation.

I would also like to extend my gratitude to Dr. Michael Kim and Dr. Jiwu Rao for assisting me in the experimental portion of this research. Their help in implementing the experimental setup and conducting the experimental procedures is greatly appreciated and their feedback was essential to obtain the results shown in this work.

I would also like to thank my fellow students in the CZEBS offices for their continuous support. These amazing people helped create a comfortable and positive work environment where everyone can achieve their full potential. Specifically, I am thankful for the support of Anna-Maria Sigounis and Harry Vallianos for giving me constant feedback on my work and for their continuous support as researchers and as friends.

Completing this degree would not have been possible without the financial and technical support of MITACS national research organization. I am grateful to them for putting me in touch with my advisors before the beginning of my master's degree.

Finally, and most importantly, I would like to thank my parents, Najmeddine and Rabaa, and my brother Adam, for their unconditional support throughout the whole journey. Their love and encouragement helped me focus on my goals when things got difficult. I would also like to show appreciation to the good friends I made in Montreal for believing in me and motivating me.

Table of Contents

List of Figures x

List of Tables xiii

Nomenclature xiv

Acronyms xiv

Greek Letters xvi

Symbols xvii

1. Chapter 1: Introduction 1

1.1- Overview 1

1.2- Motivation 3

1.3- Goal and Objectives 4

1.4- Outline 5

2. Chapter 2: Literature Review 7

2.1- Advanced Fenestration Systems 7

2.1.1- Definition and Examples 7

2.1.2- Complex Solar Shading Devices 8

2.1.3- Dynamic Shading Devices 10

2.1.4- Design Considerations 10

2.2- Building Integrated Photovoltaic 14

2.2.1- Definition and Types 14

2.2.2- Electrical and Thermal Implications of BIPV Windows 18

2.2.3- Building Integrated Photovoltaics with Thermal Recovery 20

2.2.4- Design Considerations 22

2.3- Quantifying Visual Comfort 24

2.3.1- Types of Light 24

2.3.2- Light Assessment 26

2.3.3- Daylighting Metrics 27

2.3.4- Glare Metrics 30

2.4- Shades Control Strategy 33

2.4.1- Classical and Advanced Control 33

2.4.2- Open Loop Control Strategies 34

2.4.3- Visual Comfort Centric Control Strategies 36

2.5- Research Gaps 39

3. Chapter 3: Methodology 41

3.1- Case Study 41

3.1.1- Office Space 41

3.1.2- Fenestration 43

3.1.3- Experimental Setup 45

3.2- Modeling the Transmittance 50

3.2.1- Data Driven Models 51

3.2.2- Model Derived from Previous Literature 54

3.2.3- Root Mean Square Error 58

3.3- Daylight Calculations 59

3.3.1- Sun Position Calculations 60

3.3.2- Incident Daylight Calculations 61

3.3.3- Transmittance and Transmitted Daylight Calculations 63

3.3.4- Radiosity Analysis 63

3.3.5- Work Plane Illuminance Calculations 65

3.3.6- Simplified Daylight Glare Probability Calculations 66

3.4- Control Strategy 68

3.4.1- Description 69

3.4.2- Flowchart 74

3.4.3- Control Strategy applied to the Case Study: 75

3.5- Parametric Variation 77

4. Chapter 4: Results 80

4.1- Daylighting Trends 80

4.1.1- Clear Sky 80

4.1.2- Cloudy Sky 82

4.2- Transmittance Model Validation 84

4.2.1- Clear Conditions Transmittance Model Validation 84

4.2.2- Cloudy Conditions Transmittance Model Validation 87

4.3- Control Strategy Results 90

4.3.1- Clear Sky Conditions 90

4.3.2- Cloudy Sky Conditions 92

4.4- Parametric Effect on Visual Comfort 94

4.4.1- Window to Wall Ratio 95

4.4.2- Room Dimensions 96

4.4.3- Reflectance of the Opaque Surfaces 98

5. Chapter 5: Discussion 100

5.1- Transmittance Trends under Clear Sky Conditions 100

5.2- Clear Sky Transmittance Model 105

5.3- Dimming Light Approach 108

5.4- Impact of Other Parameters on Visual Comfort 109

6. Chapter 6: Conclusion 110

6.1- Contributions 111

6.2- Limitations 112

6.3- Future Work 113

7. References 115

8. Appendix 129

Appendix A: Experimental Results 129

Appendix B: Sun Position Calculations Code Sample 136

Appendix C: View Factor & Configuration Factor Calculations 138

Appendix D: Incident and Transmitted Daylight Calculations 142

Appendix E: Control Strategy Sample Code 145

List of Figures

Figure 1.1: Global Share of energy consumption and emissions per sector (Source: United Nations Environment Programme, 2020) 1

Figure 2.1: Daily heating demand [KWh] (left) and minimum mean radiant temperature [°C] (right) for different glazing types on a cloudy day (Source: Bessoudo et al., 2010) 9

Figure 2.2: Trend line of the energy demand of heating and air conditioning with WWR (Source: Ma et al., 2023) 12

Figure 2.3: Simulated single person office space with a three-section façade (Robinson & Athienitis, 2009) (left) Configuration of a BIPV window with c-Si spaced cells (Park et al., 2010) (right) 17

Figure 2.4: Effects of semi-transparent BIPV windows application (Ng et al., 2013) 19

Figure 2.5: Schematic Diagram of a building integrated PV with thermal recovery from the inside environment (left) and outside environment (right) (Quesada et al., 2012) 21

Figure 2.6: Annual bifacial gain and equivalent cell efficiency as a function of ground clearance for various system designs (Kreinin et al., 2016) 23

Figure 2.7: The reference terrestrial solar spectrum in comparison with the extraterrestrial spectrum and the theoretical black body spectrum (Dirnberger, 2015). 25

Figure 2.8: Diagram of Open-loop and Closed-loop control algorithms (Tabadkani et al., 2020). 35

Figure 2.9: Flowchart of a simple venetian blinds control strategy based on glare metrics (Chan & Tzempelikos, 2013). 38

Figure 3.1: Concordia University's Future Buildings Lab (Baril, 2023) 42

Figure 3.2: Three-dimensional schematic of Test cell 4 at the FBL building. 43

Figure 3.3: Frontal view of the outer glazing with measurements in millimeters (Source: Canadian Solar) (left) and Transversal view of the advanced fenestration system (right) 44

Figure 3.4: Images of the pyranometer and photometer used in the experimental setup (LI-COR, Inc., 2022a; LI-COR, Inc., 2022b). 46

Figure 3.5: Outer glazing experimental setup in test cell 4 (left) and simplified diagram (right). 48

Figure 3.6: Inner glazing experimental setup in test cell 4 (left) and simplified diagram (right).49
Figure 3.7: Floor plan experimental setup in test cell 4 (left) and simplified diagram (right). ... 50
Figure 3.8: Refraction diagram for light traveling through silicon (right) and through glass (left) 55
Figure 3.9: Sun position and incident daylight calculations flowchart...................................... 59
Figure 3.10: Two-dimensional surface breakdown of a reference office space. 65
Figure 3.11: Correlation between DGP and vertical illuminance at eye level (Wienold, 2007). 67
Figure 3.12: Simplified flowchart of the control strategy. 69
Figure 3.13: Control strategy process. 74
Figure 3.14: Two-dimensional surface breakdown of the studied office space. 75
Figure 3.15: Position of the occupant within the office space.. 77
Figure 4.1: Evolution of the transmittance with respect to the blind tilt angle for different intervals of the incidence angle under clear conditions... 81
Figure 4.2: Evolution of the transmittance with respect to the incidence angle for different blind tilt angles under clear conditions. 82
Figure 4.3: Evolution of the transmittance with respect to the blind tilt angle for different intervals of the incidence angle under cloudy conditions.. 83
Figure 4.4: Experimental and theoretical work plane illuminance from developed model as a function of time for blind tilt angles of 0 degrees and 50 degrees under clear conditions. 85
Figure 4.5: Experimental and theoretical work plane illuminance from previous literature models for blind tilt angles of 0 and 50 degrees under clear conditions. 86
Figure 4.6: Experimental and theoretical work plane illuminance from developed model as a function of time for blind tilt angles of 0 degrees and 80 degrees under cloudy conditions. 88
Figure 4.7: Experimental and theoretical work plane illuminance from previous literature models for blind tilt angles of 0 and 80 degrees under cloudy conditions. 88
Figure 4.8: work plane illuminance on a clear day in the office space with the control strategy applied. 91
Figure 4.9: simplified daylight glare probability on a clear day in the office space with the control strategy applied. 91
Figure 4.10: Optimal blind tilt angle on a clear day in the office space with the control strategy applied. 92

Figure 4.11: work plane illuminance on a cloudy day in the office space with the control strategy applied. 93

Figure 4.12: simplified daylight glare probability on a cloudy day in the office space with the control strategy applied. 93

Figure 4.13: Optimal blind tilt angle on a cloudy day in the office space with the control strategy applied. 94

Figure 4.14: work plane illuminance for different WWR on a clear day with the applied control strategy. 95

Figure 4.15: simplified daylight glare probability for different WWR on a clear day with the applied control strategy 96

Figure 4.16: work plane illuminance for different room dimensions on a clear day with the applied control strategy 97

Figure 4.17: simplified daylight glare probability for different room dimensions on a clear day with the applied control strategy. 98

Figure 4.18: work plane illuminance for different surface reflectance on a clear day with the applied control strategy 99

Figure 4.19: simplified daylight glare probability for different surface reflectance on a clear day with the applied control strategy. 99

Figure 5.1: Evolution of the transmittance with respect to θ for small blind tilt angles under clear conditions. 101

Figure 5.2: Evolution of the transmittance with respect to θ for large blind tilt angles under clear conditions. 102

Figure 5.3: Output of the Wilk-Shapiro test conducted for the different blind tilt angles under clear conditions. 106

Figure 5.4: Experimental work plane illuminance for a 70 degrees blind tilt angle under clear conditions. 107

Figure 6.1: Thermal sensation scale (left) and PPD based on the PMV curve (right). (Source: ASHRAE, 2017). 113

List of Tables

Table 3.1: Properties of the photometer and pyranometer used in the experimental phase (LI-COR, Inc., 2022a; LI-COR, Inc., 2022b). 47

Table 3.2: Daylight glare comfort classes. 68

Table 3.3: Reflectance of different building elements in the test cell. 76

Table 3.4: Physical parameter variation summary. 79

Table 4.1: RMSE values between the experimental and theoretical results of the work plane illuminance (in lux) for different blind tilt angles under clear sky conditions. 87

Table 4.2: RMSE values between the experimental and theoretical results of the work plane illuminance (in lux) for different blind tilt angles under cloudy sky conditions. 89

Table 5.1: Results of the Wilk-Shapiro test. 107

Nomenclature

Acronyms

AFS	Advanced Fenestration System
ASE	Annual Sunlight Exposure
AST	Apparent Solar Time
a-Si	Amorphous Silicon Solar Cells
BAPV	Building Attached Photovoltaic
BIPV	Building Integrated Photovoltaic
BIPV/T	Building Integrated Photovoltaic with Thermal Recovery
CdTe	Cadmium Telluride
CIE	International Commission on Illumination
CIGS	Copper, Indium, Gallium and Selenium
CGI	CIE Glare Index
CO_2	Carbon Dioxide
CS_{model}	Control strategy based on data-driven transmittance model
CS_{lit}	Control strategy based on literature derived transmittance model
c-Si	Crystalline Silicon Solar Cells
DGI	Daylight Glare Index
DGP	Daylight Glare probability
DSSC	Dye-sensitized solar cell
ET	Equation of time
FF	Fill Factor
GHG	Green House Gazes
h	Hour Angle
HDR	High Dynamic Range
HISG	Heat Insulation Solar Glass
HVAC	Heating, Ventilation, and Air Conditioning
LAT	Latitude

LEED	Leadership in Energy and Environmental Design
LON	Longitude
Low e	Low Emissivity
LSM	Local Standard Meridian
LST	Local Sidereal / Standard Time
MPC	Model Predictive Control
MVB	Motorized Venetian Blinds
n	Day of the year
NIR	Near Infrared
PF	Packing Factor
PID	Proportional Integral Derivative
PMV	Predicted Mean Vote
PPD	Predicted Percentage of Dissatisfied
PV	Photovoltaic
RH	Relative Humidity
RMSE	Root Mean Square Error
SGHC	Solar Gain Heat Coefficient
ST-BIPV	Semi-Transparent Building Integrated Photovoltaic
STC	Standard Test Conditions
STPV	Semi-Transparent Photovoltaic
T-BIPV	Transparent Building Integrated Photovoltaic
TMY	Typical Meteorological Year
UDI	Useful Daylight illuminance
UGR	Unified Glare Rating
UV	Ultraviolet
U-value	Thermal transmittance $[\frac{w}{m^2 \cdot K}]$
WWR	Window to Wall Ratio

Greek Letters

α	Solar altitude angle
α_{PV}	Temperature coefficient of power for a PV cell / module
a	Absorption
θ	Theta – Incidence angle of the sun
θ'	Refraction angle
η	Eta – Efficiency
η_{PV}	Eta – Efficiency of a PV cell / module
η_{STC}	Eta – Efficiency of a PV cell / module under standard test conditions
β	Beta – Blind tilt angle
β_{opt}	Beta – Optimal blind tilt angle
β_{window}	Beta – Window tilt angle
ε	Epsilon – Emissivity
δ	Delta – Declination angle
φ	Phi – Solar azimuth angle
γ	Gamma – Solar surface azimuth angle
ω_s	Solid angle
Ω_s	the solid angle modified by Guth's position index [sr]
ϕ	Phi – Solar azimuth angle
ψ	Psi – Surface azimuth

Symbols

$A_{PV}, A_{silicon}$	Area covered in photovoltaics
A_{glass}	Area covered in glass
$A_{glazing}$	Area of the glazing
$\tau_{clear,middle\ glazing}$	Visual transmittance model for the middle part of the window on clear days.
$\tau_{cloudy,middle\ glazing}$	Visual transmittance model for the middle part of the window on cloudy days.
τ_{glass}	Visual transmittance of the glass
$\tau_{lit,clear}$	Visual transmittance model obtained from literature under clear conditions.
$\tau_{lit,cloudy}$	Visual transmittance model obtained from literature under cloudy conditions.
τ_{middle}	Visual transmittance of the middle window
$\tau_{model,clear}$	Data driven visual transmittance model under clear conditions
$\tau_{model,cloudy}$	Data driven visual transmittance model under cloudy conditions
τ_{outer}	Visual transmittance model for the outer part of the window on clear days.
$\tau_{silicon}$	Visual transmittance of silicon
k	Absorption coefficient
ρ	Reflectivity
ρ_g	Reflectance of the ground
c	Optical atmospheric extinction coefficient
c_{pi}	Configuration factor between point p and surface i
cDA	Continuous daylight autonomy
d	Profile angle
d	Thickness
d'	Effective thickness
D	Daylight Factor

DA	Daylight Autonomy
$DGPs$	Simplified Daylight Glare Probability
E_d	Direct vertical illuminance at the eye [lux]
E_{ground}	Daylight reflected off the ground [lux]
E_h	Horizontal Illuminance
$E_{h,\ global\ indoor}$	Indoor global horizontal illuminance [lux]
$E_{h,\ global\ outdoor}$	Outdoor global horizontal illuminance [lux]
$E_{h,sky}$	Horizontal illuminance due to the sky [lux]
$E_{h,sun}$	Solar horizontal illuminance [lux]
$E_{h,total}$	Total horizontal illuminance [lux]
E_i	Indirect vertical illuminance at the eye [lux]
$E_{incident,clear}$	Incident daylight on a clear day [lux]
$E_{incident,cloudy}$	Incident daylight on a cloudy day [lux]
$E_{middle\ transmitted,clear}$	Transmitted daylight through the middle window on a clear day [lux]
$E_{middle\ transmitted,cloudy}$	Transmitted daylight through the middle window on a cloudy day [lux]
E_o	Average illuminance on a surface oriented directly towards the sun, just outside the Earth's atmosphere [lux]
E_{sky}	Daylight reflected and diffused in the atmosphere [lux]
E_{sun}	Daylight directly from the sun [lux]
$E_{transmitted}$	Transmitted daylight through the PV windows [lux]
E_p	Work plane Illuminance at point p [lux]
E_v	Vertical Illuminance [lux]
E_{ref}	Overall Irradiance on the building facade
f	Correction factor to account for the elliptical shape of the Earth's orbit around the sun
F	View factor
G	Incident solar irradiation $[\frac{w}{m^2}]$

I	Identity matrix
Int	Light intensity $[\frac{lumens}{m^2}]$
I_{sc}	Short circuit current
L_b	Background luminance $[\frac{cd}{m^2}]$
L_s	Luminance of source $[\frac{cd}{m^2}]$
M	Final luminous exitance matrix [lux]
M_0	Initial luminous exitance matrix [lux]
n	Refraction index
P	Position index
P_{max}	Maximum power point
$Power$	Luminous flux [lumens]
q	Heat flux density $[\frac{w}{m^2}]$
$q_{without\ sun}$	Heat flux density at the center of the window without the sun $[\frac{w}{m^2}]$
$q_{with\ sun}$	Heat flux density at the center of the window with the sun $[\frac{w}{m^2}]$
r	Distance from the source [m]
sDA	Spatial daylight autonomy
t	Thickness
t'	Effective thickness
T	Radiosity matrix
T_e	Exterior ambient temperature [°C]
T_i	Interior ambient temperature [°C]
T_{PV}	PV cell / module temperature [°C]
V_{oc}	Open circuit voltage
W_B	Blind Slat Width
W_G	Glazing Spacing

1. Chapter 1: Introduction

1.1- Overview

Buildings play an essential role in separating the outdoor climatic conditions and the indoor environment to ensure the occupant comfort and safety. The building sector contributes to 35% of the final global energy consumption and 38% of the total greenhouse gas GHG emissions according to the United Nations Environment Programme (2020). On a local level, the Canadian building sector is the third highest source of emissions (Natural Resources Canada, 2023a) and represents 31% of the national energy consumption (Natural Resources Canada, 2016), with 73% of that energy being used for space heating, space cooling, and artificial lighting. With the government aiming to reach net-zero emissions in the building sector by 2050 under the Canada Green Buildings Strategy (Natural Resources Canada, 2023b), improvements must be made to reduce energy consumption and/or increase efficiency. Figure 1.1 summarizes the energy consumption and the subsequent emissions of major sectors.

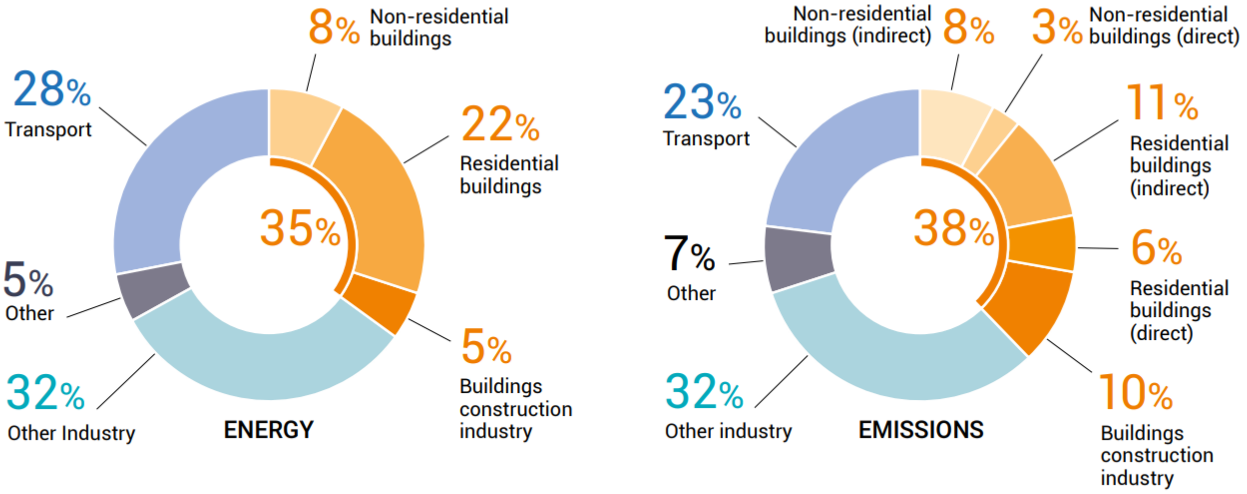

Figure 1.1: *Global Share of energy consumption and emissions per sector (Source: United Nations Environment Programme, 2020)*

One approach is to improve the components of the building envelope, like fenestration, either by introducing retrofits that will transform them into energy generation tools or by introducing automatic controls of their respective shading device. In fact, control for windows and more specifically shading devices can be a solution to reduce energy consumption in buildings (Yun, Yoon, and Kim, 2014) for multiple reasons. First and foremost, current trends in building development favor a bigger window area, meaning that the latter has a more significant impact on the indoor environment. The standard in building design assumes a window to wall ratio (WWR) of 40% (ASHRAE, 2022), but actual construction projects stride for higher WWR for aesthetic purposes.

Furthermore, carefully selected fenestration and their respective shading can be used as tools to control the visual and thermal comfort of the indoor space (Evola, Gullo, & Marletta, 2017). They allow for the utilization of passive solar space heating and natural lighting (Kunwar et al., 2020). The evolution in shading devices for windows and automatic control of those devices makes it easier to control the amount of light that penetrates the space, ensuring that the occupants are comfortable visually and thermally. This also reduces the demand on the HVAC system of the building and allows more control to be given to the occupants based on their schedules and their occupancy patterns, which in turn translates to significant savings in electricity consumption for lighting and heating (Tzempelikos and Athienitis, 2002).

Finally, innovations in the field have transformed windows into tools for energy production, notably through building-integrated photovoltaics (BIPV). They are an emerging PV technology where the cells replace pre-existing building materials and are integrated within the envelope (Jelle & Breivik 2012). Semi-transparent photovoltaics (STPV) are a subset of BIPVs which have a non negligeable transmittance (light can pierce through) which makes them ideal for fenestration design. These systems serve both as partial shades and as sources of electricity directly where needed (Shirazi et al., 2019), without the need for transportation of the produced energy with cables. Mende et al. (2011) highlight how BIPV technologies impact the energy requirements for building heating, cooling, and lighting, highlighting its considerable influence on reducing overall energy consumption.

In summary, the energy performance of buildings can be improved through controls and retrofits of windows that allow them to become tools of energy generation, while also enhancing the quality of the indoor environment.

1.2- Motivation

In order to study the advantages of advanced fenestration technology and its impact on visual comfort, models that mimic the real-world behavior of these windows need to be developed. Previous transmittance models shown in literature do not account for the advancements we see in the field today because the combination of number of glazing, type of solar cell integrated in the glazing, and shading device used makes every case specific, with its unique visual and thermal properties . In a review of transparent and semi-transparent BIPV for fenestration applications, Romaní et al. (2022) concluded that there is a large gap in research regarding the evaluation of the impact of ST-BIPV and T-BIPV on thermal and visual comfort, with most models focusing on heat transfer and energy generation. In consequence, there is a lack of results regarding the impact of shading device control strategies for these advanced fenestrations, especially in the case where the aforementioned device is integrated between the different layers of glazing.

Therefore, the study conducted in this thesis is unique because it addresses a type of fenestration combination unaddressed in previous research: a triple glazed window with bi-facial silicon photovoltaic cells on the outer glazing and inter-pane venetian blinds. The transmittance equations presented target this specific type of window to predict the impact of the incidence angle of the sun and the blind tilt angle of the blinds on the evolution of the transmitted daylight throughout the day. The model can then be used to anticipate the energy generation from the PV cell, the impact of the heating effect on the latter, or the impact of this fenestration on the thermal comfort of the occupants.

Furthermore, based on the obtained model, a control strategy is presented to optimize the visual comfort within the indoor environment of a single person office space based on the outdoor conditions and the occupancy schedule for sunny and cloudy periods. This adds to the relevancy of the work as there is a gap regarding control strategies for advanced fenestration technologies, especially in the case where the considered venetian blinds are internal to the system. In addition, Jain & Garg (2018) state that further research needs to be considered for shading device control strategies during cloudy skies.

In summary, this project aims to add a transmittance model for an advanced fenestration to the body of literature. This model can be integrated into other projects such as a control strategy similar to the one presented in this work, which uses these developed models to enhance the visual comfort within an office space.

1.3- Goal and Objectives

The goal of this paper is to develop a control strategy for a triple glazed south facing window with integrated bi-facial silicon photovoltaic cells with inner-pane venetian blinds in a single person office space in Montreal that prioritizes visual comfort and maximizes passive solar heating gains.

- **Objective 1:** Develop a transmittance model for an advanced fenestration system based on a case study

The first objective is to develop a transmittance model for the fenestration based on experimental data from an outdoor test-room at the Future Buildings Laboratory (FBL) of Concordia University. This model accounts for the variations of the transmittance tau based on the blind tilt angle beta and the incidence angle theta of the sun for sunny time steps. It is then validated using experimental results from a test site representing a single person office space located in Montreal, Quebec, and its accuracy is quantified using the work plane illuminance as a metric for visual comfort. This office serves as a reference site to assess the transmittance model and control approach outcomes. Experimental data from this location is collected to adjust the model, confirm the transmittance's accuracy, and simulate the control strategy to evaluate its effect on visual comfort in a real single-person office.

- **Objective 2:** Develop a control strategy for an office space to optimize visual comfort and reduce energy consumption.

The second objective is to develop a control technique that automates the choice of the blind tilt angle at each 15-minute time step based on multiple factors: the outdoor conditions (cloudiness level, position of the sun etc.), occupancy schedule of a reference office space, and indoor visual level quantifiers. In this case, the two main quantifiers used are the work plane illuminance and the simplified daylight glare probability. The aim of the control strategy is to primarily prioritize visual comfort while also reducing heating energy consumption. In terms of comfort, low glare and high illuminance establish a comfortable environment, thus the hyperparameter optimization of these two indices becomes a tradeoff which determines the optimal tilt angle of the blinds. In terms of passive heating, the transmitted daylight can be used to reduce energy consumption when the office space is not occupied.

- **<u>Objective 3:</u>** Investigate the impact of physical parameters on the performance of the control strategy.

The final objective is to analyze how different physical parameters of the indoor environment can have an impact on the visual comfort. The three variables investigated are the window to wall ratio (WWR), the room size, and the reflectance of the different surfaces within the space. Different variations of these parameters are simulated to present their impact on the work plane illuminance and the simplified daylight glare probability.

1.4- Outline

The thesis is structured into six chapters, with each chapter summarized as follows:

<u>Chapter 1: Introduction</u> – The introduction gives a general overview of the problem that this work aims to solve. It provides information regarding the relevancy of the results compared to the current body of literature as well as the motivation behind it. The objectives of the project and a general outline are also provided.

<u>Chapter 2: Literature review</u> – The literature review explores relevant topics in the current body of knowledge. Special interest is given to: Advanced fenestration technologies and their advantages, building integrated photovoltaics (and more specifically semi-transparent BIPVs on windows), visual comfort metrics that help quantify the efficiency and the accuracy of models and

strategies, and control strategies' impact on comfort level and energy consumption.

Chapter 3: Methodology – The first part of the methodology provides information regarding the specific office space used as reference and fenestration technology considered, as well as details regarding the experimental setup used to obtain data from the test cell. The next part focuses on how the transmittance models were derived and evaluated. The following two sub-sections are dedicated to the daylight equations used and the control strategy developed using the daylighting equations. The final part focuses on the physical parameter's variation.

Chapter 4: Results – Divided into four parts, the first part discusses the trends concluded from the experimental data regarding the impact of the incidence angle and the blind tilt angle on the transmittance. The next subsection validates the transmittance model using experimental data. The next part discusses the results from implementing the control strategy and compares it to different baseline scenarios. It is also tested under different climatic conditions. The final section focuses on the impact of different space parameters on the output of the control strategy.

Chapter 5: Discussion – The discussion section will further elaborate on the different topics discussed in the results section, mainly regarding the daylighting trends observed. A subsection is dedicated to the Shapiro-Wilk test to test the accuracy of the derived transmittance model.

Chapter 6: Conclusion – The conclusions summarizes the work, provides its contributions within the current body of literature, discusses its limitations that may have caused potential errors, and analyzes potential opportunities for future work.

2. Chapter 2: Literature Review

The objective of this section is to review current research in the field of advanced fenestration systems (AFS), building integrated photovoltaics, visual comfort metrics, and shading device control strategies to position this project within the already established framework and to understand which gaps it will fill.

2.1- Advanced Fenestration Systems

2.1.1- Definition and Examples

Advanced fenestration systems are defined as systems that respond to the basic functionalities of a regular window such as minimizing heat transfer and regulating view to the outside, while also regulating these functions into more sophisticated solutions to ensure optimally controlled, indoor comfort for the occupants and to improve the energy performance of buildings in a context where carbon-neutral structures are becoming the aim (Favoino et al., 2022). There are multiple types of AFS used in buildings because advanced windows are one of the key components being deployed for low-energy structure strategies, especially in modern architecture where the glazing coverage is large (Ming et al., 2024).

Some examples of AFS are smart windows which can adapt to the needs of the indoor space based on the outdoor environment or occupant input (Wong and Chan, 2014). The most common examples of smart windows are electrochromic windows and thermochromic windows. The first is user controlled and changes transmittance using electrical current, and the second is triggered by outdoor conditions to regulate near infrared (NIR) light while allowing visible light to pierce through (Cui et al., 2018). There are multiple advantages to this type of fenestration, most notably their low cost, their energy saving potential, and the fact that they are fully material driven (Ke et al.,2019).

Another type of advanced fenestration system is the vacuum insulated glazing. The inner-glazing cavity is evacuated in this technology, making the fluid convection and conduction within the window insignificant (Cuce & Riffat, 2015). This results in a reduction of heat transfer as radiation becomes the unique theoretical way for heat to move through the window, thus reducing the buildings energy consumption for heating and cooling (Fang et al., 2007). In addition, this technology can be coupled with other advanced fenestration systems such as the previously mentioned smart windows. However, some disadvantages of this technology involve the short-term performance and the high cost of manufacturing (Favoino et al., 2022).

2.1.2- Complex Solar Shading Devices

These examples illustrate the idea that advanced fenestration systems are diverse and can cater to specific cases based on need. However, since the studied fenestration in this thesis includes integrated PV cells and inter-pane shading devices, the focus of this section will be shifted towards AFS that includes one or both of these components. Fenestrations that include a shading component are called a complex solar shading system, and windows with venetian blinds are part of this category. Many studies have been conducted regarding the advantages of integrating these designs in the building envelope on occupant comfort and energy savings.

Tzempelikos & Athienitis (2007) presented a simulation-based study on the impact of window to wall ratio (glazing area), shading device, and shading / artificial lighting control on the building cooling and lighting demand for an office space located in Montreal. For a window to wall ratio of 30% The results show a roller-shade with a transmittance of 20%, coupled with a control strategy, leads to a decrease of 50% in the annual cooling energy demand, and a total energy demand decrease by 12%. Reduction in consumption is further accentuated when a dimming artificial light control strategy is introduced in the space.

Bessoudo et al. (2010) developed a two-node thermal comfort model to evaluate the impact of the outdoor climatic conditions on interior thermal conditions and thermal comfort during winter days. Different types of glazing (different number of glazings, with or without low e, with or without a shading device) have been tested for sunny and cloudy days. The results show that the choice of glazing type is a trade-off between thermal comfort, visual comfort, and energy consumption. However, the integration of a shading device will always improve the performance of the fenestration. Figure 2.1 shows the daily heating demand and the minimum mean radiant temperature. Note that glazing 1 refers to an uncoated double glazing, glazing 2 refers to a double glazing with low-e coating ($\varepsilon = 0.1$), and glazing 3 refers to a triple glazing with low-e coating ($\varepsilon = 0.05$).

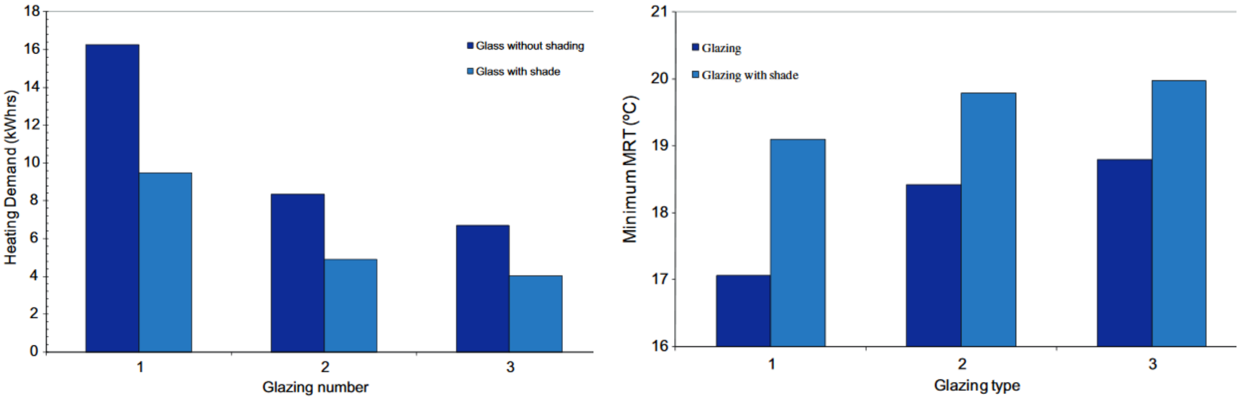

Figure 2.1: *Daily heating demand [KWh] (left) and minimum mean radiant temperature [°C] (right) for different glazing types on a cloudy day (Source: Bessoudo et al., 2010)*

The two above studies show that there is significant energy saving potential for using shading devices, whether it is exterior or interior to the AFS. The reason behind it is the strong influence of windows on the convective heat transfer rate between the outdoor and indoor environment. Studies have shown that shading devices reduce convection. Naylor et al. (2007) conducted an experiment to study the convective heat transfer within a double-glazed window with inter-pane aluminum Venetian blinds using the laser interferometry with the objective of using the obtained data as validation for future numerical models and to optimize inter-pane window designs. The results show that the heat transfer between the outer glazing and inner glazing is highest when the blinds are open and lowest when the blinds are closed. However, closed blinds do not create a complete partition due to imperfections in design. Overall, the presence of inter-pane blinds reduces the overall convective heat transfer compared to a traditional window. It is important to note that the window considered in this study has a blind slat width equal to the glazing spacing ($\frac{W_B}{W_G} = 1$), similar to the window considered in this project.

2.1.3- Dynamic Shading Devices

In addition, dynamic shading devices, like venetian blinds, are preferred over more conventional static shading devices. They refer to conventional technologies like venetian blinds and louvres that can be located on the inner side, outer side, or between the panes of the window (Lee et al., 1998). In a study conducted by Sanati and Utzinger (2013), the impact of a window with both a static (light shelf on the top half) and dynamic (venetian blinds on the bottom half) on occupant overall comfort was assessed. The results show that occupants prefer movable systems where their preference can be accounted for. Furthermore, it was also noted that the illuminance in the indoor space can be very low during overcast days because of the light shelf. These are some of the reasons why static shades are no longer considered in energy efficient building design (Al-Masrania and Al-Obaidi, 2019). Dynamic shading devices are becoming the norm. And one of the main reasons for this switch is the fact that control strategies can be implemented on dynamic shades to automate them based on factors like outdoor conditions, space usage, occupancy schedules, … Another reason is that dynamic shades allow the occupant to take advantage of the benefits of the winter sun on indoor illuminance while blocking the direct summer sun (Feng et al., 2021).

2.1.4- Design Considerations

Design considerations for fenestration systems are complex and not well defined due to the extensive list of design criteria such as aesthetics, visual and thermal comfort, and energy savings (Feng et al., 2021). Choices regarding the geometry (orientation, size, WWR), glazing (U-value, solar gain heat coefficient, glazing type), and shading (shading technique, shading control) need to be made depending on the overall objective of the project (Kuhn, 2017). Some of these design considerations, explored in previous research, will be discussed in this section. Since shading devices, and more specifically venetian blinds, have been mentioned in section 2.1.2, the focus will be more on the geometry and glazing criteria.

Window orientation is defined as the direction to which the window is facing. The choice of the orientation depends on the design objective of the fenestration. For example, Lu & Law (2013) studied the energy generation potential of BIPV on windows in a high-rise office building in Hong Kong and concluded that the optimal orientation is South-East facing if the objective is to prioritize energy production. At the same time, Robinson & Athienitis (2009) concluded that the optimal orientation to optimize daylight usage was South for a three-section façade where the top section was covered in semi-transparent photovoltaics. Other parameters need to be considered while choosing the orientation based on location and climatic conditions.

The window to wall ratio (WWR) is another important design consideration. It is presented as a percentage and is calculated using Equation 2-1:

$$WWR = \frac{Window\ Area}{Wall\ Area} \cdot 100 \tag{2-1}$$

Standards regarding the optimal WWR vary according to the space used. For office spaces, ASHRAE 90.1 (2016) states that a small office space (area of 464.5 m^2 or less) should have a maximum WWR of 19%, medium office spaces (area of 464.5 m^2 to 4,645.2 m^2) should have a maximum WWR of 31%, and large office spaces (area of 4,645.2 m^2 or greater) should have a maximum WWR of 40%. Research shows that the WWR has an impact on the heating and cooling loads of a space. Ma et al., (2023) assessed the evolution in the heating and cooling loads with reference to the window to wall ratio for three different Chinese cities having different climates. The results conclude that the heating and cooling energy demands vary linearly with WWR for all three climates, with the cooling load seeing a more dramatic change compared to its heating counterpart. The outdoor conditions affect the rate of change. Figure 2.2 shows the trend lines for heating and cooling demand with respect to WWR. For reference, the cities of Harbin and Beijing are considered a "very cold climate" while the city of Chengdu is referred to as a "cold climate".

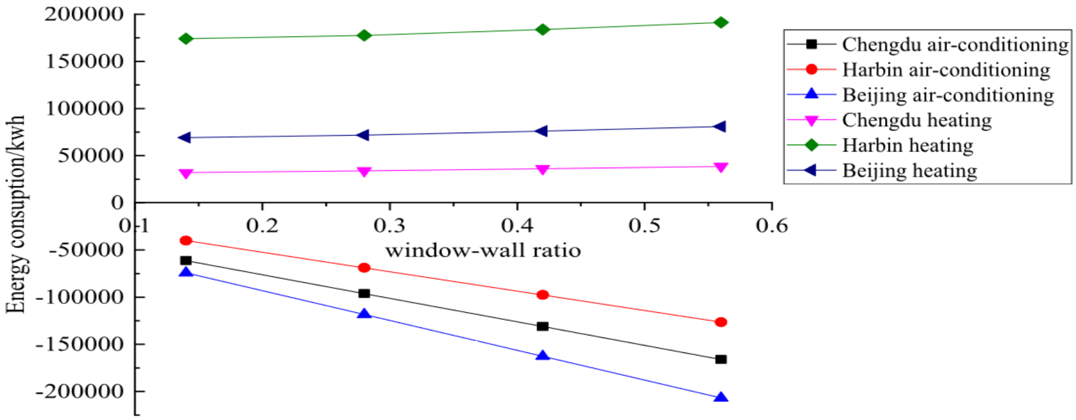

Figure 2.2: *Trend line of the energy demand of heating and air conditioning with WWR (Source: Ma et al., 2023)*

Another important aspect to consider when optimizing the fenestration used in a building is the glazing properties such as the U-value and the solar heat gain coefficient SHGC. The SHGC is defined as the ratio of solar heat gain entering through the fenestration product (including both directly transmitted solar heat and absorbed solar radiation that is re-radiated, conducted, or convected into the space) to the solar radiation striking the fenestration product (National Fenestration Rating Council, 2017). SHGC can be considered for the entire façade of a building, for a specific component of the façade (just the window for example), or for a sub-component (the glazing of the window excluding the frame). The effective heat gain coefficient for the center of the window is calculated using Equation 2-2:

$$SHGC = \frac{q_{with\ sun} - q_{without\ sun}}{E_{ref}} \qquad (2\text{-}2)$$

Where $q_{with\ sun}$ is the heat flux density $[\frac{W}{m^2}]$ with the sun shining at the center of the window and $q_{without\ sun}$ is the heat flux density without the sun. E_{ref} is the overall irradiance on the building façade.

U-value, or the thermal transmittance is another indicator of how much heat transfer is conducted through the building envelope components. It quantifies the rate at which heat moves through a material or barrier, factoring in the area and the temperature difference between the outer and inner side of the material. Calculated under steady-state conditions, this metric is essential for evaluation of a systems insulation effectiveness (BSI, 2014). According to ISO 9869-1, the U-value is calculated using Equation 2-3:

$$U_{value} = \frac{q}{(T_i - T_e)} \tag{2-3}$$

With q the heat flux density $[\frac{W}{m^2}]$, T_i the interior ambient temperature in Kelvin and T_e the exterior ambient temperature in Kelvin.

Envelope components with a lower heat transmittance help reduce energy consumption in buildings in cold climates because it translates into an increased insulation from the outdoor weather conditions (Aguilar-Santana et al., 2020). With windows having the highest U-value compared to other building elements like floors, roofs, and walls (Jelle et al., 2012), it becomes essential to improve fenestration in cold climate areas by decreasing their heat transmittance through the addition of extra glazing, shading devices, or special coatings. Aguilar-Santana et al. (2020) compared the thermal transmittance of multiple novel windows that utilized different compositions, gas cavities, and materials using the ISO 98691:2014 heat flow meter method. The results show that window's U-values significantly vary according to construction. For example, a double-glazed window with Argon gas filled gap reduces the thermal transmittance by 44% compared to the same window with air filled gap. The study reports that the optimal values were obtained for the granulated aerogel glazing and the vacuum gap glazing.

Another study by Cuce et al. (2014) studied the heat transmittance properties of heat insulation solar glass (HISG) which the authors define as "transparent amorphous silicon (a-Si) PV module equipped with various coatings and structures". Similar to the studied semi-transparent PVs studied in this project, HISG is a cost-effective approach to reducing the thermal transmittance of the window and providing an on-site energy generation tool. The results of the study show that the average U-value of HISG is around 1.1 $\frac{W}{m^2 \cdot K}$, which is close to that of a triple glazed window.

Furthermore, under an irradiance of 850 $\frac{W}{m^2}$, 0.66 m^2 of these windows were able to generate around 40 Watts of power. However, these results were obtained under laboratory conditions within a controlled environment and through simulation. It is expected that the performance would be less ideal in a real-life scenario when the window is subject to outdoor climate variations.

Overall, advanced fenestration systems have become a core interest in building engineering research due to their numerous advantages. Multiple window types fall under the AFS umbrella, which allows designers to choose the optimal one based on their objective. With the appropriate design considerations, AFS allow fenestration to become a tool for energy generation and an essential part of net-zero building design.

2.2- Building Integrated Photovoltaic

Before discussing BIPVs, an important distinction must be made between building integrated photovoltaics and building attached photovoltaics (BAPV). The latter describes arrays that are added to the building as a separate component, without affecting the structure's functional aspects (Barkaszi & Dunlop, 2001). This section will focus uniquely on BIPVs, their applications, their types, and their impact on the operation of buildings.

2.2.1- Definition and Types

Building integrated photovoltaics are defined as PV cells or arrays that are incorporated directly into the different building components as an integral part serving as both power generators and elements of the architectural design, while seamlessly blending with structure's aesthetic without appearing out of place (Henemann, 2008). They can be placed on any part of the structure, but most applications consider BIPVs on the building's façade or roof to optimize energy production.

There are multiple categorizations that can be made. A popular one is based on solar cell types, which categorizes them based on whether the P-N junction is silicon based and non-silicon based (Biyik et al., 2017). Silicon based cells include amorphous silicon and crystalline silicon (both mono-crystalline and poly-crystalline), while non-silicon based include perovskite, Dye-sensitized solar cell (DSSC), Cadmium telluride (CdTe), and CIGS solar cells.

Perovskite solar cells can be integrated to windows because they possess tuneable transparency, which makes them a potential shading tool (Ghosh, 2022). A study conducted by Cannavale et al. (2017) analyzed the energy and thermal comfort performance of a semi-transparent building integrated perovskite cells under different weather conditions and window to wall ratios. The studied cells / window had a conversion efficiency η equal to 6.64% and a visual transmittance of 42.4%. The results show that in terms of visual comfort, just like other PV windows, perovskite cells provided adequate levels of daylight glare probability (DGP) and useful daylight illuminance (UDI). The values of DGP did however increase when considering a larger WWR. In terms of energy production, the annual energy produced from the cells could cover the total energy used for artificial lighting, with the heating effect having little to no impact on the efficiency of the perovskite cells. The authors conclude that perovskite BIPVs are a valid solution to overcome the functional and aesthetic issues that arise from using silicon-based PVs.

Dye-sensitized solar cells are another type of non-silicon cells that can be used in window integration because of their transparency and cheap fabrication cost (Gong et al., 2012), but the usage of liquid electrolyte can lead to issues when exposed to extreme outdoor weather conditions such as freezing under extremely low temperatures and expanding under extremely high temperatures (Richhariya et al., 2017). The transmittance of these cells greatly depends on their thickness, with τ varying between 6% and 30% based on thickness in a study conducted by Kang et al. (2013). Another study analyzed the visual comfort of DSSC BIPV with three different transmittance levels and concluded that glare can be reduced by 21% for a DSSC cell with τ equal to 37%, compared to a regular double-glazed window (Selvaraj et al., 2019).

Cadmium Telluride solar cells are another option for BIPV. Five different CdTe based BIPV with different visual transmittances (varying between 0.07 and 0.327) were analyzed using experimental and simulated data by Barman et al. (2018). It was concluded that transmittance, window orientation, and WWR play an important role in determining the amount of energy savings that can be obtained. A maximum of 60.4% reduction in energy consumption was obtained for the highest efficiency CdTe cells window compared to a reference low e window.

Copper, Indium, Gallium and Selenium (CIGS) cells are another alternative for BIPVs. This thin film technology is gaining popularity in research due to the low-cost fabrication and nontoxicity compared to other non-silicon-based cells, but the low efficiency makes its commercial deployment on a larger scale more difficult (Ghosh, 2022). A study conducted by Kong et al. (2020) quantified the relative competitiveness of different BIPVs on a scale based on economic, aesthetic, energy efficient, and innovative indices. The results show that CIGS-BIPVs score relatively high with 86/100, close to Silica-based BIPVs which received a score of 86.20/100.

However, the silicon based solar cells represent the most studied type for building integrated PVs (Yu et al., 2021). There are two types of cells in this category: the crystalline silicon cells (c-Si), which can be both mono-crystalline and poly-crystalline, and the amorphous silicon cells (a-Si). The first one is used because of its high efficiency, reaching up to 26.7% ± 0.5 based on the version 57 of the solar cell efficiency table developed by Green et al. (2020). The long-term resilience of crystalline silicon (c-Si) in extreme outdoor conditions, combined with its well-established technology, positions it as an ideal choice for BIPV systems (Ghosh, 2022). However, this cell is considered as opaque with a visual absorption of around 90.5% (Santbergen & Van Zolingen, 2008), therefore, for BIPV integration, glass spacing between the different cells is needed for light to transmit into the indoor space. An application of c-Si is common in three section facades as seen in Figure 2.3, where the upper third is covered by spaced PV cells, the middle third is the viewing section with a shading device, and the bottom third is an opaque section that covers the space below the work plane.

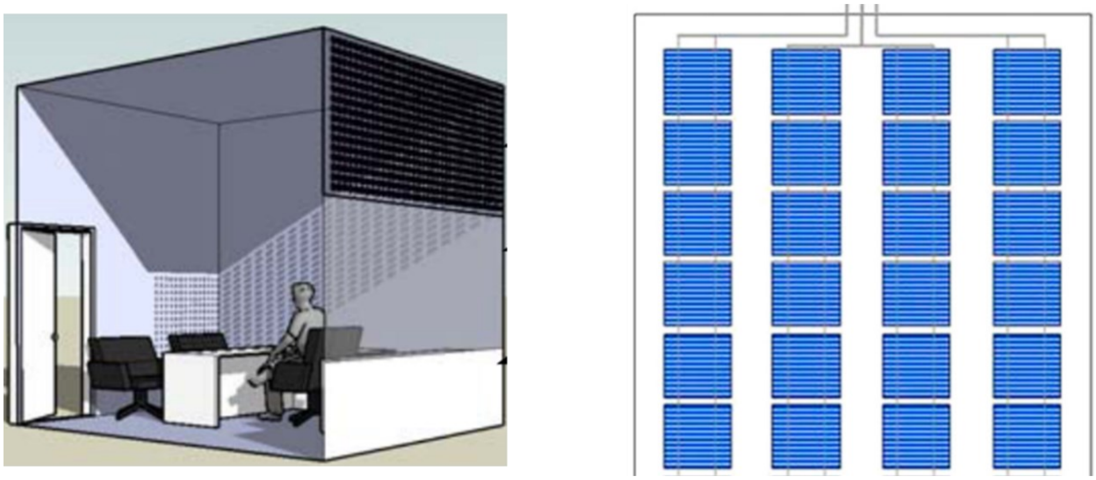

Figure 2.3: *Simulated single person office space with a three-section façade (Robinson & Athienitis, 2009) (left) Configuration of a BIPV window with c-Si spaced cells (Park et al., 2010) (right)*

At the same time, amorphous silicon solar cells are the most researched cell type for BIPV applications. Multiple studies have been conducted to assess the energy saving and visual comfort capabilities of a-Si BIPVs. A study conducted by Chae et al. (2014) assessed the energy performance of commercial office buildings incorporated with building integrated photovoltaics in six different climatic conditions in the United States. The results show that a-Si BIPV have the capacity to reduce energy consumption in all weathers compared to a regular double-glazed window, but the reduction is highest in low latitude sites (warmer temperature). Energy generation is also higher in these locations. Furthermore, a-Si BIPV reduce greenhouse gas emissions: In the Chicago location, there was a decrease of 68.14 tons of carbon equivalent annually.

Another type of building integrated PVs are bi-facial cells, which can be both silicon based, and non-silicon based. As opposed to mono-facial solar cells that only capture photons from the front side of the device, bi-facial cells collect light from the front face (direct light) and the back face, by absorbing diffuse and reflected light (Guerrero-Lemus et al., 2016). This renders the cells more effective in terms of power output. Valdivia et al. (2017) compared the energy generation of bifacial and mono-facial cells under the representative weather conditions of Ottawa, Canada. The obtained results show that the bifacial can increase annual energy yield by up to 18%, while the instantaneous power increases by 13 to 35% during sunny days and by 40 to 70% during cloudy days. The authors state that the ground clearance, which is the distance between the bottom of a solar cell and the ground level, plays an important role in determining the energy produced from a bifacial cell. Other aspects can affect the efficiency of a bifacial cell, such as the geometry in which the cells are mounted and the albedo (Russell et al., 2017). The albedo refers to how well a surface reflects light. The design aspects / considerations will be discussed in more detail in section 2.2.4.

With the different types of BIPV discussed, the next section will discuss the electrical and thermal properties of BIPV which impact the efficiency and the comfort levels they offer within the indoor environment.

2.2.2- Electrical and Thermal Implications of BIPV Windows

Ng et al. (2013) summarize the effect of semi-transparent BIPV application on buildings into three main categories: Optical, thermal, and electrical. Each category is quantified using certain indices (for example, the electrical impact can be quantified using the efficiency of the solar cells) and impacts the comfort and the performance of the indoor space. Figure 2.4 encapsulates the idea behind this categorization. The optical implications will be discussed in section 2.3. This part will focus mostly on the electrical and thermal implications of BIPV windows, and how the properties of the latter can ensure comfort while allowing for increased on-site energy generation.

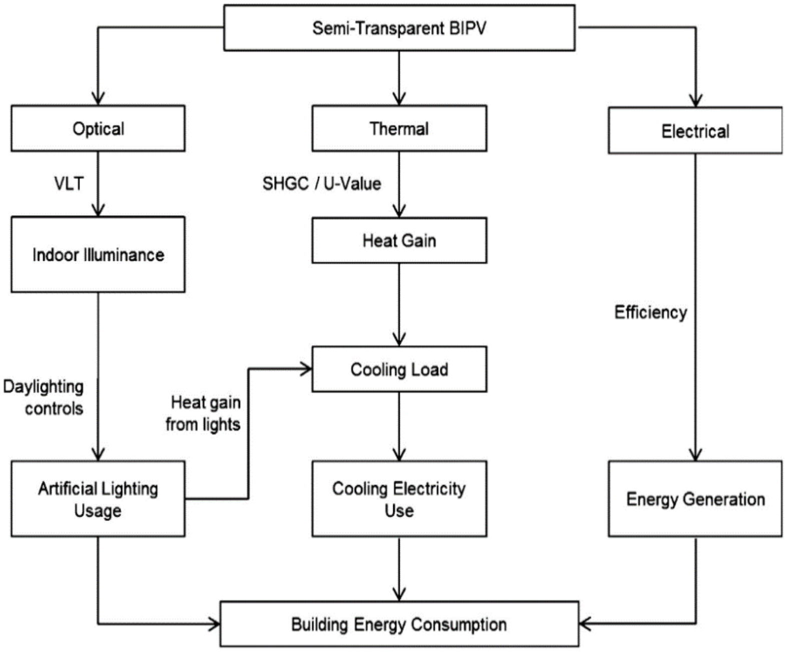

<u>Figure 2.4:</u> *Effects of semi-transparent BIPV windows application (Ng et al., 2013)*

The electrical output of a solar cell, and by extension a BIPV installation, is mainly impacted by climatic and geographic conditions (outdoor conditions, orientation, …) that have been discussed earlier and by their electrical properties. The electrical properties refer primarily to the efficiency η, the fill factor FF, the open circuit voltage V_{oc}, the short circuit current I_{sc}, and the maximum power P_{max}. The efficiency is calculated using Equation 2-4:

$$\eta_{STC} = \left(\frac{P_{max}}{A \cdot G}\right) \cdot 100 \qquad (2\text{-}4)$$

Where A is the area of the cell / array / installation in m^2, P_{max} is the maximum power of the cell / array / installation in $Watts$, and G is the incident solar radiation in $\frac{W}{m^2}$.

The incident solar radiation to calculate the efficiency is usually 1000 $\frac{W}{m^2}$, which represents the solar irradiance under standard test conditions STC. Therefore, Equation 2-4 refers to the STC efficiency.

However, the variations in cell temperature can vary η: Increased cell temperature decreases its efficiency (Hassan et al., 2016). At a PV temperature T_{PV}, the efficiency can be calculated using the Equation 2-5:

$$\eta_{PV} = \eta_{STC} \cdot [1 - \alpha_{PV}(T_{PV} - 25)] \quad (2\text{-}5)$$

With η_{PV} being the efficiency at the cell temperature T_{PV}, and α_{PV} being the temperature coefficient of power for a PV cell / module.

The choice of the cells to be used in a building integrated installation needs to be considered prior to construction based on the location. For example, if the BIPV system is planned to be installed in a hot climate, solar cells with a small α_{PV} need to be used so that the efficiency remains in a nominal range.

In terms of the thermal implications, BIPV have similar properties to AFS. These properties are mainly the thermal transmittance U-value and the solar heat gain coefficient SHGC, explained thoroughly in section 2.1.4. When installing BIPV as part of an advanced fenestration system, both their thermal implications must be considered to ensure that the indoor environment is thermally comfortable. The thermal properties also indirectly impact the amount of energy produced by the cell and the levels of visual comfort.

2.2.3- Building Integrated Photovoltaics with Thermal Recovery

Solar energy technologies are broadly divided into photovoltaic systems, which directly convert sunlight into electricity, and solar thermal systems, which convert solar energy into heat. In solar thermal setups, electrical energy is sometimes used to circulate working fluids. This need for external electricity can be eliminated by integrating photovoltaic and thermal systems into a combined photovoltaic/thermal system which, once incorporated into the building components, becomes a building integrated photovoltaic/thermal (BIPV/T) system (Maghrabie et al., 2021). There are two ways of integrating the air recovery for these systems, as illustrated in Figure 2.5. The fresh air that flows behind the PV cells is used to heat up the internal environment and cool down the solar cells to reduce the impact of the heating effect, increase the life span of the panels, and ensure high energy productions throughout the year (Biyik et al., 2017).

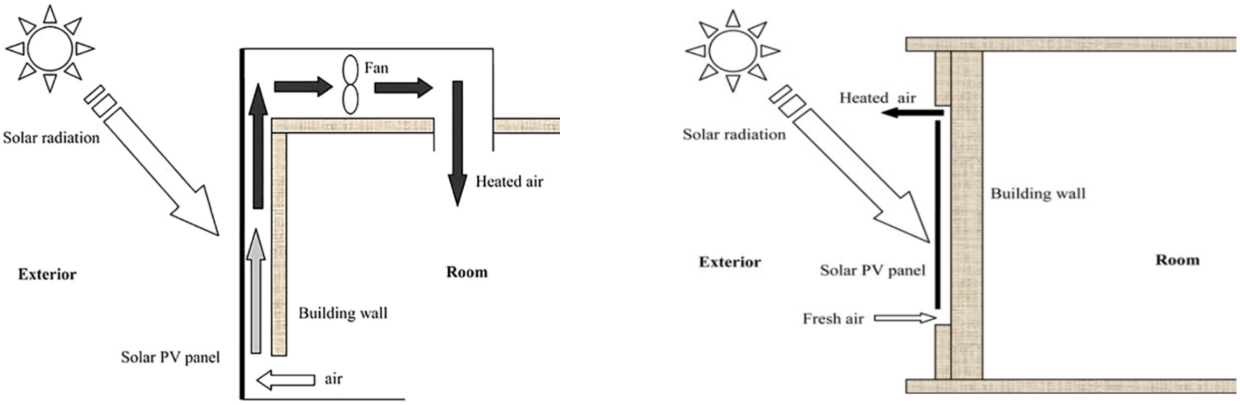

Figure 2.5: *Schematic Diagram of a building integrated PV with thermal recovery from the inside environment (left) and outside environment (right) (Quesada et al., 2012)*

There are three main applications of BIPV/T systems: combined solar cooling / heating power, solar ventilation, and architectural envelope (Maghrabie et al., 2021). The two last applications are less common. Solar ventilation BIPV/Ts cool the modules while pre-heating the ventilation air. In terms of architectural design, these systems are used as building envelope components to help optimize the daylighting and cooling requirements (Piccolo & Simone, 2015). Power production (electrical and thermal) is the most common and most studied application of BIPV/Ts. Chen et al. (2010) analyzed the thermal performance of a BIPV/T system installed in a near net-zero energy house located in a cold climate. The results show that the PV module's temperatures were significantly reduced (which allows the efficiency to remain at steady levels) and significant amount of solar thermal energy was collected: on a sunny day, and with a flow rate of 250 L/s, the exhaust air temperature was between 30℃ to 35℃. Furthermore, these systems' efficiency can be further improved with the implementation of model predictive control. A study by Sigounis et al. (2023) investigated how MPC can improve the performance of pre-installed BIPV/T system in a net-zero energy building in Quebec. The results show that the energy consumption was reduced by 40% compared to the business-as-usual operations of the system.

2.2.4- Design Considerations

Some design elements, like the type of PV cells used, have already been discussed in previous sections. This section will focus on implications regarding the construction and implementation, with an emphasis on bifacial solar cells. Albedo is one of these essential design considerations. It refers to the reflectivity of the surfaces around a solar panel, which reflects daylight back to the PVs, increasing their production. It is defined as the ratio between the power of the reflected light and the power of the incident light (Russell et al., 2017). Albedo depends on the material surrounding the PV cells (concrete, snow, dirt, sand, …) and increase energy generation, and more specifically the bifacial energy gain, with this gain being proportional to the albedo (Kreinin et al., 2016). The same study concluded that the electric gain and the equivalent cell efficiency also increase with albedo.

Furthermore, ground clearance is also a design implication that affects the energy production of bifacial PV cells. Ground clearance is defined as the elevation between the ground and the bottom of the solar cell / solar array. An increase in the ground clearance is translated into an increase in energy production (Kreinin et al., 2016; Yusufoglu et al., 2015). However, this proportional relationship reaches a peak at around 0.4 – 0.5 meters (Kreinin et al., 2016), with other studies reporting a decrease after reaching a certain altitude (Yusufoglu et al., 2015). Figure 2.6 shows the electric gain and efficiency based on albedo and ground clearance.

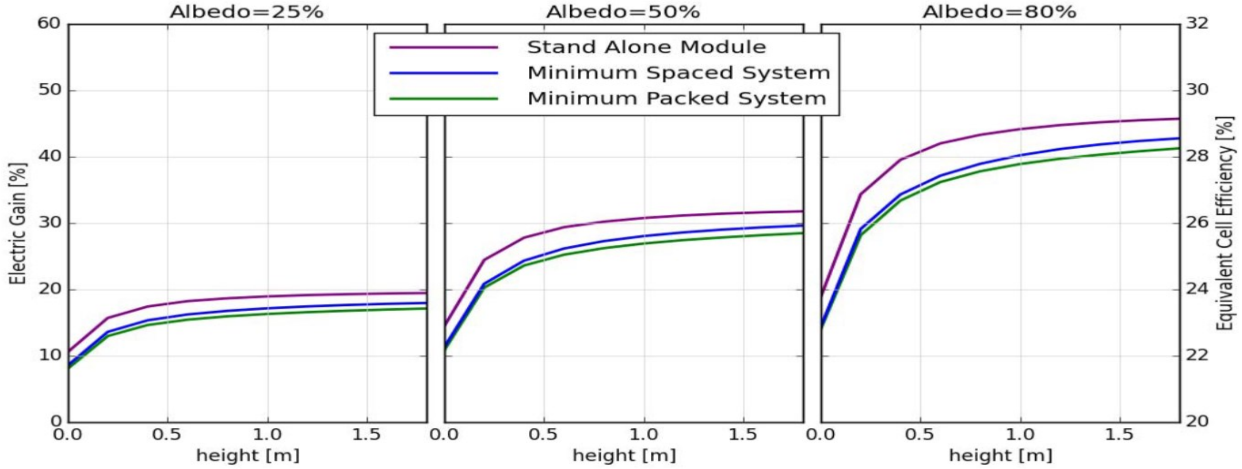

Figure 2.6: *Annual bifacial gain and equivalent cell efficiency as a function of ground clearance for various system designs (Kreinin et al., 2016)*

The packing factor PF can also have an impact on the production of building integrated PV system, both mono-facial and bifacial. It is defined as the ratio between of the area covered by solar cells and the total area of the glazing, and is calculated (in percentage) using Equation 2-6:

$$PF = \frac{A_{PV}}{A_{glazing}} \cdot 100 \tag{2-6}$$

The choice of the packing factor is a tradeoff between energy generation, thermal comfort, and visual comfort. Vats et al. (2012) conducted a study to analyze the effect of the packing factor of different types of semi-transparent BIPVs on energy performance and thermal comfort. Multiple conclusions were made, most notably: A decrease in the PF leads to a decrease in the overall temperature of the cells, which in turn increases their efficiency. There is also an increase in the room temperature of the inside when the PF is smaller (because of increased transmitted irradiance). The results show that an increase in the packing factor is not always optimal for electrical and thermal performance, since a PF of 0.62 performed better in both aspects compared to a PF of 0.83.

Design considerations for BIPVs are not limited to the ones discussed in this section, as there are multiple other factors that need to be accounted for such as orientation of the window, tilt angle, and climate in which the system is installed.

2.3- Quantifying Visual Comfort

This section will first discuss the different types of light impinging on a BIPV system, to later provide information regarding how visual comfort is assessed in academic research. The last two subsections provide information regarding metrics that are used to quantify daylight illuminance and the impact of glare in the indoor environment.

2.3.1- Types of Light

Spectral light from the sun originates from the continuous nuclear fusion reactions happening in its core. It covers an array of wavelengths, ranging from ultraviolet (UV), to visible, to mid-infrared (Stanley et al., 2016). Terrestrial solar radiation, impacted by atmospheric absorption and scattering, spans 280 to 4000 nm, with over half the energy exceeding 700 nm, concentrated mainly in the visible spectrum where peak intensity lies (Stanley et al., 2016). Figure 2.7 compares the terrestrial with the extra-terrestrial solar spectrum using the black body radiation spectrum as a reference. Details regarding absorption due to certain molecules in the atmosphere are also shown.

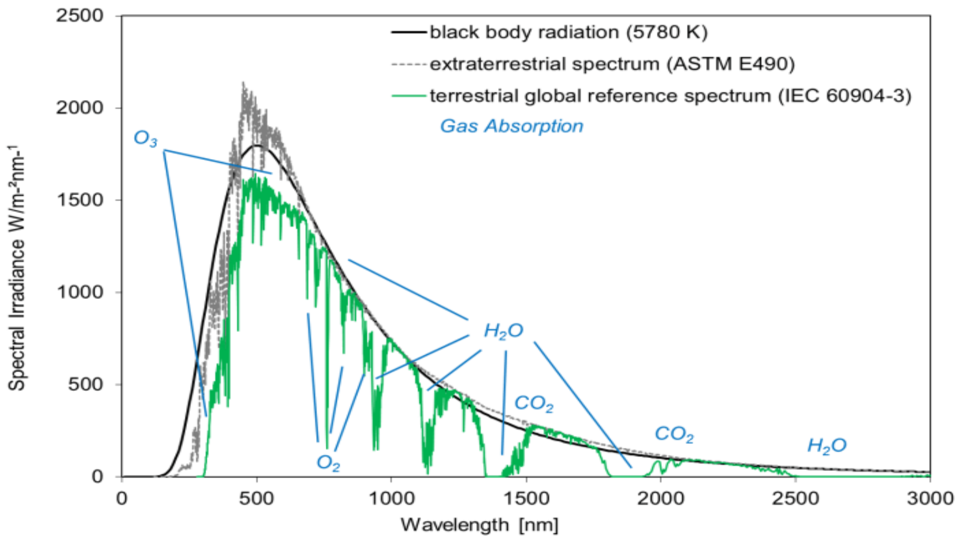

Figure 2.7: *The reference terrestrial solar spectrum in comparison with the extraterrestrial spectrum and the theoretical black body spectrum (Dirnberger, 2015).*

Once the radiation reaches the atmosphere, photovoltaic cells convert light to electricity efficiently within a narrow wavelength range. Photons outside these bands or lacking the energy for electron promotion cause heat generation, reducing the device's efficiency by increasing its temperature. Overall, the photons from solar radiation reaching a solar cell can either be transformed to electricity or thermal energy (Stanley et al., 2016).

According to the U.S department of energy, the solar energy that reaches the surface of the earth at any given moment depends on season, time of day, geographical location, landscape, and outdoor weather. Due to Earth's shape, sunlight reaches the surface at varying angles, varying between horizontal (incidence angle of 0 degrees) to vertical (incidence angle of 90 degrees). Sunlight that hits directly overhead delivers the maximum energy possible to the Earth's surface. However, as the angle becomes more oblique, sunlight travels a longer path through the atmosphere, scattering and diffusing in the process. That is why two types of light can reach a device on the Earth’s surface: Direct (beam) light, or diffuse light.

The same source defines diffuse sunlight as any light that is scattered or reflected as it travels through the atmosphere because of air molecules, water vapor, clouds, dust, and pollutants. Direct light refers to the sunlight that has not been diffused. Direct light is more common during clear days, as only 10% of the light reaching the surface is diffused. However, diffuse light is more common on cloudy days as 100% of the daylight is expected to be scattered as it travels through the atmosphere. Both types of light affect visual comfort in the inside environment differently: Direct light leads to increased indoor illuminance but can cause glare, while diffuse daylight is generally dimmer, but does not cause disturbing levels of glare.

2.3.2- Light Assessment

According to Shafavi et al. (2020), there are three methods to assess visual comfort within an indoor environment: Questionnaire, simulation, and measurements.

Questionnaires provide a subjective evaluation of comfort levels. Surveys used mainly focus on the occupant's perception of glare, daylight level, and overall satisfaction which includes the ability of view to the outside (Shafavi et al., 2020). An essential part of surveying is to collect personal information from the sample, which include age, gender, visual capabilities, … For example, a study conducted by Mangkuto et al. (2017) to determine the appropriate criteria for discomfort glare involved a survey where only individuals native to the country (Indonesia in this case) where eligible to participate. There are also two types of survey design: cross-sectional and longitudinal. A cross-sectional study collects data across various subjects (like occupants or buildings) at each occurrence, whereas a longitudinal study involves gathering data from the same group of subjects over a time period, tracking changes or developments (Wagner and Brien, 2018).

Other information related to the environment needs to be collected simultaneously, like the sky condition. Some questionnaires are completed under a specific sky condition (Mangkuto et al., 2017), while others involve different cloud covers to highlight their impact on the indoor environment. Other factors that can be recorded are the activity level of the occupants, the blinds position, the intensity of the electrical lighting if any, and the illuminance adjustments that the occupants make manually or that surveyor decides automatically (Shafavi et al., 2020). Once the data is collected, statistical methods are used to analyze the relation between the different variables and to generalize the information for a larger population. A study conducted by Bellia et al. (2017) used both Spearman and Pearson correlation to develop a relationship between the measured data and the occupant's opinion regarding visual comfort in three daylit office spaces in Naples.

Simulation is also a very common and cost-effective tool to assess visual comfort. Current tools can provide results using multiple metrics for glare and illumination. The most common software used are Daysim and Radiance, with the DIVA and Everglare interfaces (Shafavi et al., 2020). To run an accurate simulation, different models for different elements need to be setup. The sky is most commonly modeled using the Perez all sky approach and a typical meteorological year (TMY) from the nearest weather station. The studied space, shading, window design, and luminaires (artificial lighting) need to also be simulated accurately. Validation of the results is then done using experimental data from a test cell or confirmation from previous studies ensuring the validity of the software and models.

Measurements are the final method used to collect data regarding visual comfort. Photometers, solar pyranometers, spectroradiometers, spectro-photometers, and HDR photography are some of the most common tools used to measure indices that quantify lighting and glare (Shafavi et al., 2020). Other studies report on measurements regarding air velocity, CO_2 levels, or air humidity. In terms of reported data, there are three main categories: Illuminance data, which represent the indoor lighting quality (Kong et al., 2018), luminance data as a visual perception indicator, and solar irradiance to corelate outdoor climate with indoor conditions. Other reported data involved indirect measurements of the window transmittance and the surface reflectance.

2.3.3- Daylighting Metrics

Daylighting metrics are used to assess the daylighting performance of advanced fenestration systems realistically (Kuhn, 2017). The same source states that the daylight that is transmitted through a building envelope, and more specifically windows, is determined by the properties of the fenestration (orientation, size, position, transmittance, and operation / control) and by the outdoor conditions (location, cloudiness level). This section will focus on metrics that are generally used to assess the lighting and daylighting requirements of a space.

- Horizontal and Vertical illuminance:

Horizontal illuminance E_h and vertical illuminance E_v define the level of brightness or the level of darkness that an individual feels (Iwata et al., 1994). E_h refers to the amount of light received on a horizontal surface, like a desk for example, while E_v refers to the amount of light received on a vertical surface, like a wall. Their unit is lux. Studies have shown that horizontal illuminance correlates with occupant satisfaction with regards to the level of daylighting within a space (Jakubiec et al., 2019). However, the same study also concludes that this level of satisfaction is space / and activity dependant: An occupant does not require the same amount of daylight in an office space as he does in a residential space. At the same time, the requirements are different if the person is cooking or sleeping within that residential space. E_h and E_v are essential to quantify light within an indoor space, but they are not good glare indicators, as sources differ on how accurate they are to quantify glare levels (Shafavi et al., 2020). However, comparing these two metrics, vertical illuminance is more accurate compared to horizontal illuminance.

- Daylight Factor:

The daylight factor D is used as a minimum requirement for building design (Kuhn, 2017). It is the ratio of daylight inside the building and daylight available outside, and is calculated using Equation 2-7:

$$D = \frac{E_{h,\ global\,indoor}}{E_{h,\ global\,outdoor}} \cdot 100 \qquad (2\text{-}7)$$

Where $E_{h,\ global\,indoor}$ is the global indoor horizontal illuminance in lux and $E_{h,\ global\,outdoor}$ is the global outdoor horizontal illuminance in lux.

However, this metric assumes a perfectly diffuse sky at all times throughout the day. Furthermore, the daylight factor cannot directly be used to predict indoor illumination levels under actual weather conditions for any specific location and facade orientation. Because of these reasons, D is rarely used in research (Shafavi et al., 2020).

- Daylight Autonomy:

The daylight autonomy DA compares the working hours where the occupants can completely function on daylight alone and the total working hours within a delimited time period (Reinhart et al., 2006). It is calculated using Equation 2-8:

$$DA = \frac{working\ hours\ with\ illuminance\ over\ the\ threshold}{total\ working\ hours} \cdot 100 \tag{2-8}$$

The threshold is determined based on the studied space and the type of activity being done by the occupants. Different standards have different thresholds. This metric has been commonly used in research with other variants being developed over time. cDA is the continuous daylight autonomy. This metric softens the transition between compliance and noncompliance by providing partial credit to timesteps where the illuminance is close to the threshold (Reinhart et al., 2006). This metric is used when dimming light control strategies are implemented within the space. Another less common variant is the spatial daylight autonomy sDA which evaluates the daylight autonomy based on the percentage of the floor area in the studied environment.

- <u>Useful Daylight Illuminance:</u>

Introduced by Nabil and Mardaljevic (2005), the useful daylight illuminance UDI abandons the idea of target illuminance and focuses on work plane illuminance being in a certain range. The logic that if illuminance falls below a certain range, occupants will not be able to carry out the necessary tasks. However, it adds the idea that an illuminance greater than the threshold can also be a source of visual discomfort. That is why the authors defined a range of useful daylight illuminance that can be obtained for a pre-determined time period. A range between 100 to 2000 lux was suggested based on the subjective input of occupants in a well-lit office space (Nabil & Mardaljevic, 2005).

- <u>Annual Sunlight Exposure:</u>

Annual sunlight exposure ASE is defined as the total amount of direct light that reaches a certain point in the indoor space over the course of a year (Reinhart et al., 2006). The units are in lux hours per year. This metric is most often used for spaces that include light sensitive artwork and has to be accompanied by other metrics if used for a residential / commercial building study. Korsavi et al. (2016) conducted a study to assess the visual comfort of daylit and sunlit classrooms in Iran using dynamic metrics and surveys. The threshold for ASE used was based on the LEED Simulation-based Daylight Credit Compliance and was equal to 1000 lux · 250 hours per year. The study concluded that there is no correlation between this dynamic metric and related user feedback that could reflect on visual comfort.

For all these metrics, the work plane illuminance E_p is an integral part of the calculations, especially for office spaces, as it represents the horizontal illuminance on a specific point in the environment.

2.3.4- Glare Metrics

Kuhn et al. (2017) categorizes glare within five categories, three of which do not affect indoor spaces and therefore are not considered for visual comfort studies. These are vision impairing glare and outdoor glare. Vision impairing glare can lead to permanent damage to the eye and is caused by focusing vision on a concentrated source of light (like curved mirrors for example). Outdoor glare occurs outside and is usually caused by light reflecting out of surfaces like snow or bodies of water. In terms of glare affecting indoor spaces, the same source (Kuhn et al., 2017) refers to three types: disability glare, discomfort glare, and reflex glare. The first impairs the ability to see details and contrasts, making it difficult to perform tasks. It can also reduce the size of the pupil which reduces the brightness of our vision. Disability glare's impact becomes more intense with age. Discomfort glare is less problematic than disability glare and depends on the feedback of the occupants. It can be classified as imperceptible, perceptible, but not disturbing, disturbing, but tolerable, and intolerable. Finally, reflex glare occurs when light reflecting off surfaces, such as a computer screen, reduces the contrast of displayed objects, making them harder to see. The rest of the section will provide metrics that are commonly used in studies to quantify glare levels.

- <u>Daylight Glare Probability:</u>

The daylight glare probability DGP was developed by Wienold & Christoffersen (2006) and uses the probability that person is disturbed by glare instead of the glare magnitude. It is calculated using Equation 2-9:

$$DGP = 5.87 \cdot 10^{-5} \cdot E_v + 9.18 \cdot 10^{-2} \cdot \log\left(1 + \sum_i \frac{L_{s,i}^2 \cdot \omega_{s,i}}{E_v^{1.87} \cdot P_i^2}\right) + 0.16 \qquad (2\text{-}9)$$

Where E_v is the vertical illuminance in lux, L_s is the luminance of source in $\frac{cd}{m^2}$, ω_s is the solid angle of the source, and P is the position index.

The coefficients were obtained through random optimization to obtain the highest correlation with subjective glare rating. The DGP is expected to be between the values of 0.2 and 0.8. Even though this metric is widely accepted, Shafavi et al. (2020) found some deficiencies such as overestimation in cases of high source luminance and lack of consideration of temporal effects. Other simpler alternatives to daylight glare probability have been developed and validated such as the simplified daylight glare probability $DGPs$.

- <u>CIE Glare Index:</u>

CIE glare index CGI was developed by Einhorn (1969) and later adopted by the international commission on illumination. It is used in spaces where high contrasts are expected. However, recent studies concluded that it tends to overestimate or underestimate glare under certain conditions (Hirning et al., 2014). It is calculated using Equation 2-10:

$$CGI = 8 \cdot log_{10}(2 \cdot \frac{1 + E_d \cdot 500}{E_d + E_i} \cdot \sum_{i=1}^{n} \frac{L_s^2 \cdot \omega_s}{P^2}) \qquad (2\text{-}10)$$

Where E_d is the direct vertical illuminance at the eye in lux, and E_i is the indirect vertical illuminance at the eye, also in lux. L_s is the luminance of source in $\frac{cd}{m^2}$, ω_s is the solid angle of the source, and P is the position index.

- <u>Daylight Glare Index:</u>

The daylight glare index DGI is also commonly used. It is a function of the position of the source, its size, and background luminance. It also takes into account the direction of view and is calculated using Equation 2-11:

$$DGI = 10 \cdot log_{10}(0.48 \cdot \sum_{i=1}^{n} \frac{L_s^{1.6} . \Omega_s^{0.8}}{L_b + 0.07 \cdot \omega_s^{0.5} \cdot L_s}) \qquad (2\text{-}11)$$

With L_b the background luminance in $\frac{cd}{m^2}$, and $\Omega_s$is the solid angle subtended by the glare source modified by Guth's position index equal to $\frac{\omega_s}{P}$ in steradian, and ω_s is the solid angle of the source.

DGI translates numerical values into categorical descriptions of glare, ranging from 16 (barely noticeable) to 28 (extremely uncomfortable). However, studies validating this equation indicate that its ability to predict glare from natural light through windows is weaker compared to its predictions for glare caused by artificial lighting (Hirning et al., 2014). With its inconsistencies, it is still a widely used estimator of glare levels.

- Unified Glare Rating:

The unified glare rating UGR combines elements from the daylight glare index and the CIE glare index. It is mostly used to evaluate glare from artificial lighting source like luminaires and is calculated using Equation 2-12:

$$UGR = 8 \cdot log_{10}(\frac{0.25}{L_b} \cdot \sum_{i=1}^{n} \frac{(L_s^2 \cdot \omega_s)}{P^2}) \qquad (2\text{-}12)$$

With L_b the background luminance in $\frac{cd}{m^2}$, L_s is the luminance of source in $\frac{cd}{m^2}$, ω_s is the solid angle of the source, and P is the position index.

The UGR method demonstrated significant precision in identifying both perceptible and disturbing glare, but its effectiveness substantially decreased when assessing intolerable glare levels.

Another aspect of visual comfort that can't be quantified but needs to be considered is the view to the outside (Kuhn, 2017). A study by Wienold & Christoffersen (2006) concluded that occupants accept a certain level of visual discomfort if they have a view to the outside. It also has a positive impact on the productivity and the psychology of the individuals.

2.4- Shades Control Strategy

Sections 2.1.2 and 2.1.3 discussed advanced fenestration systems as building envelope components. This section will focus on the different control approaches that can be applied to these AFS to help enhance their performance and optimize the comfort that they offer.

2.4.1- Classical and Advanced Control

Manual blinds are often left fully open or closed because occupants rarely adjust them, mainly doing so to block out glare and prevent visual discomfort (Kim et al., 2009). Yet, even in the absence of discomfort, the shades and lighting typically don't change, leading to higher energy consumption and lost opportunities for outdoor views. Adopting automated blinds integrated with lighting controls can efficiently manage daylight, address issues with glare and heat, enhancing both comfort and energy efficiency (Galasiu et al., 2004). That is why active façade control has become an essential tool in controlling comfort and reducing energy consumption because most adaptive facade systems offer a mix of active and selective control over energy and mass flow between a building and its surroundings, as well as managing thermal insulation, natural ventilation, shading, and daylighting. Additionally, they can locally generate electricity and heat for air and water using solar energy (Alkhatib et al., 2021).

Alkhatib et al. (2021) also make the distinction between classical control and advanced control. In classical control, two techniques are commonly used: rule-based and proportional integral derivative (PID). Rule-based approaches regulate processes within specified limits using upper and lower set points. These methods are primarily employed for managing temperature control. However, some rule-based strategies can lead to energy efficiency because of their lack of flexibility in dealing with variables not accounted for or incomplete data.

Meanwhile, advanced control systems for shades predict the behavior of an adaptive facade using a building model, encompassing five main types: Adaptive control, Optimal control, Model Predictive Control (MPC), Feedforward/feedback mechanisms, and Robust controls (Alkhatib et al., 2021). Dounis & Caraiscos (2009) define adaptive control as a control system that adjusts its parameters and control strategy dynamically in response to changes in the external environment or the system itself by learning the system's behavior over time and adapting to ensure optimal performance. Optimal control determines a control strategy that minimizes or maximizes a specific performance criterion, such as cost, energy, or time, subject to given constraints (Dounis & Caraiscos, 2009). MPC models the future behavior of the blind position over a limited time period and chooses the optimal control approaches to reach the control strategy's objective. It is a dynamic approach where the prediction of the optimal tilt angle and the optimization are done at each time step (Huchuk et al., 2016). Robust control aims to keep system performance and stability despite uncertainties and parameter changes. The objective is robust operation even when the model does not match the real-world conditions of the considered system (Alkhatib et al., 2021). Finally, Feedback / Feedforward control uses both as input to impact the behavior of the system. Feedforward comes from outside disturbance and feedback comes from the initial output of the system. Other control approaches that are less common involve model free control, intelligent, and hybrid control (Alkhatib et al., 2021).

2.4.2- Open Loop Control Strategies

All the control approaches discussed in the previous section fall into one of two control techniques: closed-loop control (also called extrinsic control) or open-loop control (also called intrinsic control). These categories broadly cover control strategies used in various systems, like HVAC systems for instance. However, this section will specifically focus on open and closed loop strategies for shading control.

Closed loop uses feedback from the system as an input to update the input continuously and actively. This means that the outcomes of the present action or setup can be evaluated against the targeted state or set point, allowing for active adjustments to the system's behavior if required (Loonen et al., 2013). Open loop, on the other hand, does not use feedback and directly makes decisions based on the environmental conditions (captured using sensors), which requires less energy and less hardware while also allowing for more flexibility (Alkhatib et al., 2021). Figure 2.8 summarizes the difference between the two approaches.

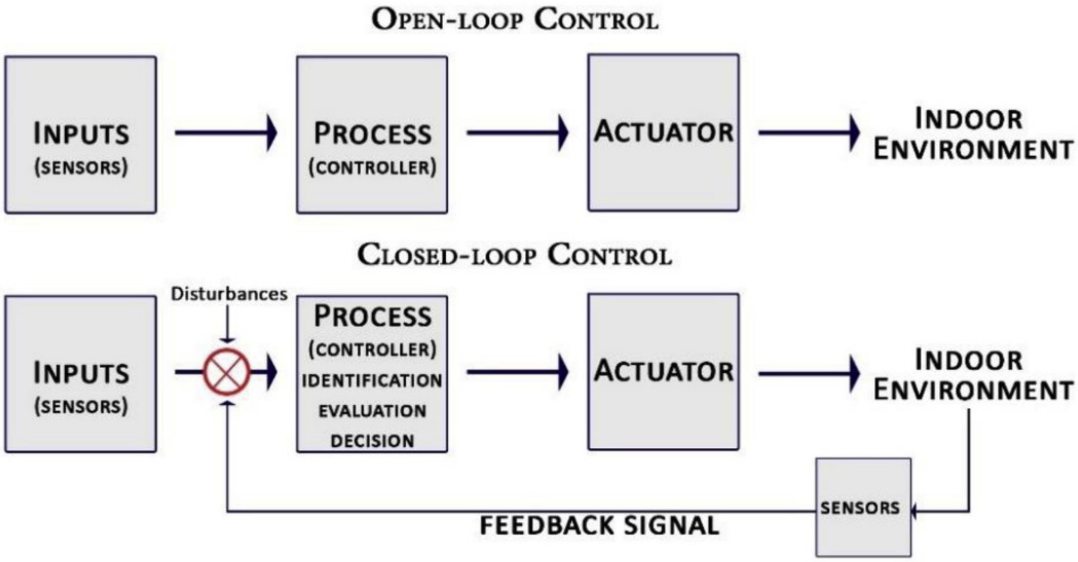

<u>Figure 2.8:</u> *Diagram of Open-loop and Closed-loop control algorithms (Tabadkani et al., 2020).*

Jain & Garg (2018) argue that open loop controls for shading systems are more efficient and optimized compared to closed loop systems for multiple reasons. Open-loop systems provide more calibration flexibility compared to closed-loop systems: Doulos et al. (2005) argue that open loop control is less prone to errors in sensor placement or field of view, unlike closed loop systems, where sensor placement has to be done carefully and the sensors need to be calibrated. The calibration process for these sensors is an expensive and complicated process that makes closed loop control a challenge to implement (Jain & Garg, 2018). The same source states that the implementation of virtual sensors within simulation models, rather than using actual sensors, has been assessed and found to be more efficient for open loop control, which reduces the overall cost of implementation. Overall, open loop control has been favored lately compared to closed loop control because it is cheaper, easier to implement, and it does not require calibration of the sensors since there is usually only one sensor mounted in the exterior to measure outdoor conditions like temperature or daylight which provides the necessary information so that the optimal shading position can be deduced at each time step.

Numerous techniques employ traditional open-loop system-based control for managing blinds and lighting (Jain & Garg, 2018). They mostly follow the same structure: first, they start by estimating the outdoor daylight conditions. Based on this information, the next step is to calculate the indoor daylight metrics. Finally, the light levels or the dimming levels are determined based on the objective of the control strategy. For sky conditions, the most commonly used sensors are outdoor photometers on window facades and pyranometers for measuring global horizontal or vertical illuminance and irradiance. While these devices accurately capture daylight data, they fail to offer real-time sky luminance distribution. For this information, precise sky models are needed. Sky scanners and digital cameras are tools that were used in previous research to achieve this. However, calibrating sensors in open-loop controls is often laborious and susceptible to errors (Jain & Garg, 2018).

For determining indoor daylight metrics like illuminance or glare levels, numerical and simulation methods can be used. The input of these models are usually the outdoor environment information (temperature, cloudiness level, global irradiance, and global illuminance) and the properties of the studied space (orientation, dimensions, surface reflectance). The results from previous studies show that this approach accurately simulates the real-life results of indoor illuminances (Jain & Garg, 2018). The final step, which is determining the tilt angle and the light levels, will be discussed in section 2.4.3 as there is multiple approaches to making the decision.

2.4.3- Visual Comfort Centric Control Strategies

Window blinds can be controlled for multiple reasons such as reducing daylight glare, conserving energy on lighting, enhancing thermal comfort, preserving outdoor views, and maintaining privacy. In numerous studies, the primary goals for controlling window blinds focus on minimizing glare, preventing overheating, and managing illuminance levels (Jain & Garg, 2018). These studies usually integrate both blind and artificial control.

A common strategy is the cut-off control approach. The algorithm adjusts the blind slats to consistently block direct sunlight. It uses the solar profile angle as an input to determine the optimal tilt angle of the blinds as its output. This approach can also be used to limit the levels of glare within the indoor space. Chaiwiwatworakul et al. (2009) conducted an experimental and simulation study on the application of venetian blinds for daylighting in tropical climate. One of the control strategies analyzed was a cut-off approach where the blinds remained fully open when the solar profile angle was greater than 40.3 degrees, and adjusted to an angle at which direct sunlight was fully shaded when the profile angle was below the threshold value. The results show that artificial lighting was only needed during the early hours of the morning and late hours of the afternoon. The authors also conclude that automated blind systems provide visual comfort in indoor environments with good levels of illuminance and low glare.

Another type of control strategy for visual comfort is based on glare and illuminance metrics. They are optimized to prevent glare while increasing energy savings (by taking advantage of sunlight instead of artificial lights). One simple example to illustrate such a control strategy was developed by Chan & Tzempelikos (2013) with the objective to avoid glare and maximize daylight. Initially, the tilt angle is set to a horizontal position (0°). Depending on the outcomes of DGP simulations or measurements, the system determines whether the slats require further rotation, adjusting in small steps. Figure 2.9 is the flowchart explaining the logic behind this control strategy. Even though this is a simple strategy that clearly illustrates this type of control, it has multiple flaws. First, it uses a closed system, meaning that additional hardware like HDR cameras need to be used. Second, this type of control strategy does not account for some important factors like the occupancy schedule of the individuals using the space or the view to the outside. The authors state that the frequent movement of the venetian blinds can be distracting to the occupants.

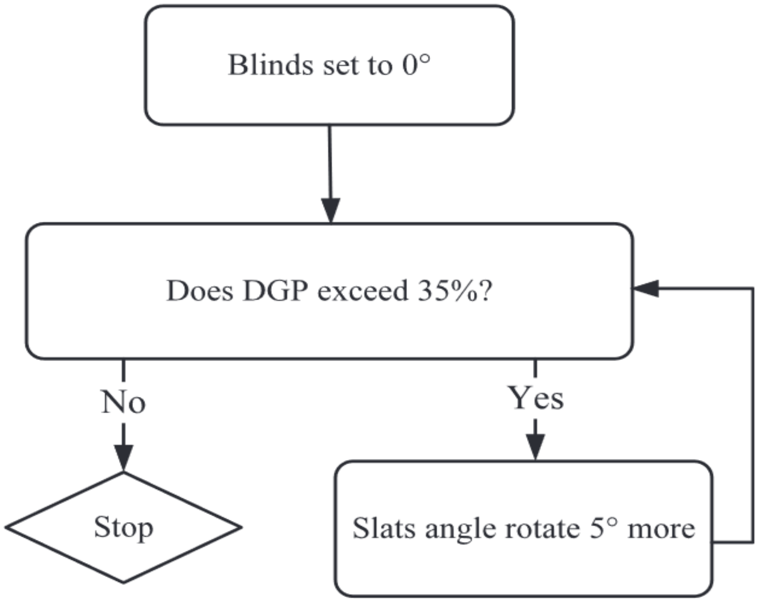

Figure 2.9: *Flowchart of a simple venetian blinds control strategy based on glare metrics (Chan & Tzempelikos, 2013).*

Finally, control strategies for visual comfort can also be based on the occupancy pattern of the space. This approach considers the occupancy level of the space as well as the usual behavior of these occupants (number of interactions with the thermostat or number of times the blind tilt angle of the venetian blinds was changed) as input for the control strategy. Data can be collected through surveys or using movements sensors. Mahdavi & Spasojevic (2006) developed an energy-efficient daylight-responsive control strategy that uses data collected in real time. The inputs of the strategy are the properties of the room, the sky conditions, and the occupancy while the output is the position of the window blinds and the status of the artificial lighting. For occupancy behavior, the authors collected data for the presence of people through occupancy sensors. Their preferences in terms of visual comfort were communicated using questionnaires / surveys available on computers within the test space. The results show that such a control strategy has positive results on the illuminance levels of the space as well as a reduction in energy consumption over the 15-day test period.

2.5- Research Gaps

Firstly, the current body of literature focuses on the most common types of advanced fenestration systems that are, for the most part, commercially available. This usually involves double glazed windows that either have an integrated shading device or an energy generating technology. However, due to the broad definition of AFS, some have not been studied in depth yet due to a lack of accessibility of these devices or the high cost of manufacturing on a small scale (since they will be used for a study and not for commercial purposes). Advanced fenestration systems like a triple glazed window with inner pane venetian blinds and integrated photovoltaics have not appeared in any publications that have been reviewed for this thesis. The complexity of these systems translates into a set of unique thermal and visual properties that must be considered separately when trying to develop models that mimic their real-life behavior. The impact of this AFS on different indoor environments has not appeared in literature either, or its behavior under a control strategy has yet to be analyzed.

Furthermore, previous literature that has been reviewed for this thesis mainly concentrate on the thermal properties of advanced fenestration systems and their impact on the thermal comfort of the occupants. There seems to be a lack of recent publications that focus on developing models to analyze the visual and optical properties of AFS. Some publications that contributed transmittance models for AFS focused on simpler types of glazing. These equations do not apply for more complex windows with different interconnected components. In addition, these developed models are provided as a stand-alone contribution rather than an application. There seems to be a lack of publications that focus on using the visual properties of AFS as part of a control strategy for advanced fenestration systems that can be scalable and applicable to different indoor environments.

Finally, the publications discussed in this thesis provide limited options for visual comfort centric control strategies. As stated in section 2.4.3, there are three strategies for control strategies focused on visual comfort: the cut-off strategy, the glare / illuminance levels strategy, and the occupancy-based approach. A small percentage of the reviewed strategies for active shading devices use one of these strategies as the main technique to optimize visual comfort. A more common approach is to use a hybrid approach where two of these techniques are coupled together to obtain a control strategy to optimize the position of the shading device at each time step. However, there appears to be a lack of control strategies which are a hybrid of all three techniques simultaneously. Such a hybrid approach can use the advantages of each while downsizing the impact of their inconveniences. In addition, with visual comfort centric control, there seems to be a lack of energy optimization considerations: A potential visual centric control can use the passive solar heating to reduce energy consumption.

3. Chapter 3: Methodology

The methodology will discuss the methods and equations used to achieve the objectives in section 1.3. The first part presents the case study used to develop and validate the contributions of this thesis, as well as giving more details regarding the experimental setup used. The following section presents the data driven models developed for the transmittance of the advanced fenestration system under clear and cloudy sky conditions. A benchmark model using equations from previous literature is also presented for comparison. The following two subsections will discuss the daylighting equations and the flow of the control strategy. The last subsection will analyze the different physical parameters considered for the sensitivity analysis.

3.1- Case Study

This section presents the single person office space that was used to develop the transmittance models and to simulate the control strategy. The experimental setup is also presented as part of the case study.

3.1.1- Office Space

The studied space is located in the Future Buildings Lab (FBL) on Concordia University's Loyola campus. It has a latitude of 45.45°N and a longitude of 73.63°W. The FBL is made out of five separate testing cells that represent single person office spaces. They have similar dimensions but have different fenestration systems. The structure is south facing and has no obstructions in front of it, meaning it receives direct sun throughout the day. The test cell that was used in this study is test cell number 4, highlighted in Figure 3.1. This cell was picked because of the type of fenestration that was installed and its window to wall ratio of 56%, representative of the WWR used in large office spaces.

Figure 3.1: *Concordia University's Future Buildings Lab (Baril, 2023)*

Test cell 4 has a length of 3.402 meters, a width of 3.050 meters, and a height of 3.048 meters. There are three windows that are south facing. The two side windows are triple glazed with bi-facial silicon photovoltaic cells on the outer glazing and inner pane venetian blinds. The middle window is double glazed with an interior low transmittance roller shade. The three windows have a length of 1.954 meters and a width of 0.986 meters. The venetian blinds used on the side windows have a width of 34.9 millimeters and a thickness at the center of 6.4 millimeters. Heating is done using a hydronic radiant floor heating system (turned off completely during experimentation in the space). The cell has a luminaire in the center of the space that was also not used in this study. Figure 3.2 is a 3D schematic of the space with information about the dimensions. In addition, the space is used to represent a single person's office space. The occupant is assumed to be sitting facing the west wall in the center of the room, which is approximately 1.5 meters away from the window. The work plane height is 0.8 meters, which represents the standard height used for work plane illuminance studies. In order to reduce the impact of multiple incident light reflections on surfaces, the only piece of furniture used in the space is a desk. The reflectance of the surfaces is assumed to be 60% for the walls, 80% for the ceiling, and 30% for the floor based on

Reinhart et al. (2006).

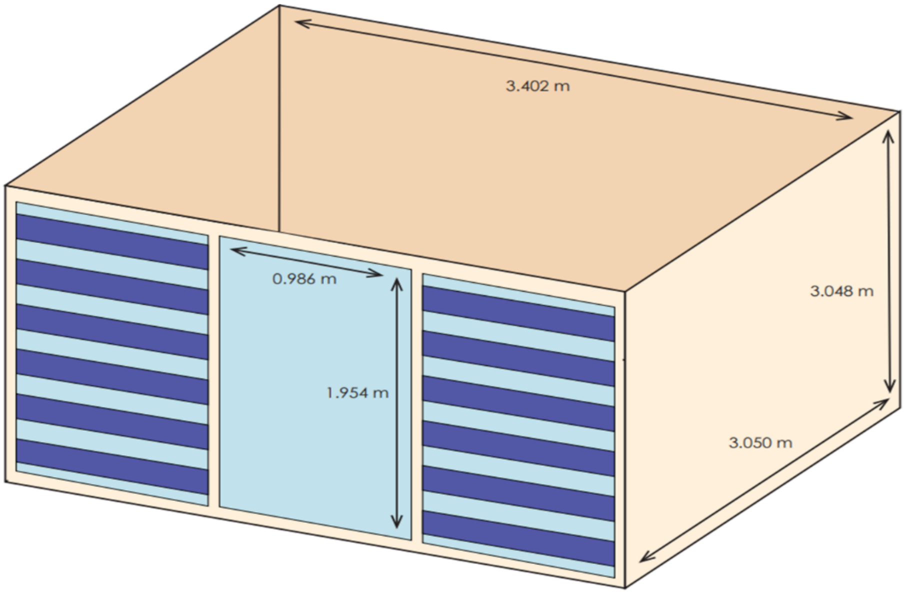

Figure 3.2: *Three-dimensional schematic of Test cell 4 at the FBL building.*

3.1.2- Fenestration

The fenestration system studied is a triple glazed window with semi-transparent bi-facial silicon PV cells on the outer glazing and inner pane aluminium venetian blinds. The glazing thickness is 6 millimeters, with argon gas filling the cavity between the outer and middle glazing. In terms of the outer glazing, the packing factor PF is 45.9%, meaning that solar cells cover almost half of the total glazing area. The PV cells are divided into six equidistant rows, with each row having a total of six cells. The 36 cells are then connected in series to a soon to be installed storage system. The cells visual transmittance is 54.09% under standard test conditions, obtained from the manufacturer’s data sheet. The cells efficiency for the mono-facial model is between 6 and 7%.

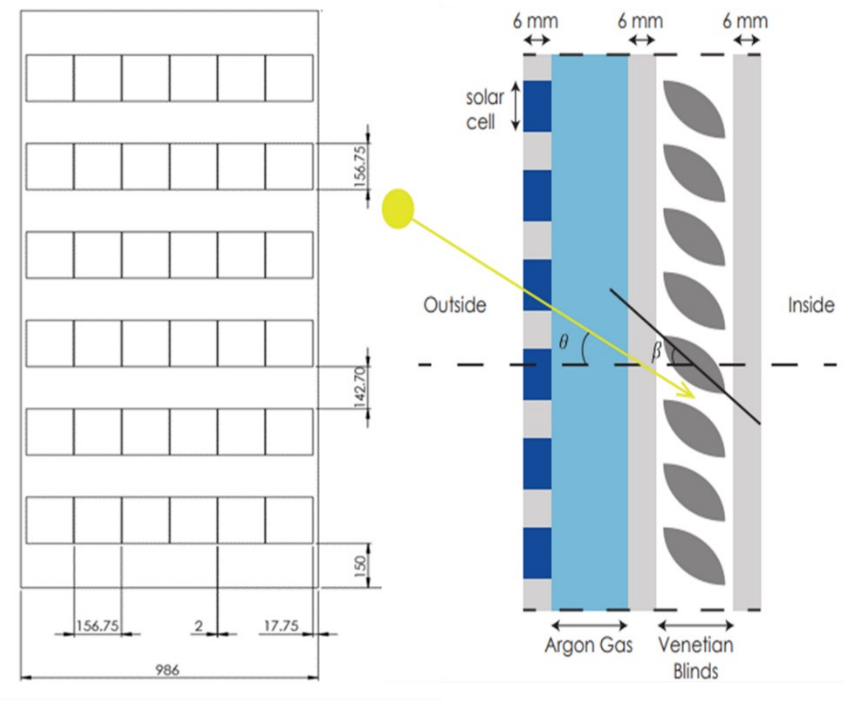

Figure 3.3: *Frontal view of the outer glazing with measurements in millimeters (Source: Canadian Solar) (left) and Transversal view of the advanced fenestration system (right)*

In terms of the venetian blinds, they are made from highly reflective aluminum shutter blinds (oval shaped) and are motorized. The motorized venetian blinds MVB can rotate between 0 degrees and 90 degrees. 0 degrees represent the completely horizontal position, while the 90 degrees represent the completely vertical position. In this angle, it is assumed that the MVB act like a highly reflective opaque surface, so no light is transmitted. It is assumed for this study that the venetian blinds can only rotate with increments of 5 degrees to simplify the procedure of the control strategy and reduce the computational needs of the latter.

In addition, constant movements of the blinds can be disturbing to the occupant, and no change in illuminance can be perceived in an interval of 5 degrees of tilt angle. The layer of argon gas between the outer and middle glazing has many advantages, mainly increased thermal insulation: the thermal conductivity of argon is lower than that of air, which improves the thermal properties of the fenestration. Other advantages of argon gas are the longevity and the noise reduction it provides. However, it is more costly than air filled windows and can suffer from leakage: under extreme weather conditions, the seals can deteriorate, and the gas leaks, reducing the thermal.

insulation of the overall fenestration. Figure 3.3 shows a frontal and a transversal view of the advanced fenestration system. The tilt angle of the blinds β and the incidence angle of the sun θ are shown on the transversal view.

3.1.3- Experimental Setup

The experiments were done with the objective of collecting data to develop visual transmittance models for the AFS and to use that data to validate the results. The data was collected for 10 days between the 20th of September 2023 and the 10th of October 2023 for sunny / clear days, and between the 27th of April 2024 and the 30th of April 2024 for cloudy / overcast days. The test cell where the experiment was conducted is located in Montreal, Canada, which represents a cold climate. Thus, these periods represent the beginning and the end of the heating season. For clear conditions, each day where the experiments were run represents a specific tilt angle, starting at 0 degrees until reaching 90 degrees, with increments of 10 degrees. For cloudy conditions, the data was collected for 0 degrees, 45 degrees, and 80 degrees. The data was collected between 7:00 AM and 7:00 PM, but only the results between 8:00 AM and 6:00 PM were used to represent the hours when the office is expected to be occupied. One day in each period (cloudy period and clear period) was used to calibrate the model, which equates to around 40 data points, while the rest of the data was used for validation.

Three types of measurements were taken: illuminance measurements in lux, irradiance measurements in $\frac{W}{m^2}$, and temperature measurements in °C. For the temperature, thermocouples were used. For illuminance and irradiance, the LI-210R sensors and the LI-200R sensors were used, respectively. LI-210R spectral response matches the CIE standard observer curve and is sensitive to light from all directions up to an incidence angle of 82 degrees (LI-COR, Inc., 2022b). At the same time, the LI-200R measures global solar radiation and has a uniform sensitivity up to 82 degrees incident angle (LI-COR, Inc., 2022a). The figure below shows the real-life images of the sensors are presented in Figure 3.4, and Table 3.1 provides specific details of operation for both. The placement of these sensors in each part of the test space is provided in more detail in their respective sections. The three considered locations for sensor placements are the outer glazing of the window, the inner glazing of the window, and the middle of the floor plan. The obtained data was used to validate the transmittance models used. This data can also be used on future projects to assess the thermal comfort of the indoor environment for example.

Figure 3.4: *Images of the pyranometer and photometer used in the experimental setup (LI-COR, Inc., 2022a; LI-COR, Inc., 2022b).*

	LI-210R Photometric Sensor	**LI-200R Pyranometer**
Detector	High stability silicon photovoltaic detector	High stability silicon photovoltaic detector
Size / Weight	2.36 cm diameter × 3.63 cm / 24 grams	2.36 cm diameter × 3.63 cm / 24 grams
Tilt	No error induced from orientation	No error induced from orientation
Temperature and Relative Humidity range	−40 °C to 65 °C 0% to 100% RH	−40 °C to 65 °C 0% to 100% RH
Cosine Correction	Cosine corrected up to 82° angle of incidence	Cosine corrected up to 82° angle of incidence
Calibration	± 5%	± 3%

Table 3.1: *Properties of the photometer and pyranometer used in the experimental phase (LI-COR, Inc., 2022a; LI-COR, Inc., 2022b).*

- Outer Glazing of the window:

A total of 9 sensors were placed on the outside glazing: seven thermocouples, one pyranometer and one photometer. The figures below show a diagram of the sensor placement as well as the real setup used during the experiments. The purple section represents the insulation on top of the window. The sensors were used to obtain the external / outdoor irradiance, illuminance, and temperature. The rest of the thermocouples used are for measuring the temperatures at different locations on the glazing: top, center, and middle. At each point, two thermocouples are used: one for the glass portion and one for the PV portion. The higher temperature of PV cells is expected due to silicon's material properties and its absorption of a large amount of solar radiation compared to glass. Figure 3.5 shows the setup in the test cell and a simplified diagram of the sensor placement.

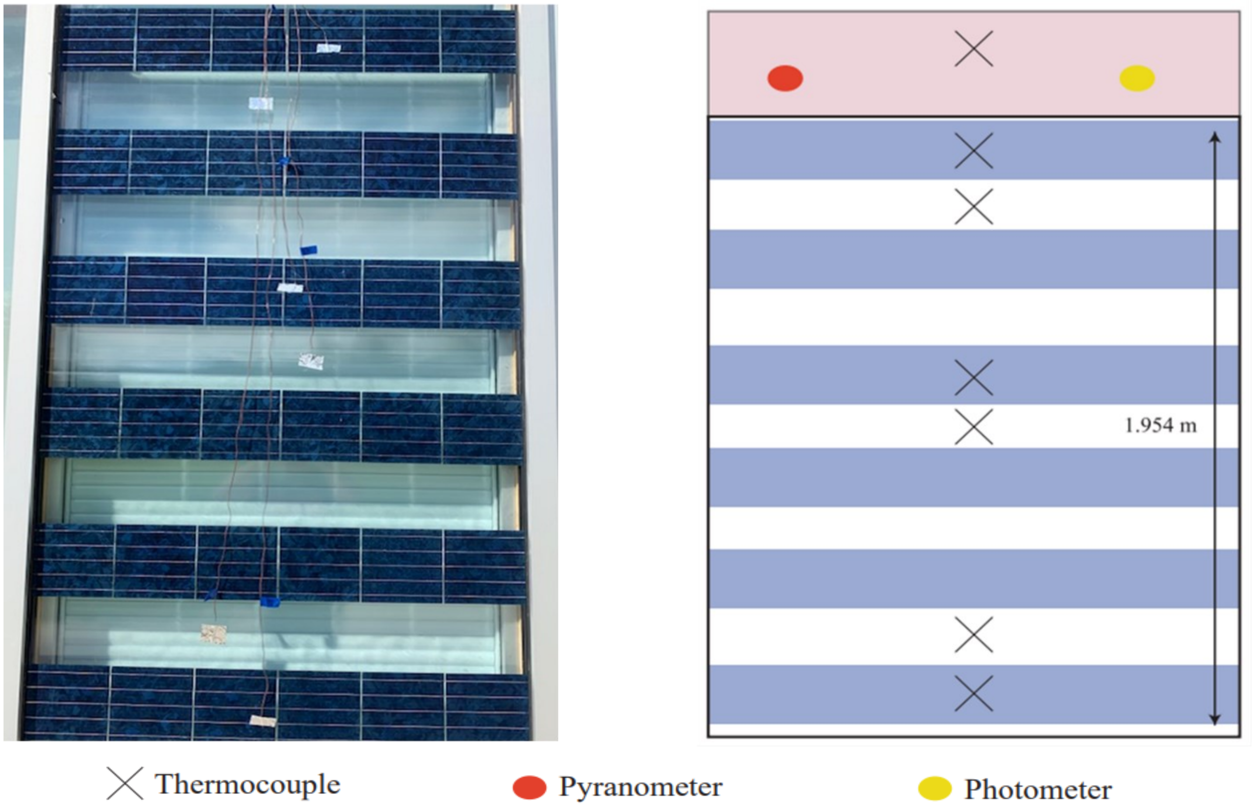

Figure 3.5: *Outer glazing experimental setup in test cell 4 (left) and simplified diagram (right).*

- Inner Glazing of the window:

A total of 14 sensors were used on the inner glazing of the window: 3 thermocouples, 7 photometers, and 4 pyranometers. The three thermocouples are used to measure the temperature of the glass at the top, middle, and bottom. The seven photometers and four pyranometers are closely arranged within a segment of the window that spans 0.325 meters, making up one-sixth of the window's total length. This section of the window is designed uniformly, mirroring the other segments in terms of the arrangement of PV cells, glass panels, and Venetian blinds. This setup allows us to account for variations in terms of transmitted illuminance and irradiance that can be caused by the different elements of the AFS without covering the entirety of the window in sensors (which would not be cost prohibitive). In addition, setting up the sensors in a closely tight formation helps reduce the error in obtained measurements. Grouping several sensors close together helps even out any spot differences in lighting, like those caused by small shadows or reflections. This approach can provide a more consistent and accurate average of the light levels in that particular spot. Figure 3.6 shows the inner pane setup during experimentation as well as a simplified diagram of the sensor placement.

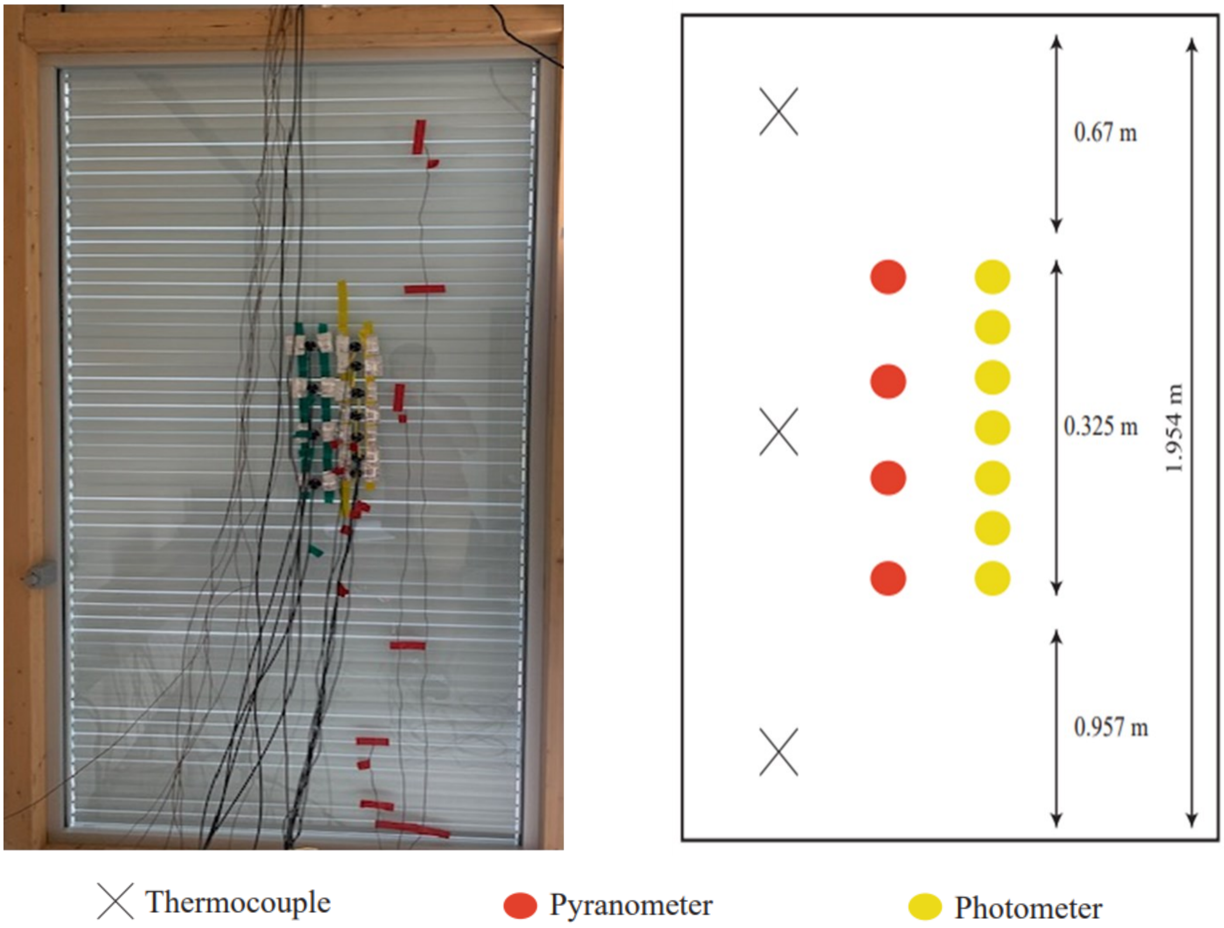

<u>Figure 3.6:</u> *Inner glazing experimental setup in test cell 4 (left) and simplified diagram (right).*

- Floor Plan:

A total of 7 sensors were used to obtain measurements on the floor plan. The sensors were placed on an adjustable desk at a height of 0.8 meters, which is considered as the work plane height. Three of the sensors were thermocouples. One was placed 0.525 meters from the window, one placed at the center of the room, and one was placed 0.525 meters from the door. This setup was used to determine the temperature variations caused by the transmitted irradiance. Expected results would show the temperature decreasing the further away the sensor is from the windows. A pyranometer was placed at the center of the room to measure the irradiance. Three photometers were placed at the same locations as the thermocouples to analyze the illuminance distribution based on the distance from the windows. Expected results would show the illuminance also decreasing the further away the sensor is from the windows. Figure 3.7 shows the floor plan setup during experimentation as well as a simplified diagram of the sensor placement.

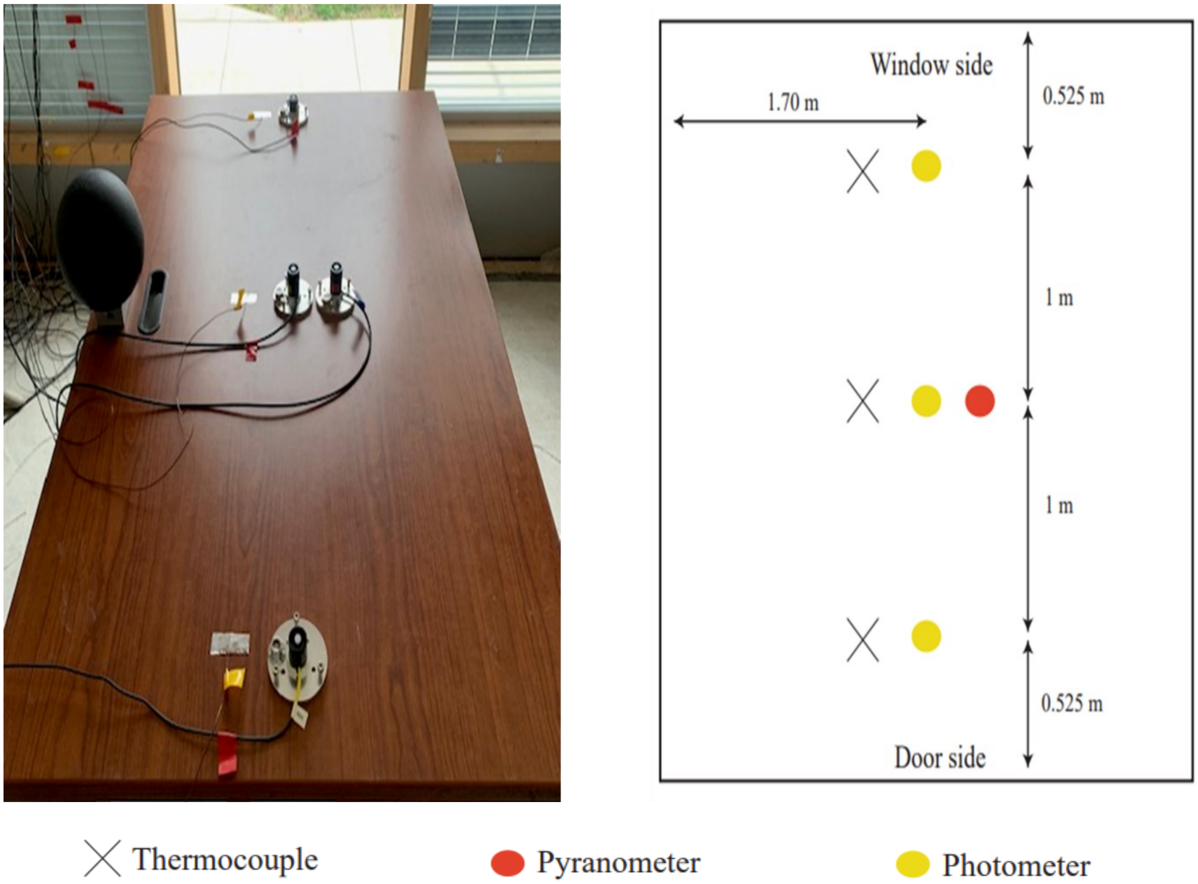

Figure 3.7: *Floor plan experimental setup in test cell 4 (left) and simplified diagram (right).*

3.2- Modeling the Transmittance

Two visual transmittance models were developed in order to mimic the real-life daylight transmittance properties of the advanced fenestration system under clear and cloudy sky conditions. The transmittance model helps with estimating the work plane illuminance and the glare levels in the office space at any time during the day so that the tilt angle can be adjusted to optimize visual comfort levels while also allowing the maximum amount of solar passive gains. The transmittance model for clear days is labeled as $\tau_{model,clear}$, while the model for cloudy days is labeled as $\tau_{model,cloudy}$ throughout the document. They represent one of the main contributions of this research.

In order to estimate the accuracy of the developed transmittance under different scenarios, two other models were calculated and used as a benchmark. They are calculated based on equations found in previous literature and Snell's law. The clear sky conditions model is labeled as $\tau_{lit,clear}$, while the cloudy sky conditions benchmark model is called $\tau_{lit,cloudy}$, to reference the fact that they were inspired by previous visual comfort studies. In both cases, the model is the product of a transmittance model developed by Athienitis & Tzempelikos (2002) and another transmittance model that was calculated using Snell's law and an area ratio between silicon and glass to represent the outer PV glazing of the fenestration. The transmittance equations by Athienitis & Tzempelikos (2002) are labeled as $\tau_{clear,middle\ glazing}$ and $\tau_{cloudy,middle\ glazing}$ for clear and cloudy days, respectively, because they represent the transmittance of the middle portion of the AFS (including the venetian blinds). The transmittance for the outer PV glazing is labeled as τ_{outer} for both cases. All the models are used to calculate the work plane illuminance, which is then compared to the experimental results in order to analyze the improvements that $\tau_{model,clear}$ and $\tau_{model,cloudy}$ bring to the body of literature. This section will present both models and the equations used. The validation of the data driven model and the comparison between all the models will be discussed in chapter 4.

3.2.1- Data Driven Models

- Clear Sky Conditions:

The data driven model presented is $\tau_{model,clear}$ and it represents one of the contributions of this work. It was developed based on the experimental results that were obtained in the test cell for clear days. This model encapsulates the total visual transmittance of the studied AFS, including the three levels of glazing, the venetian blinds, and the PV cells: As the sun moves throughout the day, each element of the window impacts the visual transmittance in a separate manner and needs to be considered when discussing the total transmittance. The model is the product of a function based on the blind tilt angle β and another function based on the incidence angle of the sun θ. Based on experimental results, the transmittance of the window behaves differently for different ranges of β. For smaller blind tilt angles, which in this case refers to a blind tilt angle between 0 degrees and 45 degrees, the transmittance $\tau_{model,clear}$ follows a normal distribution approximation with reference to the blind tilt angle multiplied by a third-degree polynomial which represents the variation of τ_{model} with respect to the incidence angle.

However, for larger blind tilt angles, which in this case refers to β between 45 degrees and 90 degrees (excluding 90), τ_{model} follows a bimodal distribution approximation with reference to the blind tilt angle multiplied by a third-degree polynomial that represents the variations of the transmittance based on the incidence angle. For the case where $\beta = 90$ (the blinds are in a vertical position), the shading device acts like a completely opaque surface since the blinds are highly reflective. Thus, the transmittance is assumed to be completely negligeable. This assumption is supported by the experimental results obtained for this specific tilt angle: the obtained transmittance is close to 0, similar to the work plane illuminance. The coefficients of the normal distribution, bimodal distribution, and both third-degree polynomials were obtained using a minimization optimization function. Equation 3-1 shows the final obtained model that was later on integrated into the control strategy,

$$\boldsymbol{for\ 0 \le \beta < 45}:$$

$$\tau_{model,clear} = \frac{1}{2.32 \cdot 10^{13} \times \sqrt{2.5}} \times \exp\left(-0.5\ \times \left(\frac{\beta - 2.38 \cdot 10^{13}}{2.32 \cdot 10^{13}}\right)^2\right) \cdot \left(-(2.9 \cdot 10^7)\theta^3 + (6.4 \cdot 10^9)\theta^2 - (6.63 \cdot 10^9)\theta - 1.73 \cdot 10^{11}\ \right)$$

$$\boldsymbol{for\ 45 \leq \beta < 90}:$$

$$\tau_{model,clear} = (0.93 \cdot \frac{1}{2.95 \cdot 10^{8} \times \sqrt{2.5}} \times \exp\left(-0.5 \times \left(\frac{\beta - 1.65 \cdot 10^{9}}{2.95 \cdot 10^{8}}\right)^{2}\right) + (1 - 0.93)$$

$$\cdot \frac{1}{2.2 \cdot 10^{8} \times \sqrt{2.5}} \times \exp\left(-0.5 \times \left(\frac{\beta - 7.28 \cdot 10^{8}}{2.2 \cdot 10^{8}}\right)^{2}\right)$$

$$\times (-(6.57 \cdot 10^{7})\theta^{3} + (4.19 \cdot 10^{9})\theta^{2} - (6.36 \cdot 10^{10})\theta - 1.85 \cdot 10^{11})$$

$$\boldsymbol{for\ \beta = 90}:$$

$$\tau_{model,clear} = 0 \qquad (3\text{-}1)$$

Where β is the blind tilt angle of the venetian blinds in degrees, θ is the incidence angle of the sun in degrees, and $\tau_{model,clear}$ is the transmittance.

- Cloudy Sky Conditions:

The data driven model presented here is $\tau_{model,cloudy}$ and it also represents one of the contributions of this work. It was developed based on the experimental results that were obtained in the test cell for cloudy days. This model encapsulates the total visual transmittance of the studied AFS, including the three levels of glazing, the venetian blinds, and the PV cells. Under cloudy conditions, the behavior of the window is similar for all blind tilt angles. The model is also the product of a function based on β and a function based on θ. In this case, the shape of the first function was inspired by Athienitis & Tzempelikos (2002), and the optimal coefficients obtained using a minimization optimization function. The function based on θ is a first-degree polynomial that is used as a correction factor based on the sun's position. This part of the model plays an important role in adjusting the illuminance during mid-day, where the incidence angle is at its highest. Its coefficients were also obtained using a minimization optimization function. Equation 3-2 shows the final obtained model that was later on integrated into the control strategy,

$$\tau_{model,cloudy} = \frac{4.231 \cdot 10^{12} \cdot \beta^{-6.58}}{\exp\left(\frac{3.753 \cdot 10^{2}}{\beta}\right) - 1} \cdot (0.45\,\theta\, +\, 0.9773) \qquad (3\text{-}2)$$

Where β is the blind tilt angle of the venetian blinds in degrees, θ is the incidence angle of the sun in degrees, and $\tau_{model,cloudy}$ is the transmittance.

3.2.2- Model Derived from Previous Literature

The models presented in this section are $\tau_{lit,cloudy}$ and $\tau_{lit,clear}$. They represent the benchmark to which $\tau_{model,cloudy}$ and $\tau_{model,clear}$ are compared to, respectively, in order to assess its accuracy. The literature models are the product of a transmittance equation developed by Athienitis & Tzempelikos (2002) and another transmittance equation calculated using Snell's law. This is because the first equations were developed for a double-glazed window with highly reflective aluminium inner pane venetian blinds. The second equation is used to account for the outer glazing which has the silicon semitransparent photovoltaic cells. They are based on the main assumption that light transmitted through the PV cells on the outside glazing is not scattered, but rather refracted based on Snell's law. Snell's law states that:

$$n_1 \cdot \sin(\theta_1) = n_2 \cdot \sin(\theta_2) \tag{3-3}$$

Where n_1 is the refractive index of the first medium. In the case of air, the value of n_1 is 1.0. n_2 is the refractive index of the second medium. In the case of silicon, the value of n_2 is 3.5, while a common value for a glass surface is assumed to be 1.5. θ_1 represents the incidence angle of the sun and θ_2 is the angle of refraction. Figure 3.8 helps illustrate Snell's law in the case of the studied AFS.

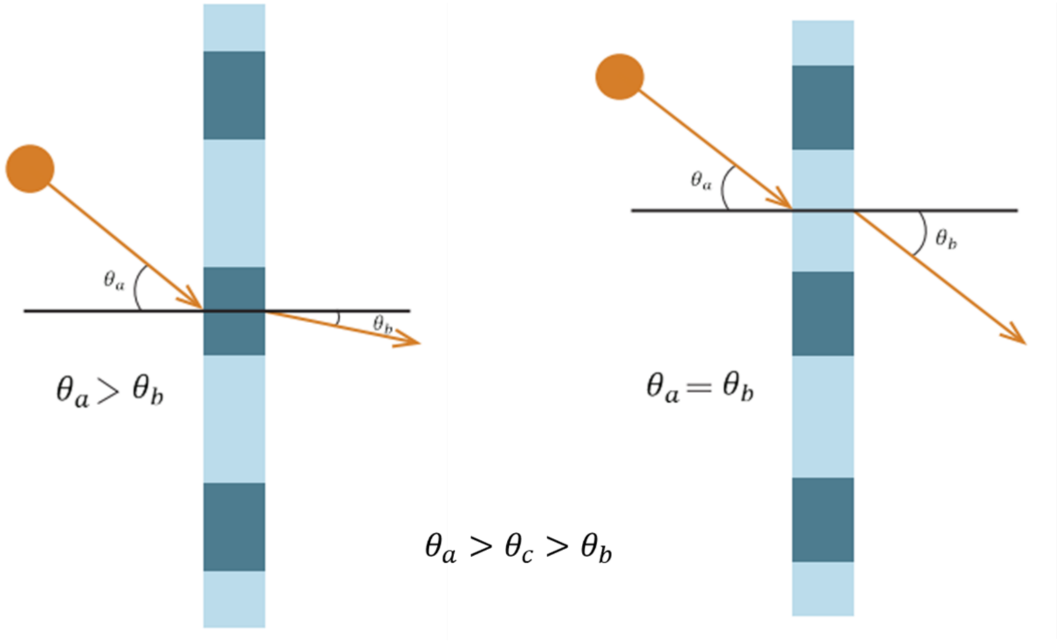

Figure 3.8: *Refraction diagram for light traveling through silicon (right) and through glass (left)*

With the assumption established, the literature visual transmittance equations are presented as follows:

$$\tau_{lit,clear} = \tau_{clear,middle\ glazing} \cdot \tau_{outer} \tag{3-4}$$

$$\tau_{lit,cloudy} = \tau_{cloudy,middle\ glazing} \cdot \tau_{outer} \tag{3-5}$$

$\tau_{clear,middle\ glazing}$ and $\tau_{cloudy,middle\ glazing}$ are the parts of the equation that represent the transmittance for the middle and inner glazing with the inner pane venetian blinds. The first is the product of a function with respect to the blind tilt angle and another function with respect to the incidence angle of the sun. However, $\tau_{cloudy,middle\ glazing}$ only depends on the blind tilt angle since the impact of the incidence angle is assumed negligeable under cloudy conditions. Athienitis & Tzempelikos (2002) studied a double-glazed window with the venetian blinds that was designed by the same company that manufactured the windows used in this study and installed in test cell 4 at the future building lab.

$$\tau_{clear,middle\ glazing} = 0.55 \exp\left(\frac{-(\beta - 80)^2}{1900}\right)(-4.917 \cdot \theta^4 + 0.00009 \cdot \theta^3 - 0.00567 \cdot \theta^2 + 0.13 \cdot \theta - 0.00437) \tag{3-6}$$

$$\tau_{cloudy,middle\ glazing} = \frac{4.5 \cdot 10^{12} \cdot \beta^{-6}}{\exp\left(\frac{335}{\beta}\right) - 1} \tag{3-7}$$

Where β is the blind tilt angle of the venetian blinds in degrees, θ is the incidence angle of the sun in degrees. $\tau_{cloudy,middle\ glazing}$ and $\tau_{clesr,middle\ glazing}$ are the transmittance.

τ_{outer} is the part of the equation that represents the transmittance of the outer glazing. It is calculated using Snell's law and the silicon to glass area ratio, such that:

$$\tau_{outer} = \frac{A_{silicon}}{A_{total}} \cdot \tau_{silicon} + \frac{A_{glass}}{A_{total}} \cdot \tau_{glass} \tag{3-8}$$

With τ_{outer} the outer glazing transmittance, $A_{silicon}$ the area of the glazing covered in PV, A_{glass} the area of the glazing covered in glass, A_{total} the total area of the glazing, $\tau_{silicon}$ the transmittance of the silicon, and τ_{glass} the transmittance of the glass.

The intermediate transmittances are obtained using Equation 3-9:

$$\tau_{silicon,glass} = \frac{(1 - \rho)^2 \cdot a}{1 - (a^2 - \rho^2)} \tag{3-9}$$

With ρ being the reflectivity and a the absorption.

These properties differ based on the material. For both the glass and the silicon, the reflectivity can be obtained using Fresnel's equation. It represents the ratio of light that is reflected off the material at each time step and is calculated using Equation 3-10:

$$\rho_{silicon,glass} = \frac{1}{2} \cdot [\left(\frac{\sin(\theta - \theta')}{\sin(\theta + \theta')}\right) + \left(\frac{\tan(\theta - \theta')}{\tan(\theta + \theta')}\right)] \tag{3-10}$$

Where θ is the incidence angle of the sun at a specific time step and θ' is the refraction angle at that specific time step.

The refraction angle refers to the angle at which the sun rays are transmitted once they pass through the specified material. Using Snell's law, it is calculated using Equation 3-11:

$$\theta' = \arcsin(\frac{\sin\theta}{n}) \tag{3-11}$$

With n being the refractive index of the material. In the case of silicon, $n_{silicon}$ is equal to 3.5. For glass, n_{glass} is 1.5.

At the same time, the absorption a representes the ratio of light that is absorbed by the material at each time step. It is calculated using the Beer-Lambart law and is equal to:

$$a_{silicon,glass} = \exp(-k \cdot t') \tag{3-12}$$

where k is the absorption coefficient of the material, a measure that describes how much light (or other electromagnetic radiation) is absorbed when it travels through a given material.

The coefficient quantifies the amount of light absorbed per unit distance of the medium. For silicon, the absorption coefficient is $k_{silicon}$ equal to 0.019. In the case of glass, k_{glass} is equal to 6.96. t' is the effective thickness of the material at a specific time. It refers to how thick a material effectively behaves or performs under specific conditions, rather than its actual physical thickness. t' can be obtained using Equation 3-13:

$$t' = \frac{t}{\sqrt{1-\left(\frac{\sin\theta}{\theta'}\right)^2}} \tag{3-13}$$

Where t is the actual thickness of the material in meters, θ is the incidence angle of the sun, and θ' is the refraction angle of the sun.

Once the intermediate transmittances $\tau_{silicon}$ and τ_{glass} are obtained, the area ratios are used as a factor for each of them. Based on the manufacturer's data sheet, the packing factor PF of the glazing is 45.9%. Thus, the ratio of silicon with regards to the total area of the glazing is given by Equation 3-14:

$$\frac{A_{silicon}}{A_{total}} = PF = 0.459 \tag{3-14}$$

The ratio of glass with regards to the total area of the glazing can then be obtained through Equation 3-15:

$$\frac{A_{glass}}{A_{total}} = 1 - PF = 0.541 \tag{3-15}$$

Through the method outlined, the overall transmittance at each time step can be precisely determined by incorporating variables such as the blind tilt angle and the incidence angle.

3.2.3- Root Mean Square Error

The root mean square error (RMSE) is a standard measurement of the accuracy of a model that compares predicted values with observed actual values. It is a measure of how well a regression model predicts outcomes. The lower the RMSE, the more accurately the model predicts. The root mean square error is calculated as follows:

$$RMSE = \sqrt{\frac{1}{n}\sum_{i=1}^{n} y_i^{observed} - y_i^{predicted}} \tag{3-16}$$

Where n is the total number of data points, $y_i^{observed}$ is the observed value (experimental values), and $y_i^{predicted}$ is the predicted values (theoretical results).

In order to assess the improvement of the data driven model compared to the models from previous literature models, the RMSE was used to estimate how close the theoretical illuminance values calculated (using these models) are to the experimental results obtained. For a specific day, if the total RMSE using the data driven models is less than the total RMSE using the literature derived model, this means that the first model is more accurate since it is more similar to the experimental results. Thus, a valid conclusion would be that the model with the smallest RMSE relative to the experimental data is more accurate.

3.3- Daylight Calculations

This section will present the equations used in the control strategy to calculate the different variables that will lead to obtaining the work plane illuminance and the simplified daylight glare probability at each time step. A simplified flow of these calculations is presented in Figure 3.9. From the sun calculations, the incidence angle and the altitude of the sun are obtained. These variables are then used to obtain the incident daylight, the transmitted daylight, and the different values of the transmittance based on outside weather conditions.

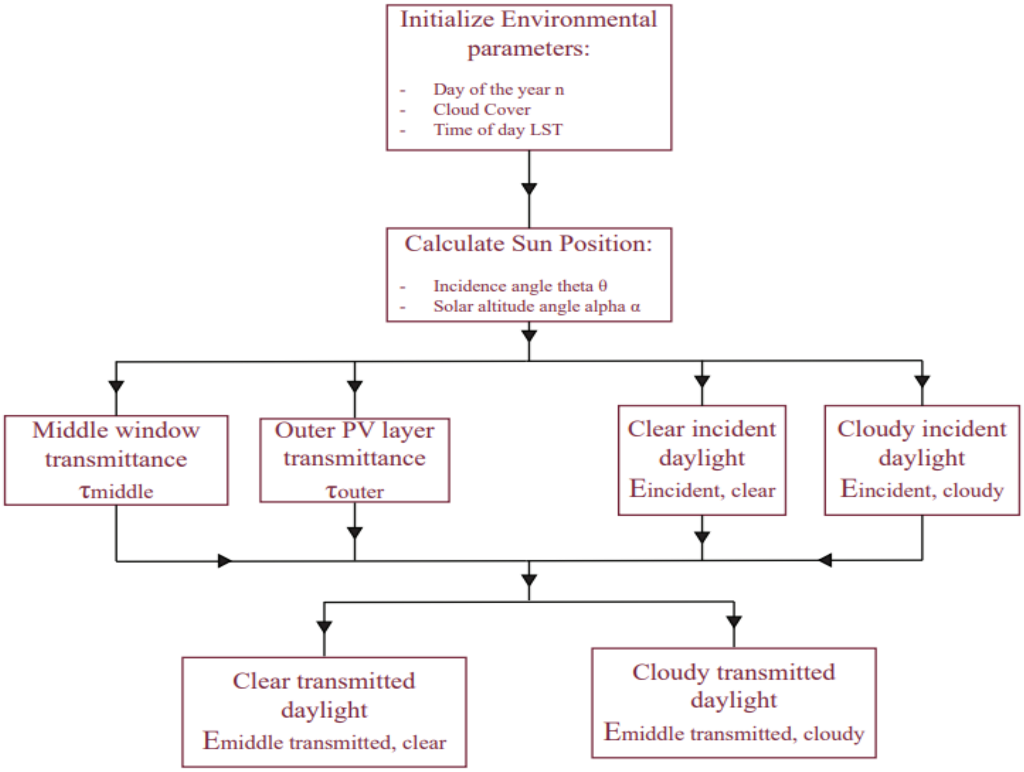

<u>Figure 3.9:</u> *Sun position and incident daylight calculations flowchart*

3.3.1- Sun Position Calculations

Sun position for each time step are calculated using the below equations for intermediate variables, with the final aim of obtaining the incidence angle θ and the solar altitude α.

$$ET = 9.87\, sin\left(4\pi \cdot \frac{n-81}{364}\right) - 7.53\, cos\left(2\pi \cdot \frac{n-81}{364}\right) - 1.5\, sin\left(2\pi \cdot \frac{n-81}{364}\right) \tag{3-17}$$

$$AST = LST + 4 \cdot (LSM - LON) + ET \tag{3-18}$$

$$h = \ 15 \cdot (AST - 12) \tag{3-19}$$

Where ET is the equation of time in minutes which describes the difference between the actual time shown on a clock and the apparent solar time AST. n stands for the day of the year, LST stands for the local standard time, LSM stands for the local standard meridian equal to 75 for the city of Montreal, and LON stands for the longitude which in the case of Montreal is equal to 73.6. h is the hour angle in degrees which is a measure of time since solar noon.

Based on these variables, solar angles can be calculated using Equations 3-20 to 3-24.

$$\delta = 23.45 \cdot sin\ (2\pi \cdot \frac{284+n}{365}) \tag{3-20}$$

$$\alpha = asin\ [cos(LAT) \cdot cos(\delta) \cdot cos(h) + sin\ (LAT) \cdot sin\ (\delta)] \tag{3-21}$$

$$\varphi = acos\ [\frac{sin(\alpha) \cdot sin(LAT) - sin(\delta)}{cos(\alpha) \cdot cos(LAT)}] \cdot \frac{h}{abs(h)} \tag{3-22}$$

$$\gamma = \ \varphi - \ \psi \tag{3-23}$$

$$\theta = acos\ [cos(\alpha) \cdot cos\big(abs(\gamma)\big) \cdot sin(\beta_{window}) + sin\ (\alpha) \cdot cos\ (\beta_{window})] \tag{3-24}$$

Where δ is the declination angle which represents the angle between the rays of the sun and the plane of the Earth's equator, α is the solar altitude angle which is the angle between the horizontal plane and the line to the sun, φ is the solar azimuth angle, γ is the solar surface azimuth angle, and

θ is the incidence angle of the sun.

The constants used for these equations are the latitude LAT equal to 45 in Montreal, the tilt angle of the windows β_{window} equal to 90 since they are vertical, and the surface azimuth ψ equal to 0 since the office space is facing south.

3.3.2- Incident Daylight Calculations

Two equations were used to calculate the incident daylight on the windows at each time step: one based on clear outdoor conditions and the other based on cloudy outdoor conditions. The equations were obtained from Athienitis & Tzempelikos (2002), which uses equations based on the Murdoch (1985). However, in a real-life application, the incident daylights at each time step can be obtained using photometers set on the outer side of the AFS. For an overcast sky, the daylight incident on the window $E_{incident,cloudy}$ in lux is given by Equation 3-25:

$$E_{incident,cloudy} = 500 \cdot (0.3 + 21 \cdot sin(\alpha)) \cdot (1 + \rho_g) \tag{3-25}$$

With α the solar altitude angle at that time step and ρ_g is the reflectance of the ground equal to 0.4 for cement / concrete.

For a clear sky, the equation of $E_{incident,clear}$ in lux is:

$$E_{incident,clear} = E_{ground} + E_{sky} + E_{sun} \tag{3-26}$$

With E_{ground} the daylight that is reflected off the ground and reaches the window, E_{sky} is the daylight that is reflected and diffused in the atmosphere reaching the window, and E_{sun} is the beam direct sunlight.

They are calculated using the Equations 3-27 to 3-29:

$$E_{ground} = F_{w-g} \cdot \rho_g \cdot E_{h,total} \tag{3-27}$$

$$E_{sky} = F_{w-sky} \cdot E_{h,sky} \tag{3-28}$$

$$E_{sun} = E_o \cdot f \cdot exp\,(-c.\frac{1}{sin(\alpha)}) \cdot cos\,(\theta) \tag{3-29}$$

With F_{w-g} and F_{w-sky} the view factors between the window and the ground, and the window and the sky, respectively. ρ_g is the previously mentioned ground reflectance and c is the optical atmospheric extinction coefficient. E_o represents the average illuminance on a surface oriented directly towards the sun just outside the Earth's atmosphere, and f is a correction factor to account for the elliptical shape of the Earth's orbit around the sun.

For this case, F_{w-g} and F_{w-sky} are assumed to be equal to 0.5 since there are no obstructions. c is equal to 0.21 under clear sky conditions, and E_o is estimated to be equal to 133 800 lux by CIE 85 (1989). f is obtained using Equation 3-30:

$$f = 1 + 0{,}033 \cdot cos\,(360 \cdot \frac{n}{365}) \tag{3-30}$$

With n the number of the day of the year.

$E_{h,sky}$ is the horizontal illuminance due to the sky in lux and is calculated using Equation 3-31:

$$E_{h,sky} = 800 + 15\,500 \cdot sin^{1/2}(\alpha) \tag{3-31}$$

With α the solar altitude.

Finally, $E_{h,total}$ is the total horizontal illuminance in lux and is the sum of the horizontal illuminance due to the sky $E_{h,sky}$ and the solar horizontal illuminance $E_{h,sun}$. $E_{h,sun}$ is calculated using Equations 3-32 and $E_{h,total}$ is calculated using Equation 3-33:

$$E_{h,sun} = E_o \cdot f \cdot exp\,(-c.\frac{1}{sin(\alpha)}) \cdot sin\,(\alpha) \tag{3-32}$$

$$E_{h,total} = E_{h,sun} + E_{h,sky} \tag{3-33}$$

With E_o the average illuminance on a surface oriented directly towards the sun just outside the

Earth's atmosphere, f a correction factor to account for the elliptical shape of the Earth's orbit around the sun obtained from Equation 3-30, c is the optical atmospheric extinction coefficient, and α is the solar altitude.

3.3.3- Transmittance and Transmitted Daylight Calculations

The transmittance equations that are used in the control strategy are the data driven models discussed. As a summary, $\tau_{model,clear}$ is used to obtain the transmittance of the windows under clear sky conditions, and $\tau_{model,cloudy}$ is used to obtain the transmittance of the windows under cloudy sky conditions. In terms of incident daylight, $E_{incident,clear}$ represents a clear day and $E_{incident,cloudy}$ represents a cloudy day

The transmitted daylights are obtained by multiplying the incident daylight with the transmittance based on the outdoor conditions at the specific time step following Equation 3-34 and 3-35:

$$E_{transmitted,clear} = E_{incident,clear} \cdot \tau_{model,clear} \tag{3-34}$$

$$E_{transmitted,cloudy} = E_{incident,cloudy} \cdot \tau_{model,cloudy} \tag{3-35}$$

3.3.4- Radiosity Analysis

In order to obtain the necessary indices to quantify the output of the control strategy, a radiosity analysis using the transmitted daylights must be conducted. In a generalized case, the interior surface of the window acts as a diffuse luminous source, dispersing daylight in all directions within the room. A typical office space is modeled into 7 surfaces: the window, the 4 walls, the ceiling, and the floor. The presence of a luminaire within the space can change this layout. It can either be considered as a separate surface, or it can be integrated within the ceiling, giving the ceiling an initial luminous exitance. The window's initial luminous exitance is equal to the transmitted daylight through them at each time step. To obtain the final luminous exitance of each surface, Equation 3-36 must be solved.

$$M_i = M_{0i} + \rho_i \cdot \sum_j M_j \cdot F_{ij} \tag{3-36}$$

Where M_i is the final luminous exitance of surface i in lux, M_{0i} is the initial luminous exitance of surface i in lux. ρ_i is the reflectance of that surface and F_{ij} us the view factor between the surfaces i and j.

This equation needs to be solved for each of the surfaces, thus a system of equations needs to be developed. In the form of a matrix equation, the equation is given by:

$$M = (I - T)^{-1} \cdot M_0 \tag{3-37}$$

Where M is a i x 1 matrix where each row represents a surface. M_0 is the initial luminous exitance i x 1 matrix similar to M. I is a i x i identity matrix, T is also a i x i matrix whose elements are the product of the reflectance of a surface and the view factor of that surface with the other surfaces.

Each element of T is obtained by solving Equation 3-38:

$$T_{ij} = \rho_i \cdot F_{ij} \tag{3-38}$$

With ρ_i the reflectance of surface i and F_{ij} is the view factor between the surfaces i and j.

The matrix equation is solved for each tilt angle at every time step. The reflectance of each surface can be either measured or obtained from a reference office space. However, since the transmittance of the window evolves at every time step, the reflectance would also change. Fresnel's equation can then be used to obtain ρ.

The view factors represent the fractions of all the light (luminous exitance) leaving surface i that strikes surface j directly. It is calculated based on the geometry of the room and the way each surface is in contact with the other surfaces within the same space. The same concept of view factors is also used in heat transfer. The view factor F is a i x i matrix that is constant (does not vary at each time step) where each row and each column represent a surface within the model. Some of the most important properties of view factors is that the view factor of a surface with itself is equal to 0 if it is flat (which is usually the case for a standard office space), and that the sum of the view factors of a surface to all other surfaces is equal to 1. Figure 3.10 shows a two-dimensional overview of the surfaces of a reference office space.

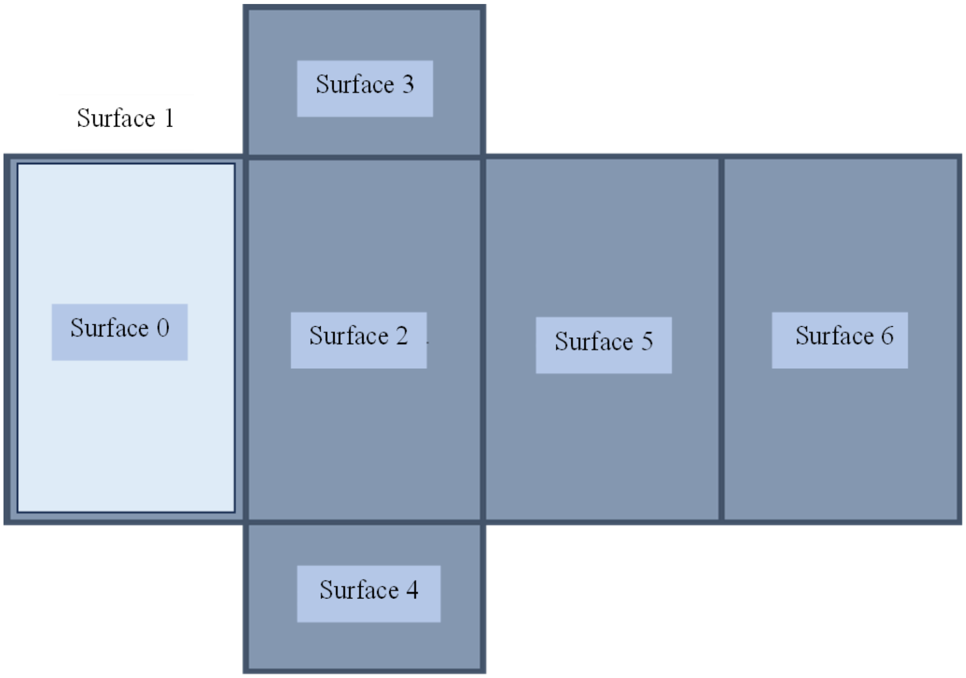

Figure 3.10: *Two-dimensional surface breakdown of a reference office space.*

3.3.5- Work Plane Illuminance Calculations

Using the final luminous exitances obtained from the radiosity analysis, the work plane illuminance can be calculated. It measures the amount of light that falls on the specified point in the space. Since the focus is the work plane illuminance, this point should be at the desk height, which is assumed to be 0.8 meters. Furthermore, since the considered space is a single person office setting, the point chosen for reference should be the center of the room, with an equal distance between the south / north walls and east / west walls. Equation 3-39 is used to obtain the illuminance at point p within the space:

$$E_p = \sum_i M_i \cdot c_{pi} \tag{3-39}$$

Where E_p is the work plane illuminance at point p in lux, M_i is the final luminous exitance of surface i obtained from the radiosity analysis in lux, and c_{pi} is the configuration factor between point p and surface i.

c_{pi} It is defined as the ratio of the illuminance on a differential area represented by point p, which results from the direct flux coming from surface i due to its luminous exitance. It is calculated based on the geometry of the space. The work plane illuminance is calculated for all the potential blind tilt angles at every time step to find the optimal one. For reference, an acceptable work plane illuminance to conduct daily office tasks is 300 lux based on Reinhart, Jakubiec, and Ibarra (2013). A higher work plane illuminance than the threshold is preferred but a lower one means that artificial lighting must be turned on to ensure visual comfort.

3.3.6- Simplified Daylight Glare Probability Calculations

Glare is the second index used in this paper to assess visual comfort within the office space. The simplified daylight glare probability $DGPs$ is used as a metric. Developed by Wienold (2007), it is a simplified version of daylight glare probability DGP built on the correlation between the glare perception and the vertical illuminance at eye level in the case where the sunlight is not directly hitting the eye of the occupant. Figure 3.11 underlines this correlation as presented in the work of Wienold (2007),

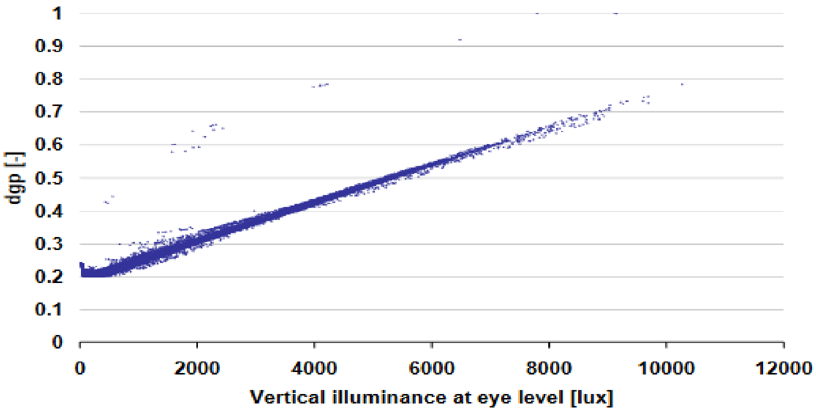

Figure 3.11: *Correlation between DGP and vertical illuminance at eye level (Wienold, 2007).*

The $DGPs$ is therefore based on the vertical illuminance at the eye level and is calculated using the following equation:

$$DGPs = 6.22 \cdot 10^{-5} \cdot E_v + 0.184 \qquad (3\text{-}40)$$

Where E_v is the vertical illuminance at eye level in lux.

The sum of all the luminous exitances from the surfaces within the occupant's eyesight represent the value of E_v at each time step. Just like illuminance, there is a threshold value that will lead to discomfort levels if surpassed. However, glare levels are set in categories. They can be set into one of three intervals: imperceptible, perceptible, and disturbing (Wienold, 2010). Imperceptible glare is the optimal interval where no discomfort or disturbance is caused to the occupant of the space. Perceptible glare is noticeable by the occupant but does not hinder the ability to complete the necessary tasks in the indoor environment. Finally, disturbing glare causes considerable discomfort and can make it hard to complete tasks. The intervals vary based on the type of glare index that is being used. For DGP and $DGPs$, the intervals are summarized in Table 3.2, based on Wienold (2010). Overall, Visual comfort is obtained when the amount of light and glare levels remain within the acceptable threshold regions. However, an increase in illuminance leads to an increase in the glare probability. Visual comfort therefore becomes a trade-off between both metrics to find an illuminance equal or greater than 300 lux, while keeping the DGPs below the imperceptible threshold of 0.35.

Glare Level	Interval
Imperceptible	≤ 0.35
Perceptible	≤ 0.40
Disturbing	≤ 0.45

Table 3.2: *Daylight glare comfort classes.*

3.4- Control Strategy

The data-driven visual transmittance models developed and discussed in section 3.3 are helpful to predict the transmittance of the window throughout a given time period but do not have any added value to the office space as a stand-alone contribution. They have to be integrated into a control scheme that would use the output provided by the model to make real-life decisions to ensure that the simulated office space is a comfortable and energy efficient environment. The control strategy presented in this section was built based on this approach.

The control strategy presented in this section chooses the optimal tilt angle at every 15-minute time step using as input the outdoor environmental conditions and the geometric / physical properties of the indoor space and windows (the geometrical properties are the dimension of the space and the reflectance of the surfaces that are integrated into the strategy through the view factors and the configuration factors). The strategy is therefore scalable for any indoor environment as long as this type of advanced fenestration technology is used. Intermediate calculations involve the incident daylight on the window, the transmitted daylight, and the transmitted daylight through the middle window (which is double glazed and does not have any PV cells installed on the exterior). These variables are calculated using the equations from section 3.3, obtained from literature. They depend on elements like the occupancy schedule of the office, the outdoor cloudiness levels, and the profile angle at every time step.

Based on these intermediate calculations, the work plane illuminance E_p and the simplified daylight glare probability $DGPs$ are obtained. These values are essential indicators of the indoor visual comfort levels. They are used to deciding on the optimal tilt angle of the blinds at each 15-minute time. The optimization approach is then decided based on the previously stated inputs. A simplified linear flowchart is shown in Figure 3.12 to provide a general idea of the flow of the control strategy.

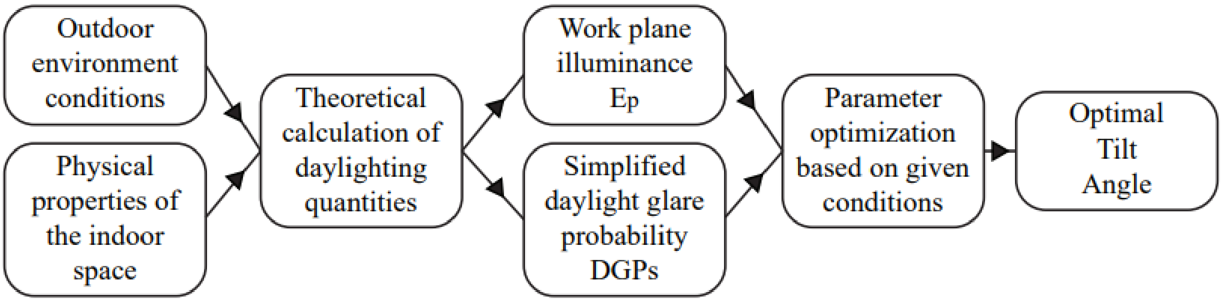

Figure 3.12: *Simplified flowchart of the control strategy.*

The control strategy presented using the data driven transmittance models $\tau_{model,clear}$ and $\tau_{model,cloudy}$ represent another contribution of this thesis.

The objective of this section is to present and discuss in detail the developed control strategy and its operation. The first sub-section will present a description of the overall functionality and how each decision-making approach is different based on the occupancy schedule and the outdoor environmental conditions. The next sub-section will provide a simplified flowchart of the control strategy to be used as reference by the reader. This flowchart also presents the nomenclature that is used throughout this part of the thesis for each calculated variable. The results and analysis of the obtained output from the CS will be discussed in chapter 4.

3.4.1- Description

The control strategy loops every 15-minutes and chooses an optimal tilt angle for that time step. A 5-minute time step would be distracting for the occupant and a time step longer than 15 minutes might have a negative impact on the visual comfort of the space. The algorithm also only runs during the occupancy period of 8:00 AM to 6:00 PM, with an expected two-hour lunch break from 12:00 PM to 2:00 PM. Outside this timeslot, the tilt angle of the blinds is set to completely horizontal (0 degrees). This occupancy schedule can be modified to fit the needs of the user.

The first step of the control strategy is to assess the sky calculations. In a real-life application, sensors set up on the outside of the space can determine these variables at each time step. However, for the simulation, these variables were obtained using input from a weather file. They mainly include the day of the year, the cloud cover, and the time-of-day LST (local sidereal time). These calculations are used to obtain the position of the sun at every time step, most notably the solar altitude angle α and the incidence angle θ. With these two angles, the location of the sun can be determined every 15 minutes.

The next step of the algorithm is to calculate the incident daylight on the windows. The incident daylight equation differs based on cloudiness level. A time step with a cloudiness level of 4 or above (the maximum being 8) is considered "cloudy" while a time step with a cloudiness level of less than 4 (the minimum being 0) is considered "clear". The equations of the incident daylight depend on the outdoor conditions. For a clear day, the altitude angle of the sun, the incidence angle, and the day of year are needed. However, for a cloudy day, only the altitude angle is required. $E_{incident,cloudy}$ refers to the incident daylight during a cloudy time step while $E_{incident,clear}$ refers to the incident daylight during a clear time step.

Based on the sun position and the incident daylight calculations, the visual properties of any window in the space that is not an advanced fenestration system can be obtained. First, the transmittance of the window is calculated based on the incidence angle of the sun using Snell's law. This transmittance is then multiplied by the transmittance of the shading device used for the specific case. The transmitted daylight of the generic window, for both clear and cloudy days, can then be obtained using the transmittance and the incident daylight. For a cloudy day, the transmitted daylight through this window is referred to as $E_{middle\ transmitted,cloudy}$. For a clear day, $E_{middle\ transmitted,clear}$ is used.

The next step of the control strategy is to categorize each time step within one of three categories based on the occupancy of the room and the outdoor cloudiness level: clear and unoccupied timestep, clear and occupied timestep, or cloudy timestep (for both occupied and unoccupied). These categories provide the necessary framework to first choose the correct equations for the variables and then choose the correct parameter optimization approach in order to ensure visual comfort and maximum passive solar gains. As previously stated, the two visual comfort indices that were used as reference are the amount of daylight, quantified using the work plane illuminance, and the glare levels, using the simplified daylight glare probability. The parameter optimization was done as follows:

- Clear and unoccupied timestep:

During a clear and unoccupied time step, the transmittance of the side windows (triple glazed with photovoltaic cells and inner-pane venetian blinds) is calculated using the previously discussed $\tau_{model,clear}$. The transmitted daylight $E_{transmitted}$ is then obtained based on the incident daylight $E_{incident,clear}$ and the respective transmittance. A radiosity analysis is then conducted to obtain the final luminous exitance of each surface M. Other than $E_{transmitted}$, the geometry of the room and the transmitted daylight through the middle window $E_{middle\ transmitted,clear}$ are used as inputs. The calculation of the work plane illuminance E_p and the simplified daylight glare probability $DGPs$ are conducted using M. At every time step, E_p is iteratively calculated for every potential tilt angle of the blinds and compared to the previous value. The maximum work plane illuminance found becomes $E_p max$ and its respective blind tilt angle is chosen as the optimal tilt angle β_{opt}. The efficiency of the control strategy on visual comfort are then quantified using E_p and $DGPs$ for that specific optimal tilt angle β_{opt}.

- Clear and occupied timestep:

During a clear and occupied timestep, glare level control becomes essential, therefore, instead of choosing the highest work plane illuminance, a hyperparameter optimization must be conducted to find the optimal level of E_p while keeping glare at acceptable levels. Furthermore, the profile angle d also plays an essential role. It is defined as the angle between the normal (perpendicular) to the window and the rays of the sun striking the window plane. This angle is crucial for determining the amount of solar radiation a window receives. d is calculated using Equation 3-41:

$$d = \tan^{-1}[\frac{\tan\,\alpha}{\cos\phi}] \tag{3-41}$$

Where α is the solar altitude angle and ϕ is the solar azimuth angle. If the profile angle is greater than 45 degrees for that specific time step, beam solar radiation can be neglected and the optimal tilt angle is set at 0 degrees to maximize view to the outside. In order to quantify the visual comfort at this blind tilt angle, similar calculations to obtain E_p and $DGPs$ are conducted. The transmittance of the window is calculated using the equation relevant to the control strategy considered. The transmitted daylight $E_{transmitted}$ is then obtained to conduct a radiosity analysis that will lead to the calculation of the work plane illuminance and glare levels.

However, for the case where the profile angle is less or equal to 45 degrees, a hyper parameter optimization is conducted. The initial step is to obtain the work plane illuminance and simplified daylight glare probability using the same steps as previously discussed for every potential blind tilt angle at that specific time step. Then the tilt angle which provides the highest E_p such that the $DGPs$ is below the value of 0.35 is chosen as the optimal tilt angle β_{opt}. Its respective work plane illuminance then becomes $E_p max$.

- <u>Cloudy unoccupied and occupied timestep:</u>

Occupancy schedule becomes irrelevant when dealing with a cloudy time step since glare is not an issue (glare is mainly caused by direct sunlight which is absent on a cloudy day). The control strategy in this case follows the same logic as the clear and occupied time step but uses different equations. First, the transmittance of the window is obtained using $\tau_{model,cloudy}$. The transmitted daylight $E_{transmitted}$ is then calculated by using as input the obtained transmittance and the incident daylight on a cloudy day $E_{incident,cloudy}$. A radiosity analysis is then conducted to obtain the work plane illuminance and the simplified daylight glare probability. At each time step, these calculations are done for every potential blind tilt angle starting at 0 degrees, with 5 degrees increments until 90 degrees. The algorithm compares each E_p to the previously calculated one to obtain the highest one. The highest work plane illuminance for that time step is labeled as $E_p max$

and its respective blind tilt angle is chosen as the optimal blind tilt angle β_{opt}. Its respective $DGPs$ is then used as an index to measure the glare levels at that specific time step.

Sub-section 3.4.2 will provide a simplified flow chart that summarizes the logic behind the choice of the optimal blind tilt angle at every time step.

3.4.2- Flowchart

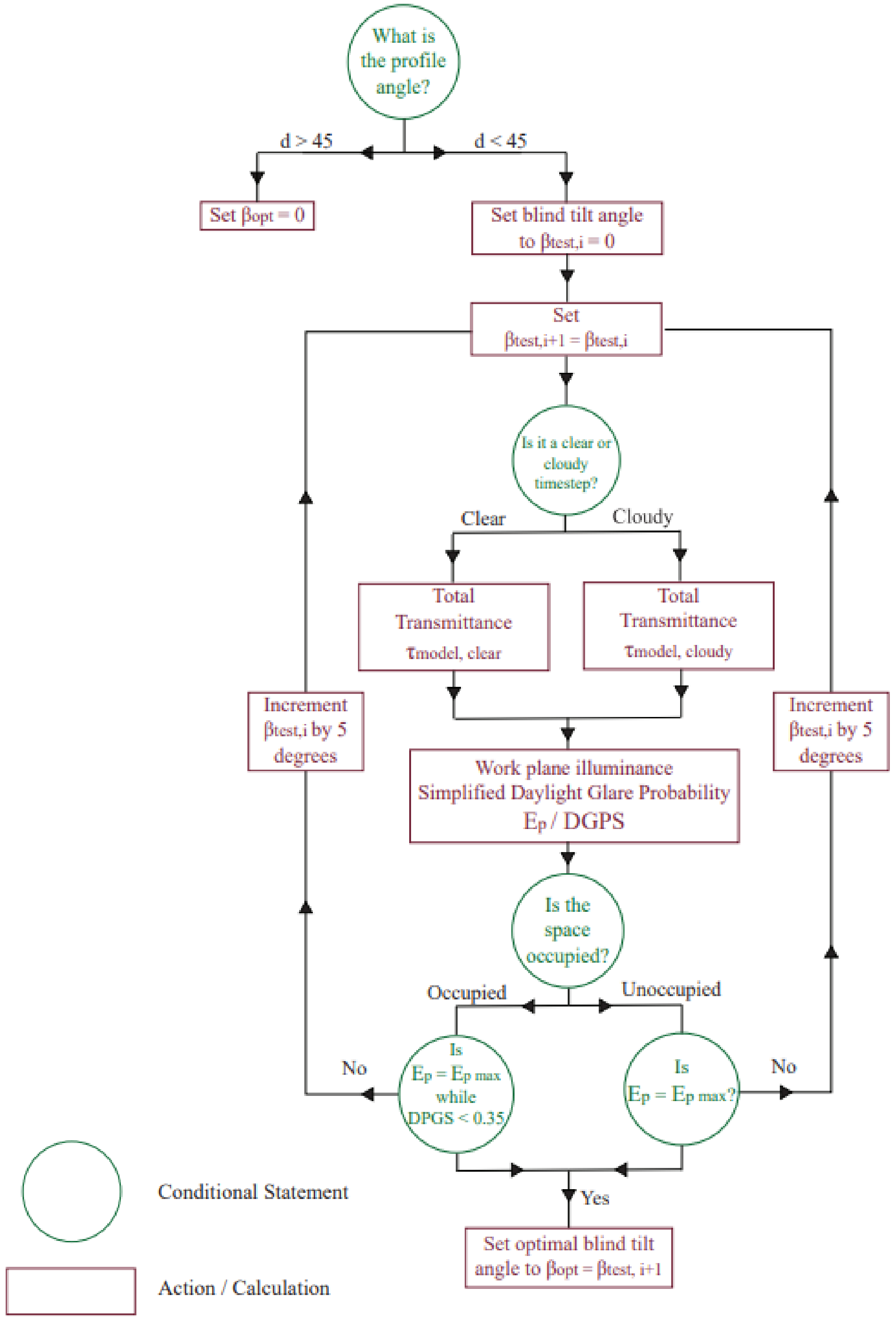

Figure 3.13: *Control strategy process.*

3.4.3- Control Strategy applied to the Case Study:

To evaluate the transmittance model accuracy and the control strategy results, the space was used as a test location for the simulations. Even though the control strategy presented in section 3.4 is scalable and can apply to any office space, some specifications must be inserted in the control approach to ensure the most precise output. The specifications that were added for this case study are presented in this section.

- <u>Radiosity Analysis:</u>

The room is modeled into 9 surfaces: the floor, the ceiling, the east wall, the west wall, the south wall (excluding the windows), the north wall, and the three windows. The latter are the only surfaces that are assumed to have an initial luminous exitance equal to the transmitted daylight through them at each time step. Figure 3.14 shows a two-dimensional overview of the surfaces of the room in the context of this model.

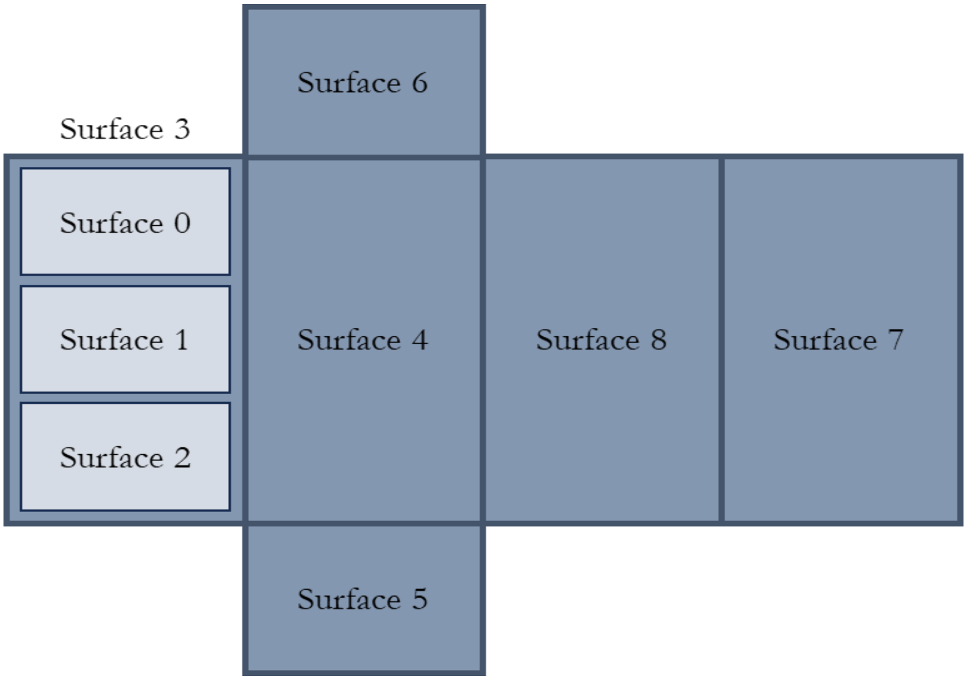

<u>Figure 3.14:</u> *Two-dimensional surface breakdown of the studied office space.*

Furthermore, to solve the radiosity equation, the reflectance of the surfaces was obtained based on Reinhart et al. (2006) for the opaque surfaces. For the windows, the reflectance varies according to Fresnel's equation. Table 3.3 summarizes the different reflectance applied to the simulation.

Building Element	**Reflectance**
Floor	0.3
Ceiling	0.8
Walls	0.6
Windows	Based on Fresnel's equation

Table 3.3: *Reflectance of different building elements in the test cell.*

- Work Plane Illuminance:

The work plane illuminance considered in the control strategy estimates the value at the center point of the room, which differs from one case to another based on the office space's dimensions. For this case study, the point p of interest where the illuminance is calculated is located at a height of 0.8 meters. In addition, the center of the room is at a distance of 1.7 meters from the east wall and 1.525 meters from the north wall.

- Simplified Daylight Glare Probability:

To calculate the $DGPs$, the vertical illuminance at eye level E_v is needed. For this case study, the occupant is sitting in the middle of the room facing the west wall, meaning that the sources of vertical illuminance are the west wall, the west window, half of the southern wall, half of the middle window, half of the northern wall, and half of the ceiling, the floor is considered covered by the desk. The sitting position of the occupant in this simulation is presented in the **Error! Reference source not found.**. The sum of all the luminous exitances from these surfaces represents the value of E_v at each time step. It is calculated using Equation 3-42:

$$E_v = \frac{E_{v,ceiling}}{2} + \frac{E_{v,south\ wall}}{2} + \frac{E_{v,north\ wall}}{2} + E_{v,west\ wall} + E_{v,window} + \frac{E_{v,middle\ window}}{2} \quad (3\text{-}42)$$

Where the vertical illuminance of each surface is calculated using Equation 3-43

$$E_{v,i} = \sum F_{i,v} \cdot M_i \quad (3\text{-}43)$$

With $F_{i,v}$ the view factor from surface i to the point on the vertical surface and M_i the final luminous exitance of surface i.

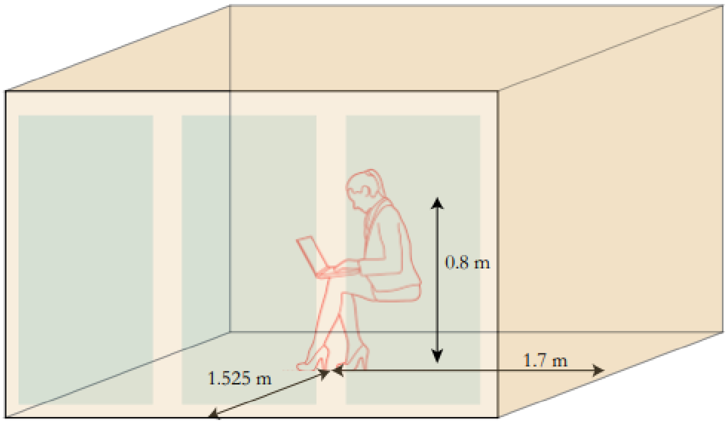

Figure 3.15: *Position of the occupant within the office space.*

3.5- Parametric Variation

To understand the impact of the physical parameters of the indoor environment on the visual comfort, a parametric variation of three parameters was tested on the case study space while using the control strategy. The parameters used are the window to wall ration (WWR), the room dimensions, and the reflectance of the opaque surfaces.

In terms of WWR, the office space has a window to wall ratio of 56%, with the three windows covering the vast majority of the south facing wall. WWR plays an essential role in determining the amount of natural daylight that can enter the space at any given time. The impact of the window size is indirectly related to illuminance calculation because it is used to calculate the view factor and the configuration factor. Two other values for the window to wall ratio were simulated to understand the impact it has on the work plane illuminance and the glare levels: a smaller WWR of 40% and a larger WWR of 80%.

The room size also plays an important role in determining the indoor illuminance level. The radiosity analysis applied to calculate E_p uses the dimensions and geometry of the space as an input in order to obtain the final luminous exitance M of each surface. M then determines the work plane illuminance (and the simplified daylight glare probability) based on the configuration factor of the surface with respect to the center of the room. To understand the effect room dimensions, have on visual comfort, the control strategy was applied on an office space half the size and double the size of the initial case study room, with the window to wall ratio remaining constant at 56%.

Another important aspect that significantly influences the illuminance levels is the reflectance of the surface. The reflectance represents the portion of light that an object reflects from the total incident light on its surface. In real life, the reflectance of a surface can be modified through dyes or paint. To analyze the effect of ρ on the work plane illuminance and glare levels, two cases were analyzed using the initial room as a benchmark. The first case represents the same office space but with highly opaque surfaces. Since $\rho = 0$ is impossible to achieve in a real case scenario, the reflectance of the walls, ceiling, and floor was set to be equal to 0.1. The second case is the highly reflective case where the reflectance of the same surfaces was set to 0.9 (since $\rho = 1$ is also impossible). Table 3.4 summarizes the information above and presents the physical parameters that were analyzed for this study. The choices made for the different levels of window to wall ratio and room dimensions aimed to reflect possible real-life scenarios: WWR 40% and 80% approximately represent the range of values typically found in office spaces (Susorova et al., 2013) while the room dimensions represent half and double the current room size. However, for the reflectance, extreme cases were considered to obtain illuminance and glare results that will help reach a clear conclusion. These values of opaque surface reflectance are never applied in real life office spaces.

Physical Parameter	Initial Value	Test Values	
Window to Wall Ratio	56%	40%	80%
Room Dimensions	31.6 m^3	15.8 m^3	63.25 m^3
Reflectance of the opaque surfaces	0.3 / 0.8 / 0.6	0.1 / 0.1 / 0.1	0.9 / 0.9 / 0.9

Table 3.4: *Physical parameter variation summary.*

4. Chapter 4: Results

The results chapter will be divided into four sections. The first section will discuss the daylighting trends concluded from the experimental setup in the test location regarding the evolution of the transmittance based on the incidence angle and the blind tilt angle. The following section will validate the visual transmittance models that were developed and will compare them to the previous models that were obtained from the literature. The next section will present the output of the visual comfort indices when the control strategy is applied. The final section will present the results of the physical parameter variations.

4.1- Daylighting Trends

4.1.1- Clear Sky

The experimental data for the indoor illuminance shows that the two main variables that affect its behavior are the blind tilt angle and the incidence angle of the sun. The evolution of each with respect to the other determined the visual comfort of the indoor environment at every time step. Figure 4.1 and Figure 4.2 were obtained in order to analyze the trends and conclude on the real-life behavior of the transmittance of the window.

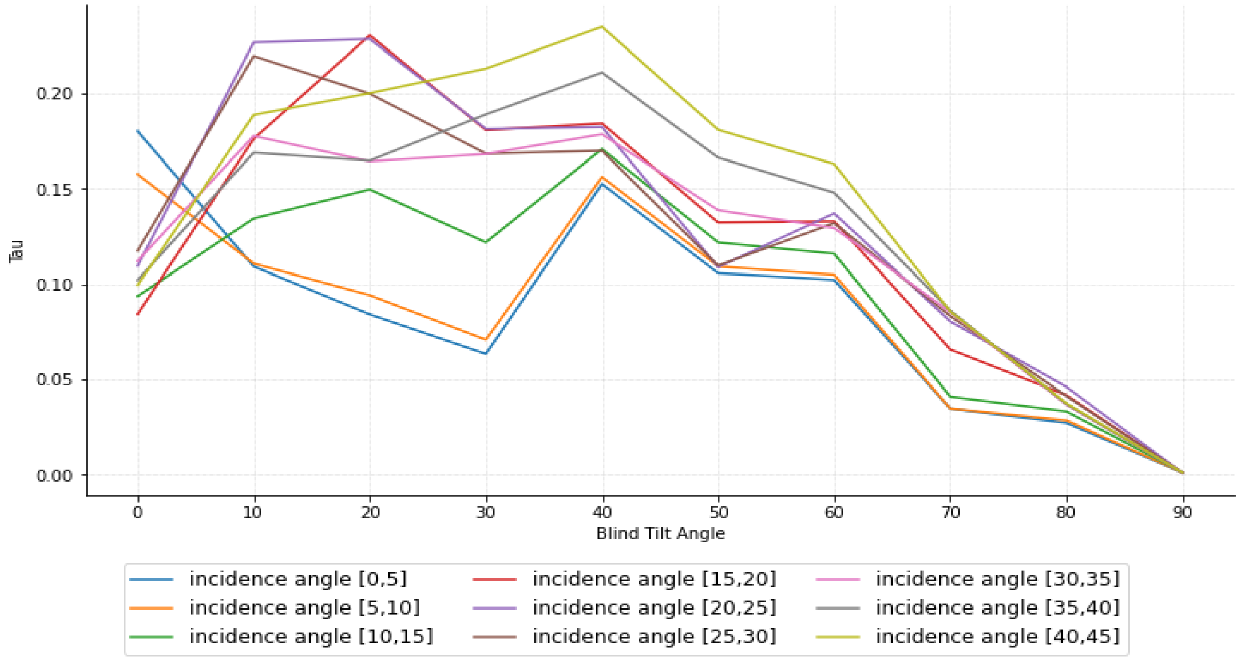

Figure 4.1: *Evolution of the transmittance with respect to the blind tilt angle for different intervals of the incidence angle under clear conditions.*

Figure 4.1 shows the evolution of the transmittance according to the blind tilt angle for different intervals of incidence angle, while the second presents the evolution of tau according to the incidence angle of the sun for different blind tilt angles. The first graph shows that the transmittance eventually converges as the blind tilt angle increases. And overall, a smaller blind tilt angles leads to an expected larger transmittance compared to a larger blind tilt angle because the latter leads to more reflection compared to a smaller β. Furthermore, the highest values of θ are the ones with the highest transmittance. This is due to the general rule that more light enters the indoor space during the middle of the day. However, the second graph does not show a common maximum for all the curves, with the maximums reached at different points and with no type of convergence.

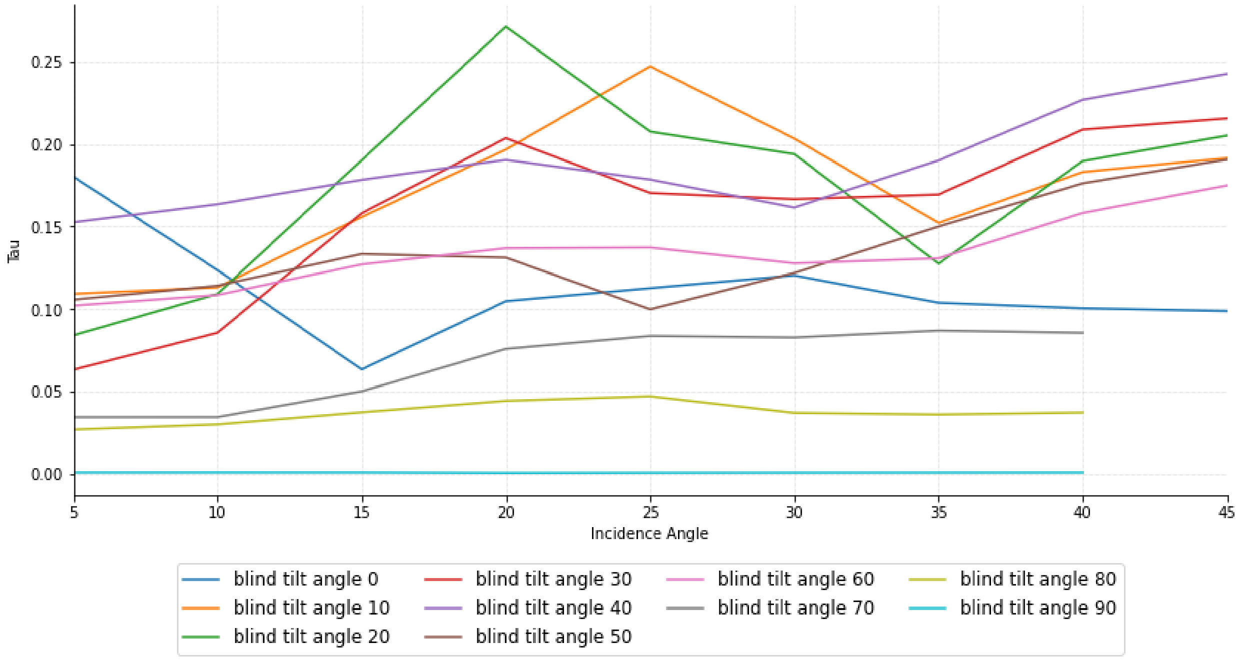

<u>Figure 4.2:</u> *Evolution of the transmittance with respect to the incidence angle for different blind tilt angles under clear conditions.*

Based on Figure 4.2, a general trend was observed for all blind tilt angles: The transmittance starts at its lowest when the incidence angle of the sun is the smallest. τ increases until it reaches a peak at the medium low range of θ (between 20 and 25 degrees). The transmittance then decreases gradually in the medium high range of the incidence angle (between 25 and 35 degrees), followed by an increase in τ for the largest incidence angles (between 35 and 45 degrees).

4.1.2- Cloudy Sky

Under cloudy conditions, the trend in transmittance is different compared to clear sky conditions. The incidence angle of the sun has a lower significance on the indoor illuminance levels because the vast majority of the incident daylight on the windows is diffuse, with only a small negligeable portion that can be considered direct. Figure 4.3 shows the evolution of the transmittance with respect to the blind tilt angle for different ranges of the incidence angle.

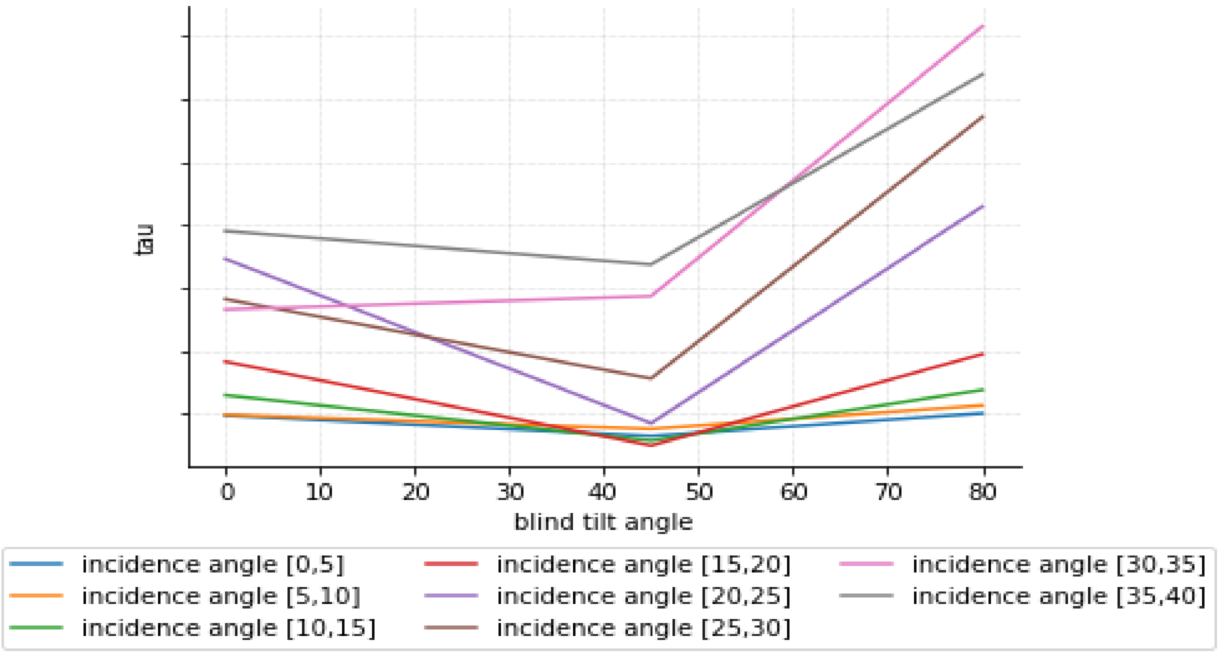

<u>Figure 4.3:</u> *Evolution of the transmittance with respect to the blind tilt angle for different intervals of the incidence angle under cloudy conditions.*

In this case, we can see a similarity in behavior for all the ranges of θ: It slowly decreases for the blind tilt angle in the range of 0 to 45 degrees, and then start to gradually increase for β between 45 degrees and 90 degrees. However, this increase is more noticeable for larger incidence angle intervals. These intervals also have the highest transmittance levels which suggests that, similar to clear days, the highest illuminance is expected during solar noon, when the light reaches the window at an angle between 30 to 40 degrees.

The decrease in transmittance as the blind tilt angle increases from 0 to 45 degrees can be attributed to an increase in the surface area of the blinds that block the transmitted daylight: As the blinds go from fully open (0 degrees) to partially open (45 degrees), the surface area of the blinds that is facing the sun increases, leading to more light being obstructed and reflected. The graph above shows that this decrease is more noticeable for small to medium incidence angles because the light is more perpendicular to the blind surface, thus increasing the amount of light that is reflected.

Furthermore, that are two explanations to why the transmittance then increases for blind tilt angles in the range of 45 to 90 degrees. First, these blind tilt angles allow the incoming daylight to pass through at steeper angles, making it easier to catch light coming in at sharper angles compared to the horizontal. In addition, the increase in τ can also be explained by the reflection of the blind slats at these specific tilt angles, which causes the incident daylight to reflect off of multiple slats before being transmitted to the space (instead of being reflected to the outside).

4.2- Transmittance Model Validation

4.2.1- Clear Conditions Transmittance Model Validation

The models found in the previous literature do not properly estimate the work plane illuminance under clear sky conditions. This is mainly due to the complexity of such a sky where direct / beam daylight represents the vast majority of the incident daylight on the AFS, with a small amount of light being reflected. That is why the impact of the incidence angle θ is important on a sunny day. The literature derived equations do account for θ, but the obtained work plane illuminance from these models does not match the experimental results. This is because it varies for different intervals of the blind tilt angle: Lower angles (0-45 degrees) result in a normal distribution of transmittance. However, larger angles (45-90 degrees) create a bimodal distribution, peaking twice within a day. The correction factor based on the incidence angle remains consistent.

In addition, in terms of the factor based on θ, the model presented in the literature uses a fourth-degree polynomial approximation which appears to be an overfit when compared to the experimental results. By testing different approaches, the optimal approximation was found to be a third-degree polynomial. A fourth-degree polynomial increased the RMSE when the model was compared with another data set for validation, while a second-degree polynomial does not capture the impact of the incidence angle on the illuminance properly.

Figure 4.4 and Figure 4.5 show a three-way comparison between the illuminance calculated using the developed model $\tau_{model,clear}$, the illuminance calculated using the product of the literature model and Snell's law $\tau_{lit,clear}$, and the experimental results. Two cases are shown: a small blind tilt angle case, represented by 0 degrees, and a large blind tilt angle case, represented by the 50 degrees. Figure 4.4 shows the model and experimental results illuminance, while Figure 4.5 is used as a benchmark case to evaluate the accuracy of the developed model compared to previous models available in the literature. The objective is to highlight the improvement that the new model provides compared to previous models under clear conditions for this specific type of advanced fenestration system.

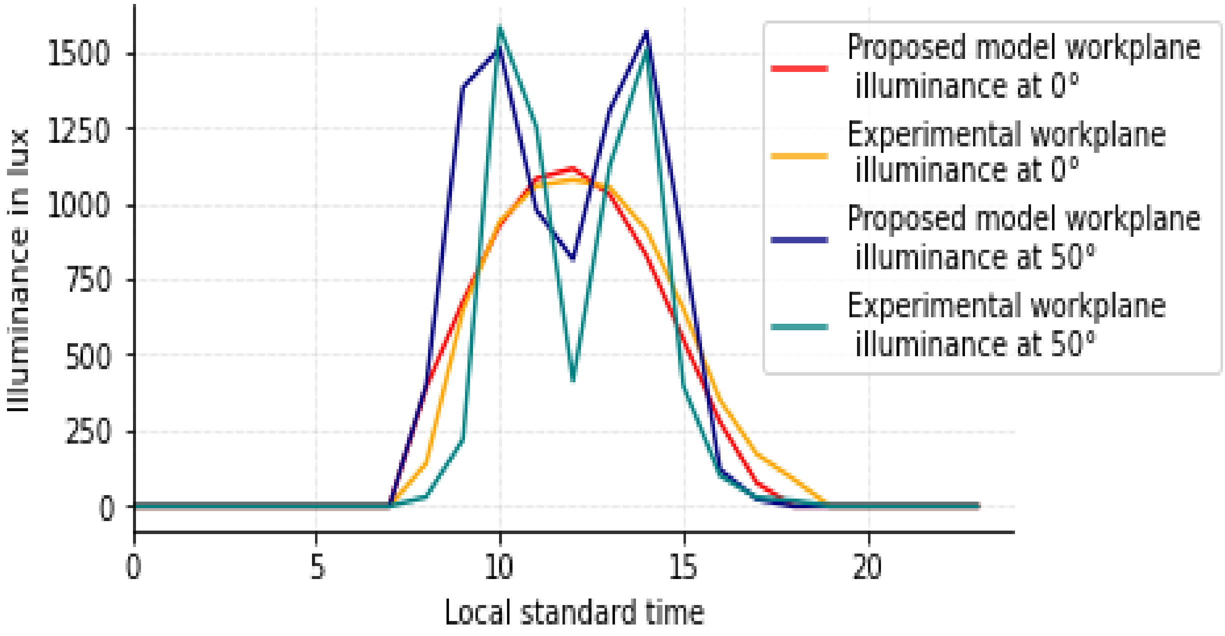

Figure 4.4: *Experimental and theoretical work plane illuminance from developed model as a function of time for blind tilt angles of 0 degrees and 50 degrees under clear conditions.*

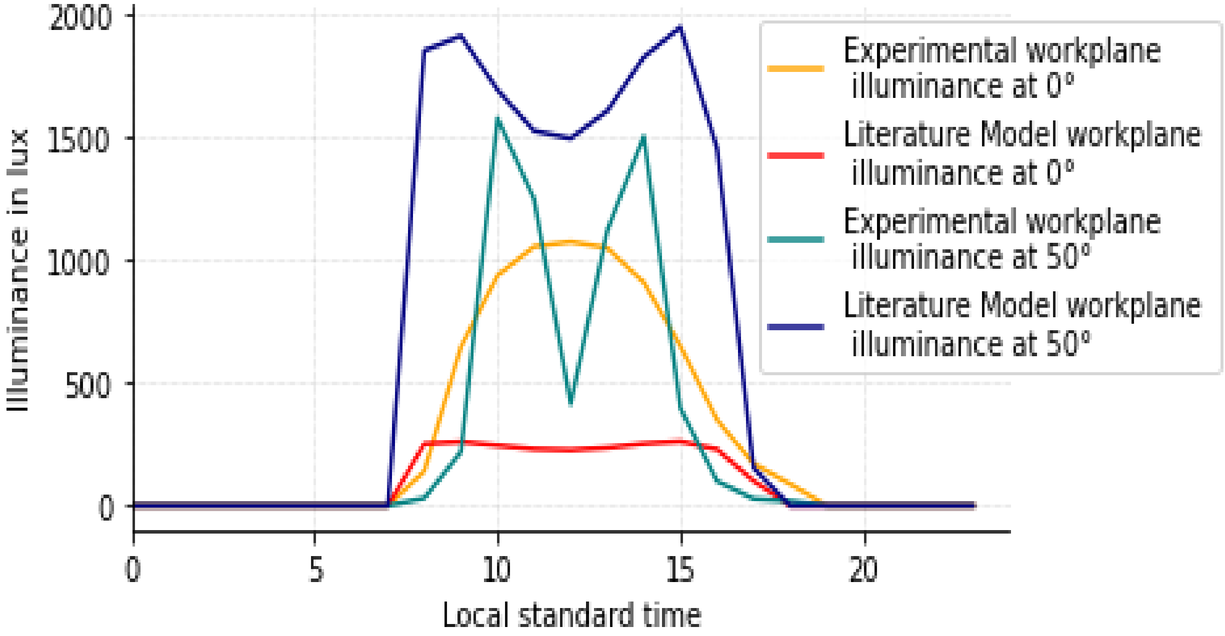

Figure 4.5: *Experimental and theoretical work plane illuminance from previous literature models for blind tilt angles of 0 and 50 degrees under clear conditions.*

For small blind tilt angles, the developed model follows the normal distribution of the work plane illuminance compared to the previous model which assumes a fairly constant illuminance throughout the day. In addition, the literature model assumes a very low level of illuminance compared to the actual values obtained from the experiment. The proposed model takes that into account and offers more accurate results. For larger blind tilt angles, both models show a certain level of bimodal distribution. However, the previous model does not account for the steep decline caused during high incidence levels (solar noon). The proposed model considers this decline as it is an important factor in mimicking the visual properties of the system. The main difference between both models is that one differentiates between different intervals of tilt angle, while the other assumes the same behavior for all tilt angles, which is shown to be an inaccurate assumption from the experimental data obtained in the test lab. Differentiating between the ranges of β allows for increased accuracy, as shown in the RMSE values calculated. Table 4.1 shows the RMSE between the proposed model and the experimental data, as well as the RMSE between the previous model and the experimental data in order to highlight the improvement that the new model provides.

Beta	RMSE model work plane illuminance and experimental work plane illuminance (lux)	RMSE previous work plane illuminance model and experimental work plane illuminance (lux)	Percent decrease in RMSE
0 degrees	66.29 lux	372 lux	82%
10 degrees	164.50 lux	417 lux	60%
20 degrees	207.73 lux	382 lux	46%
30 degrees	288.94 lux	374 lux	23%
40 degrees	321.29 lux	394 lux	19%
50 degrees	287.05 lux	709 lux	60%
60 degrees	306.74 lux	1002 lux	70%
70 degrees	453.84 lux	1312 lux	66%
80 degrees	301.13 lux	1123 lux	73%

Table 4.1: *RMSE values between the experimental and theoretical results of the work plane illuminance (in lux) for different blind tilt angles under clear sky conditions.*

4.2.2- Cloudy Conditions Transmittance Model Validation

The transmittance model $\tau_{model,cloudy}$ was used to calculate the theoretical work plane illuminance over a 24-hour period for a pre-determined blind tilt angle. The illuminance was then evaluated against the experimental results in order to determine the accuracy of the model mimicking the real-life visual properties of the advanced fenestration system considered. In the case of the cloudy transmittance model, $\tau_{model,cloudy}$ was used. The data collected from the lab under cloudy conditions were for blind tilt angles of 0 degrees, 45 degrees, and 80 degrees between the 28th and 30th of April 2024. The obtained illuminance was then compared to that calculated using the transmittance model based on the literature equations $\tau_{lit,cloudy}$ applied on the same 24-hour periods. A three-way comparison between the two models and the experimental results is shown in Figure 4.6 and Figure 4.7 to assess the improvement that $\tau_{model,cloudy}$ brings. Two cases are shown: one for a small blind tilt angle, represented by $\beta = 0$, and one for a large blind tilt angle, represented by $\beta = 80$. Figure 4.6 shows the model and experimental results illuminance, while Figure 4.7 is used as a benchmark case to evaluate the accuracy of the developed model compared to previous models available in the literature.

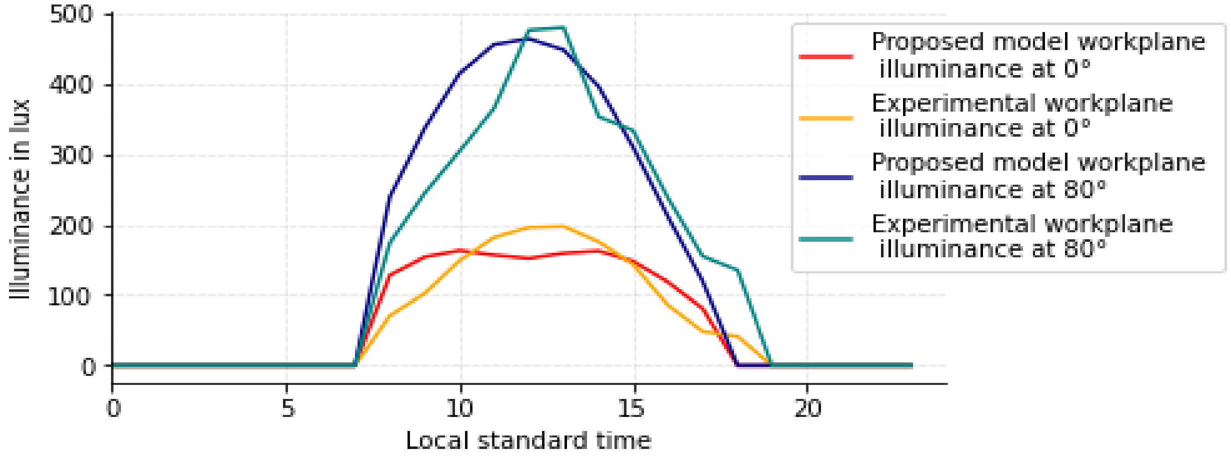

Figure 4.6: *Experimental and theoretical work plane illuminance from developed model as a function of time for blind tilt angles of 0 degrees and 80 degrees under cloudy conditions.*

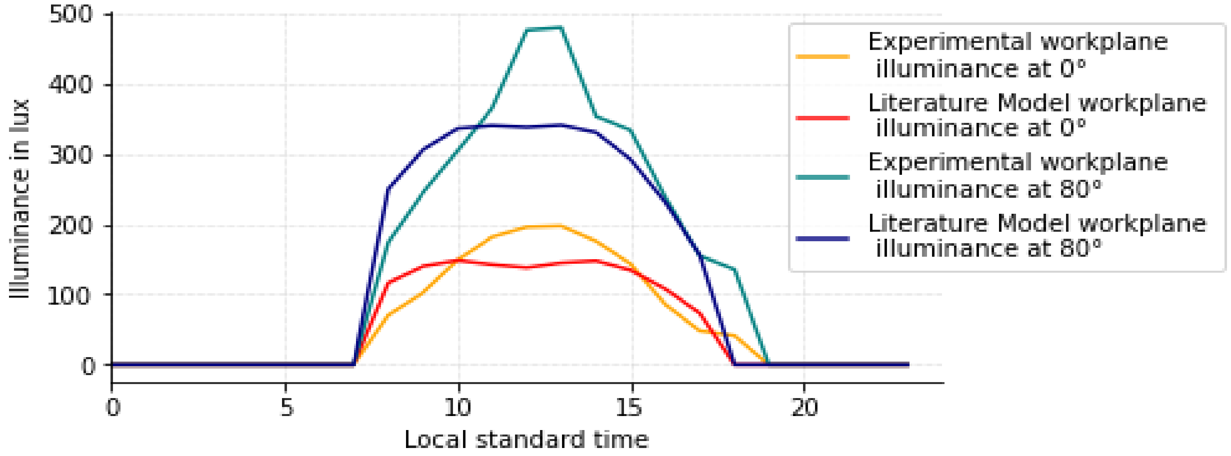

Figure 4.7: *Experimental and theoretical work plane illuminance from previous literature models for blind tilt angles of 0 and 80 degrees under cloudy conditions.*

Figure 4.6 and Figure 4.7 show that $\tau_{model,cloudy}$ provides a robust estimation of the work plane illuminance under cloudy conditions. For larger blind tilt angles, the literature model underestimate the illuminance during midday where θ is at its highest, which is not the case for the data driven model. This is because of the first-degree polynomial that accounts for the small, yet not negligeable, impact of the beam daylight on indoor illuminance under cloudy sky conditions. However, for small blind tilt angles, the impact of the incidence angle is less pronounced, shown by similar illuminance curves for both models. Still, $\tau_{model,cloudy}$ provides more accurate results for all possible blind tilt angles under overcast conditions compared to previous models.

To compare the accuracy of the models based on the experimental values, the root mean square error was also used. Table 4.2 shows the RMSE between the proposed model and the experimental data, as well as the RMSE between the previous model and the experimental data in order to highlight the improvement that the new model provides.

Beta	RMSE model work plane illuminance and experimental work plane illuminance (lux)	RMSE previous work plane illuminance model and experimental work plane illuminance (lux)	Percent decrease in RMSE
0 degrees	20.23 lux	24.88 lux	18.7%
45 degrees	70.0 lux	83.50 lux	16.2%
80 degrees	46.9 lux	54.06 lux	13.3%

Table 4.2: *RMSE values between the experimental and theoretical results of the work plane illuminance (in lux) for different blind tilt angles under cloudy sky conditions.*

The obtained values are low using both models, even though $\tau_{model,cloudy}$ brings a certain improvement compared to previous models. This is mainly due to the first-degree polynomial based on the incidence angle θ which is neglected in $\tau_{lit,cloudy}$. In additions, as opposed to the clear day model, the transmittance does not behave differently based on different intervals of the blind tilt angle, which means that the beam / direct daylight is the main cause of the bimodal distribution that was seen for large blind tilt angles (45 to 90 degrees).

4.3- Control Strategy Results

Based on the validated transmittance models above, the control strategy was simulated within the test cell to analyze its impact in term of illuminance levels and glare probability. As stated, the objective is to have a work plane illuminance above 300 lux and glare probability below 0.35, which are the standard thresholds for an office environment. The mentioned variables, as well as the sun position, are calculated for a 15-minute interval during the occupancy period.

4.3.1- Clear Sky Conditions

The control strategy was simulated for a clear day in the heating season. Figure 4.8 and Figure 4.9 show the obtained results in terms of work plane illuminance E_p and simplified daylight glare probability $DGPs$, calculated using the equations presented in section 3.2. As a benchmark for comparison, the curves for a blind tilt angle of 0 degrees are also shown to evaluate the improvements that this control strategy can bring to the visual comfort of the indoor environment. The threshold value for both cases are also presented in both cases. The control strategy output shows promising results on a sunny day. In terms of work plane illuminance, E_p remains above the 300-lux threshold except between 11:00 AM and 12:00 PM, where it is exactly equal to 300 lux to keep the $DGPs$ in an imperceptible range. It is maximum during lunch hours because there are no constraints in terms of glare levels, which helps increase the passive solar heating gains and reduce energy consumption.

c

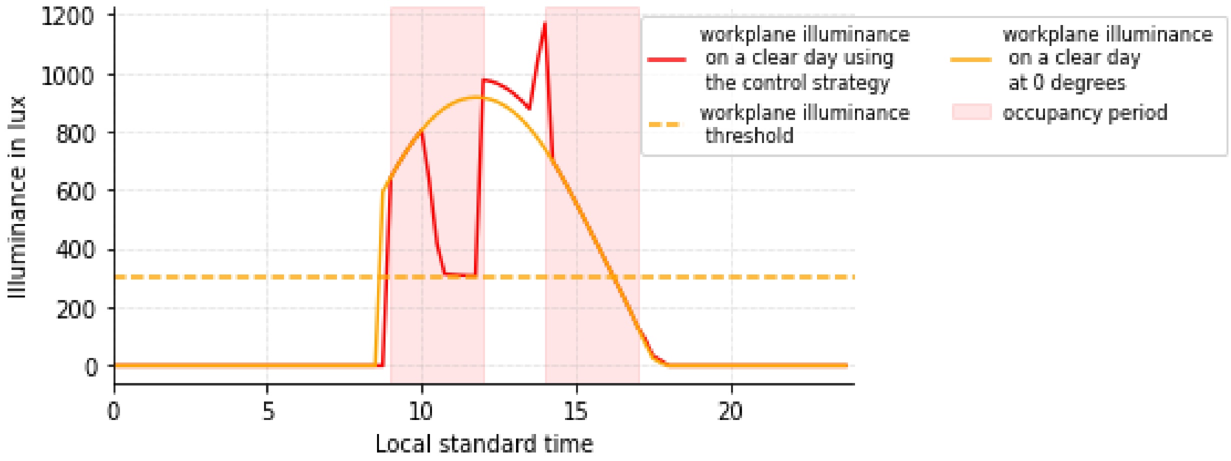

Figure 4.8: *work plane illuminance on a clear day in the office space with the control strategy applied.*

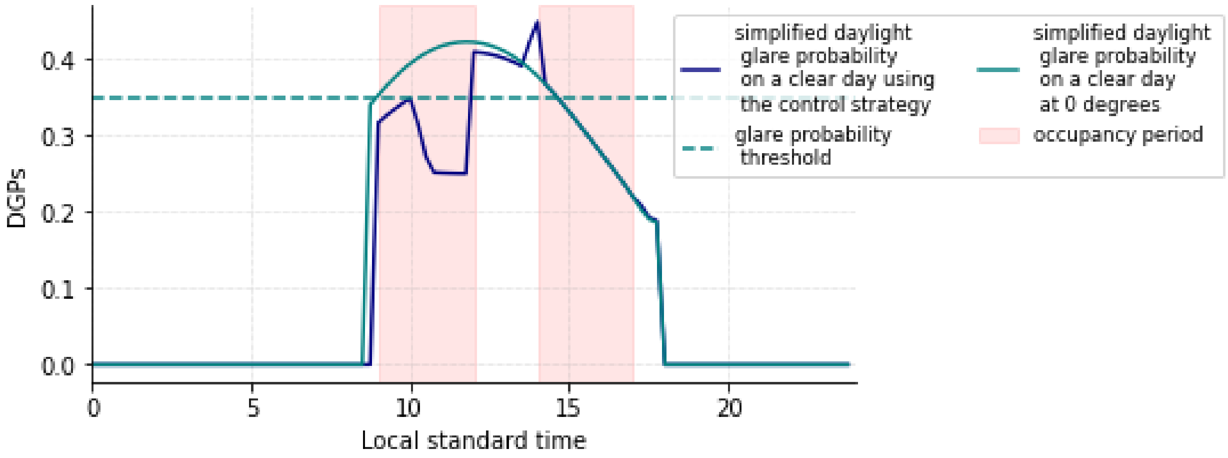

Figure 4.9: *simplified daylight glare probability on a clear day in the office space with the control strategy applied.*

After 2:00 PM, the profile angle remains above 45 degrees until 5:00 PM, which sets the blinds at 0 degrees, allowing for an optimized view of the outside. As expected, since the profile angle is above the set threshold, glare is below 0.35 throughout this whole period. In terms of glare levels, the probability that glare becomes noticeable only occurs between 2:00 PM and 3:00 PM (glare is not considered an issue when the office is unoccupied between 12:00 PM and 2:00 PM), which allows for a visually comfortable work environment throughout the day. Compared to the reference case of 0 degrees, the latter does indeed provide higher illuminance in the early hours of the workday. However, this increased E_p is accompanied by high levels of glare, even surpassing 0.45, which makes it noticeable and disturbing. Therefore, the implementation of the control strategy ensures that the illuminance and glare levels are within the comfort ranges, while also increasing passive solar gains and allowing maximum view to the outside whenever possible. Overall, using the control strategy, the work plane illuminance is above the desired threshold for 86% of the occupancy period and the glare levels are below the desired threshold for 93% of the same period. However, setting the blind tilt angle to 0 degrees for the whole day, the illuminance is optimal for 83% of the occupancy period, while glare is imperceptible for only 43% of the same period. Figure 4.10 shows the evolution of the optimal blind tilt angle throughout the day.

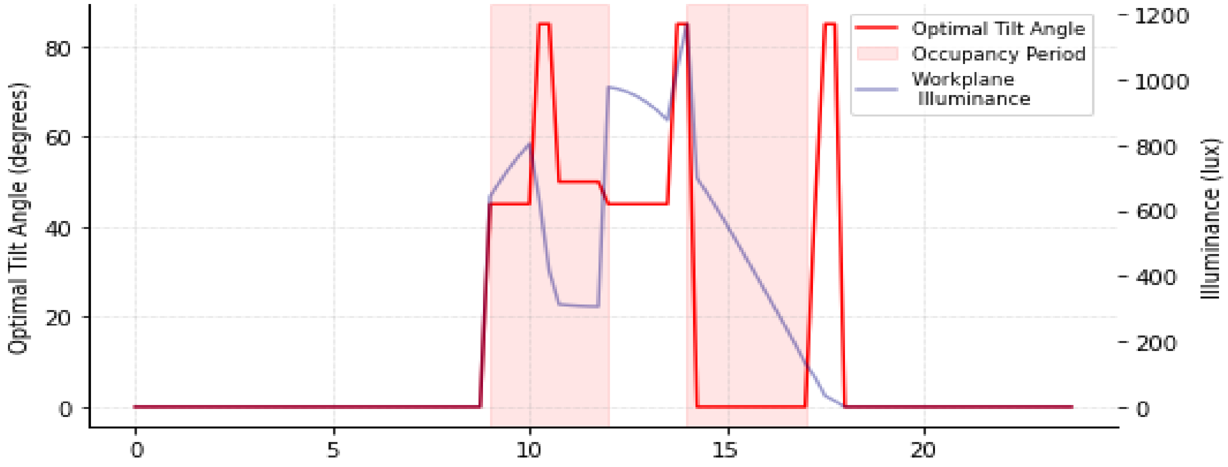

Figure 4.10: *Optimal blind tilt angle on a clear day in the office space with the control strategy applied.*

4.3.2- Cloudy Sky Conditions

The same simulation approach was considered for a cloudy day in the heating season. The cloudy case scenario is less complicated since glare is not an issue for most of the day. However, during the middle of the day, it can be a bit impactful in increasing the $DGPs$. Figure 4.11 and Figure 4.12

show the obtained results in terms of work plane illuminance E_p and simplified daylight glare probability $DGPs$, calculated using the equations presented in section 3.2. Similar to the clear day simulation, a benchmark scenario where the blind tilt angle is set at a constant angle of 0 degrees is shown as a way to highlight the improvement that the control strategy offers in terms of visual comfort. The threshold value for both cases are also presented in both cases.

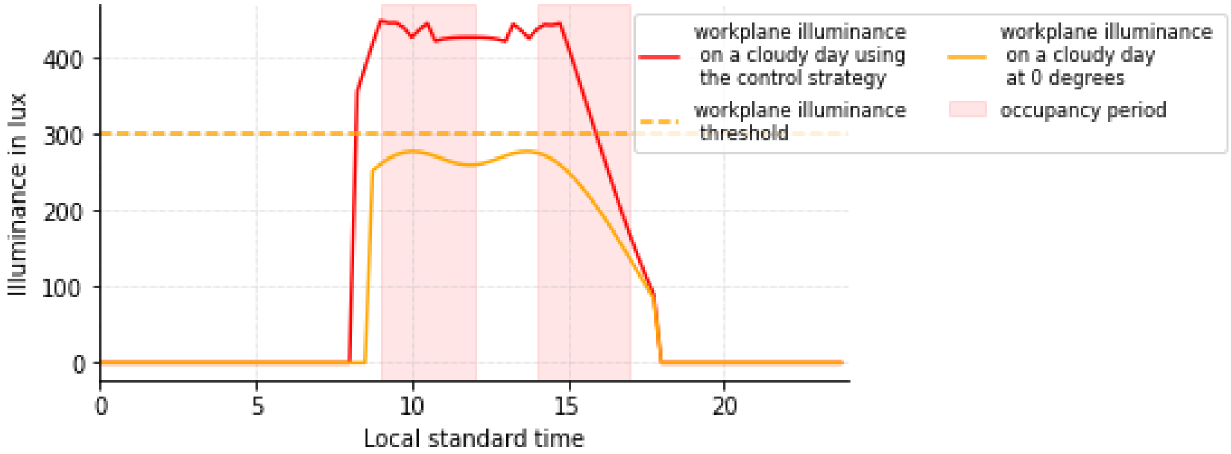

Figure 4.11: *work plane illuminance on a cloudy day in the office space with the control strategy applied.*

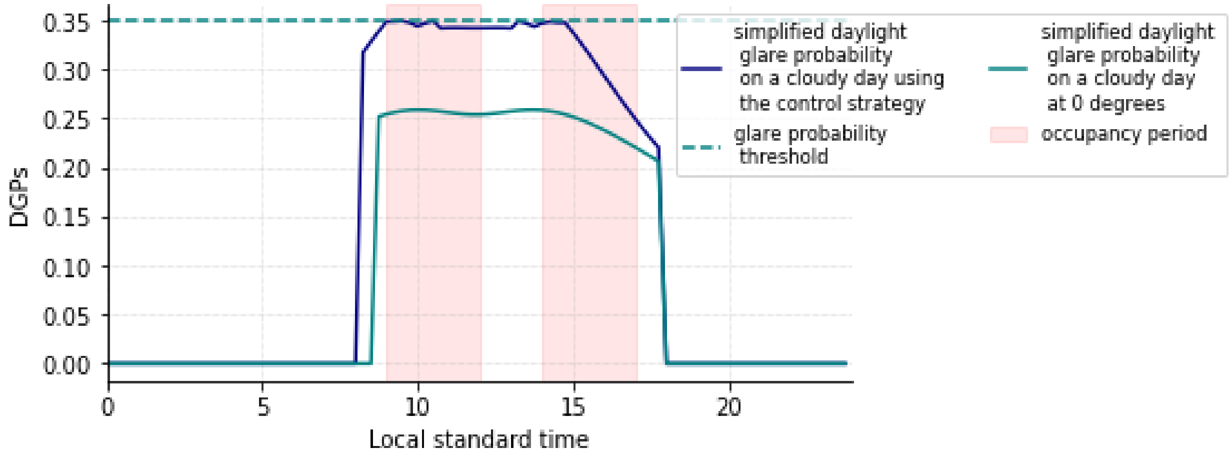

Figure 4.12: *simplified daylight glare probability on a cloudy day in the office space with the control strategy applied.*

The control strategy applied during a cloudy day provides an improvement compared to the base scenario. Using the control approach, the work plane illuminance is over the comfort threshold for 72% of the occupancy period, only dropping below 300 lux by 4:00 PM. In terms of simplified daylight glare probability, it remains below 0.35 for a 100% of the occupancy period. This is an improvement compared to the 0 degrees base scenario where even though glare is imperceptible for a 100% of the occupancy schedule, the work plane illuminance never reaches 300 lux. By keeping the glare levels very close to the threshold, the control strategy is able to ensure comfort levels of illuminance, which the base case is not able to achieve. Figure 4.13 shows the evolution of the optimal blind tilt angle throughout the day.

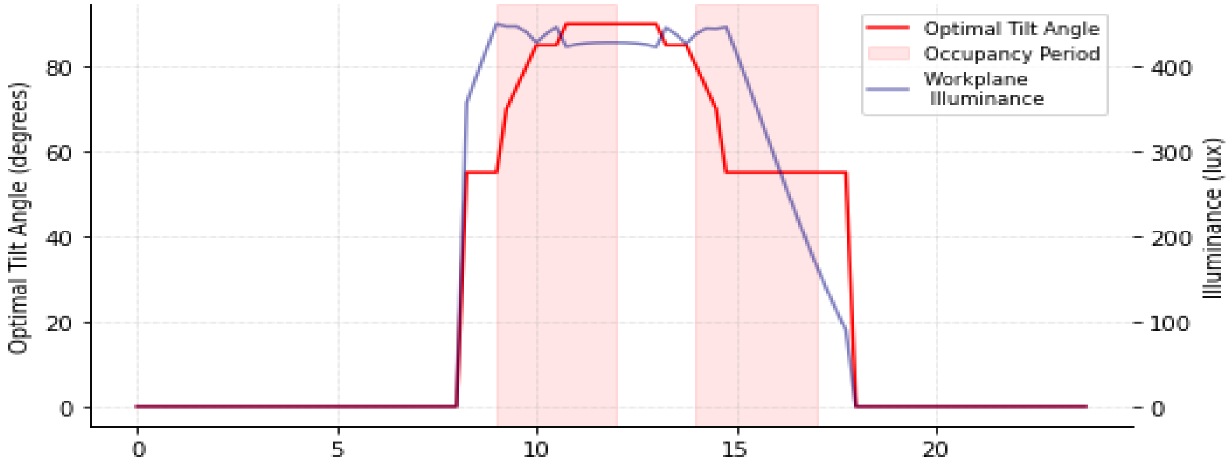

Figure 4.13: *Optimal blind tilt angle on a cloudy day in the office space with the control strategy applied.*

4.4- Parametric Effect on Visual Comfort

With the control strategy applied to the case study office space, different physical parameters were studied and simulated to determine their impact on the indoor visual comfort. These physical parameters are mainly related to the WWR, the room geometry, and the reflectance of the opaque surfaces. The results from the simulations are presented in this section.

4.4.1- Window to Wall Ratio

The office space has a window to wall ratio of 56%. WWR plays an essential role in determining the amount of natural daylight that can enter the space at any given time. The impact of the window size is indirectly related to illuminance calculations because it is used to calculate the view factor and the configuration factor. Two different WWR were tested to analyze this phenomenon: a smaller window to wall ratio equal to 40%, and a larger one equal to 80%. Figure 4.14 and Figure 4.15 show the results obtained by varying this parameter on the work plane illuminance and the simplified daylight glare probability.

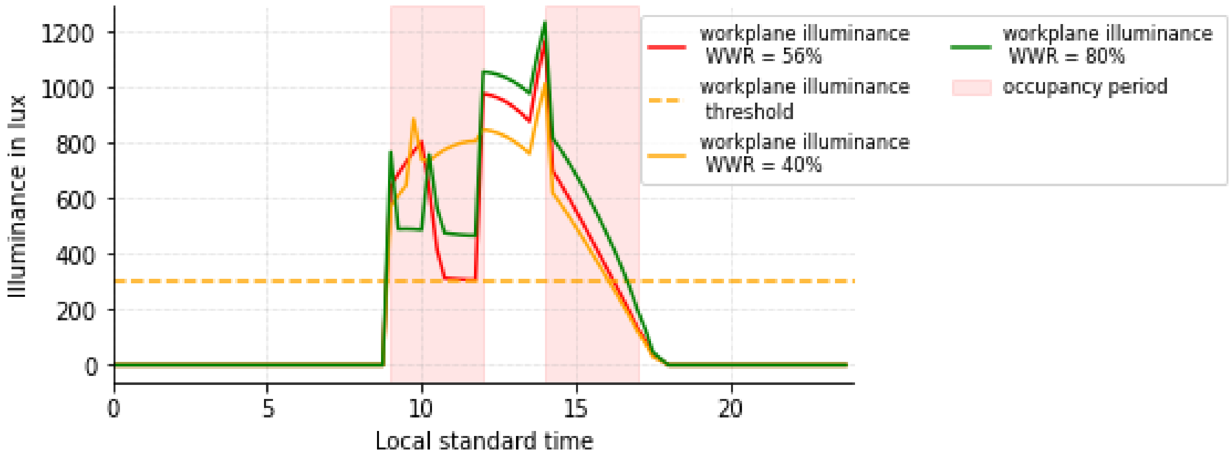

Figure 4.14: *work plane illuminance for different WWR on a clear day with the applied control strategy.*

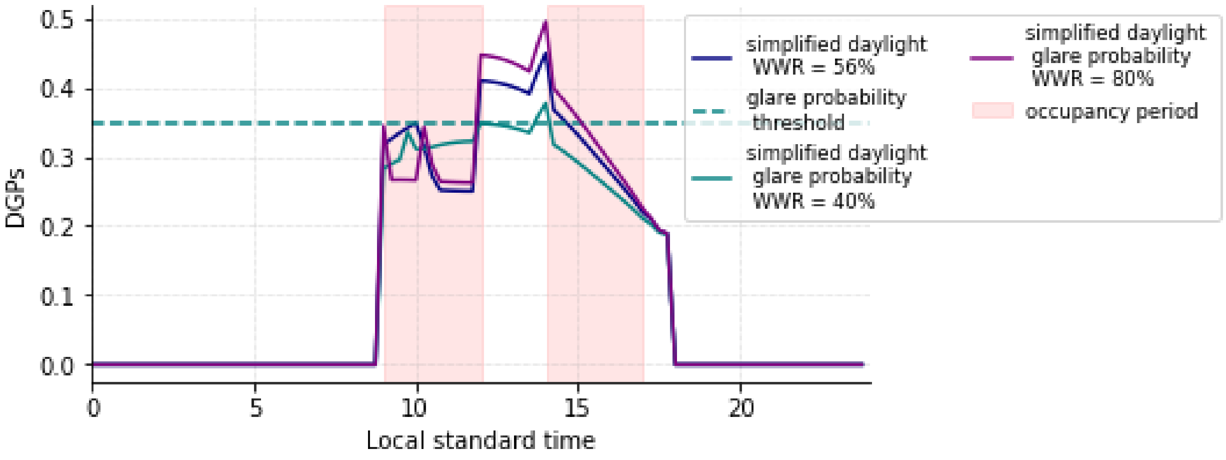

Figure 4.15: *simplified daylight glare probability for different WWR on a clear day with the applied control strategy*

The results show that a smaller WWR has a positive impact on visual comfort because it keeps glare levels at imperceptible levels 100% of the occupancy period while allowing acceptable illuminance for most of the day until 4:00 PM (around 20% of the occupancy period requires artificial lighting). At the same time, a WWR = 80% ensure that the work plane illuminance is above 300 lux during the whole occupancy period. However, glare does become an issue in this case, especially between 2:00 PM and 3:00 PM. Overall, the glare is below 0.35 for 85% of the occupancy. In addition, a larger WWR allows for increased passive solar gains during unoccupancy.

4.4.2- Room Dimensions

The room size also plays an important role in determining the indoor illuminance level. The radiosity analysis applied to calculate E_p uses the dimensions and geometry of the space as an input in order to obtain the final luminous exitance M of each surface. M then determines the work plane illuminance (and the simplified daylight glare probability) based on the configuration factor of the surface with respect to the center of the room. To understand the effect room dimensions, have on visual comfort, the control strategy was applied for the same clear day for an office space half the size and double the size of the initial room, with the window to wall ratio remaining constant at 56%. Figure 4.16 and Figure 4.17 show the results obtained from the simulation in terms of E_p and $DGPs$ respectively. As expected, the size of the room significantly reduces the illuminance levels within a space when considering a constant WWR. For a double size room, the maximum E_p reaches 1000 lux. It remains above the required threshold until around 3:00 PM. That is when a dimming artificial light approach can come in handy. At the same time, reducing the space by half allows for the complete elimination of artificial lighting need because it provides a work plane illuminance above 300 lux throughout the occupancy period. This decrease in illuminance is caused mainly by two reasons that will be explored in section 5.4. Overall, a smaller room keeps E_p above 300 lux for 100% of the occupancy, compared to a larger room with an average of 72% of the occupancy. For $DGPs$, a smaller room has imperceptible glare for 80% of the time whereas a larger room is never impacted by glare.

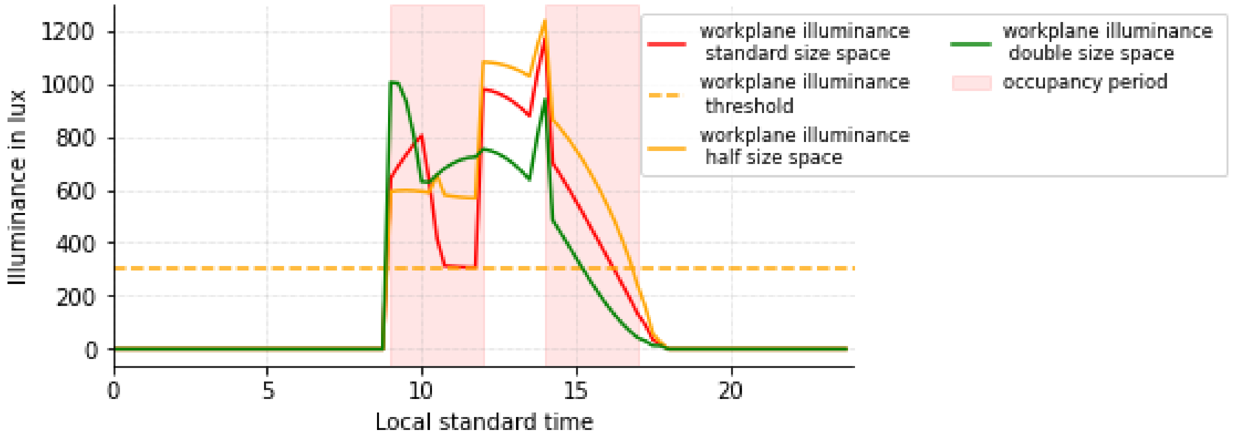

Figure 4.16: *work plane illuminance for different room dimensions on a clear day with the applied control strategy.*

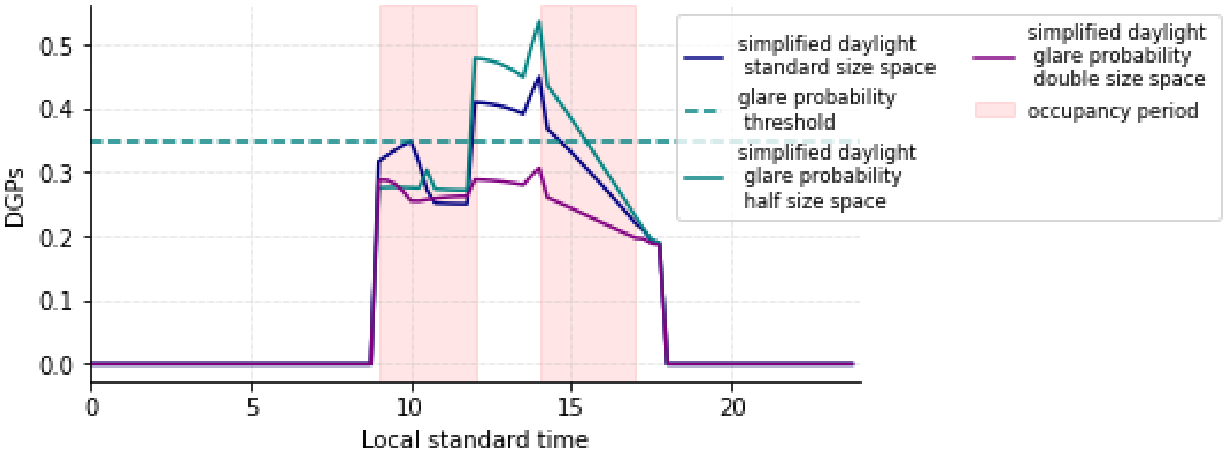

Figure 4.17: *simplified daylight glare probability for different room dimensions on a clear day with the applied control strategy.*

4.4.3- Reflectance of the Opaque Surfaces

Another important aspect that significantly influences the illuminance levels is the reflectance of the surface. The reflectance represents the portion of light that an object reflects from the total incident light on its surface. In real life, the reflectance of a surface can be modified through dyes or paint. To analyze the effect of ρ on the work plane illuminance and glare levels, two cases were analyzed using the initial room as a benchmark and the control strategy applied. The first case represents the same office space but with highly opaque surfaces where the reflectance of the walls, ceiling, and floor was set to be equal to 0.1. The second case is the highly reflective case where the reflectance of the same surfaces was set to 0.9. The results in terms of E_p and $DGPs$ are shown in Figure 4.18 and Figure 4.19. The results show that highly reflective surfaces have a positive impact on the work plane illuminance but lead to increase levels of glare, even reaching into the disturbing levels. These types of surfaces also increase the passive solar gains during occupancy since E_p can reach up to 2000 lux during unoccupancy. However, opaque surfaces seem to be optimal in this case: Even though artificial lighting is needed starting from around 3:30 PM, the $DGPs$ remains below 0.35 throughout the whole day. The trade-off becomes clear: if the objective is to increase work plane illuminance and solar passive gains, then reflective surfaces are preferred.

Nevertheless, if the objective is to ensure imperceptible glare, then opaque surface (through paint) should be considered. Overall, for reflective surfaces, E_p is over 300 lux for 100% of the occupancy period and $DGPs$ is in the imperceptible threshold for 70% of the same period. In the case of opaque surfaces, E_p is acceptable for 78% of the occupancy, with glare never being an issue.

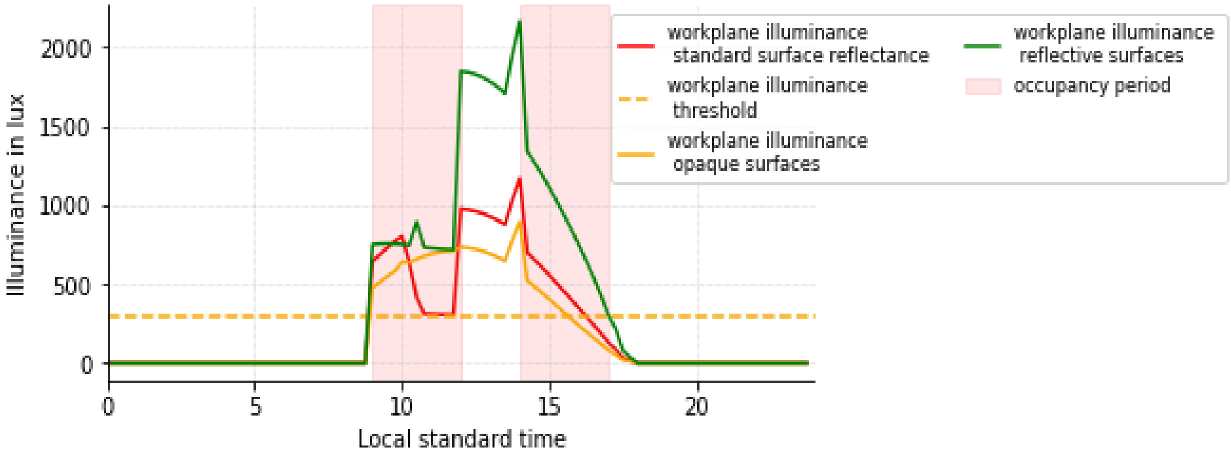

Figure 4.18: *work plane illuminance for different surface reflectance on a clear day with the applied control strategy*

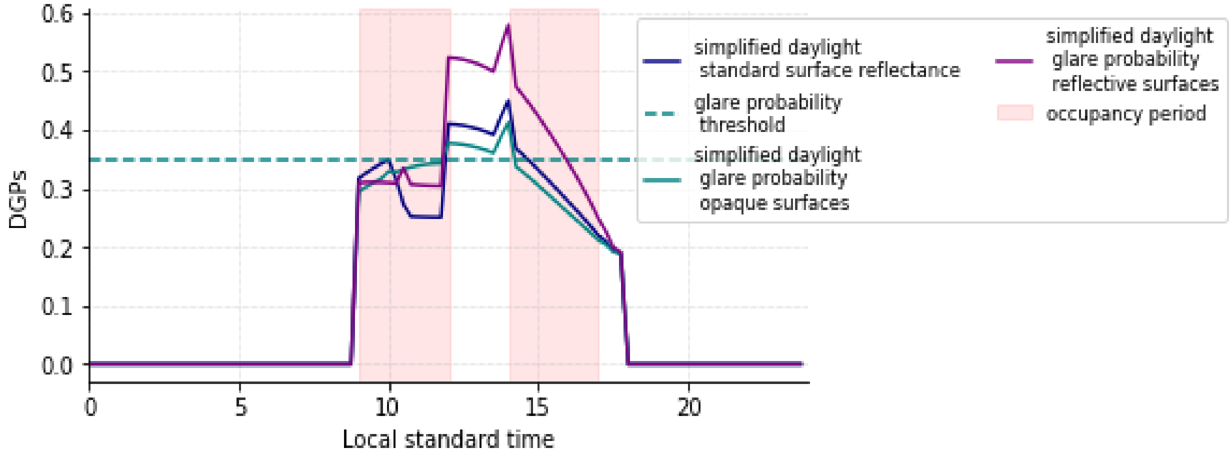

Figure 4.19: *simplified daylight glare probability for different surface reflectance on a clear day with the applied control strategy.*

5. Chapter 5: Discussion

5.1- Transmittance Trends under Clear Sky Conditions

The behavior of the transmittance under clear sky conditions can be explained by categorizing the blind tilt angles β based on their transmittance curves behaviors. For this reasoning, a small blind tilt angle is assumed to be between 10 and 20 degrees, a medium blind tilt angle is between 30 and 70 degrees, and a large blind tilt angle is 80 degrees or above. For this explanation, the completely horizontal and completely vertical cases are excluded as they represent individual specific cases. Each point of discussion represents a specific case from Figure 5.1.

- Small blind tilt angles (between 10 and 20 degrees):

Based on the figure below, the process of the evolution of the transmittance can be explained as follows. Note that the graphs shown are for the blind tilt angles 10 and 20 degrees.

(a) For small incidence angles, the light hits the center of the slat, which represents the lowest transmittance due to an increase in absorption from the thickness of the slat. As the incidence angle increases, the light hits thinner parts of the slat which decreases absorption, thus increasing transmittance.

(b) For medium low incidence angles, the light passes through the space between the two slats, maximizing the transmittance due to an absence of absorption and reflection. In this case, the light is not diffused, but rather specular.

(c) For medium high incidence angles, the light hits the bottom slat, which explains the decrease in the transmittance after reaching the maximum. As the incidence angle increases further, the light moves from the edge of the slat towards the center, increasing the absorption, thus decreasing the transmitted daylight, until reaching a regional minimum.

(d) Further into the medium high incidence angles, the light hits the bottom slat, which explains the decrease in the transmittance after reaching the maximum. As the incidence angle increases further, the light moves from the edge of the slat towards the center, increasing the absorption, thus decreasing the transmitted daylight, until reaching a regional minimum.

(e) For high incidence angles, As the light moves from the center of the slate towards the edges, the absorption effect decreases, thus increasing the transmittance of the light. The transmittance keeps increasing until the incidence angle reaches its maximum for the day (around 45 degrees), which coincides with midday.

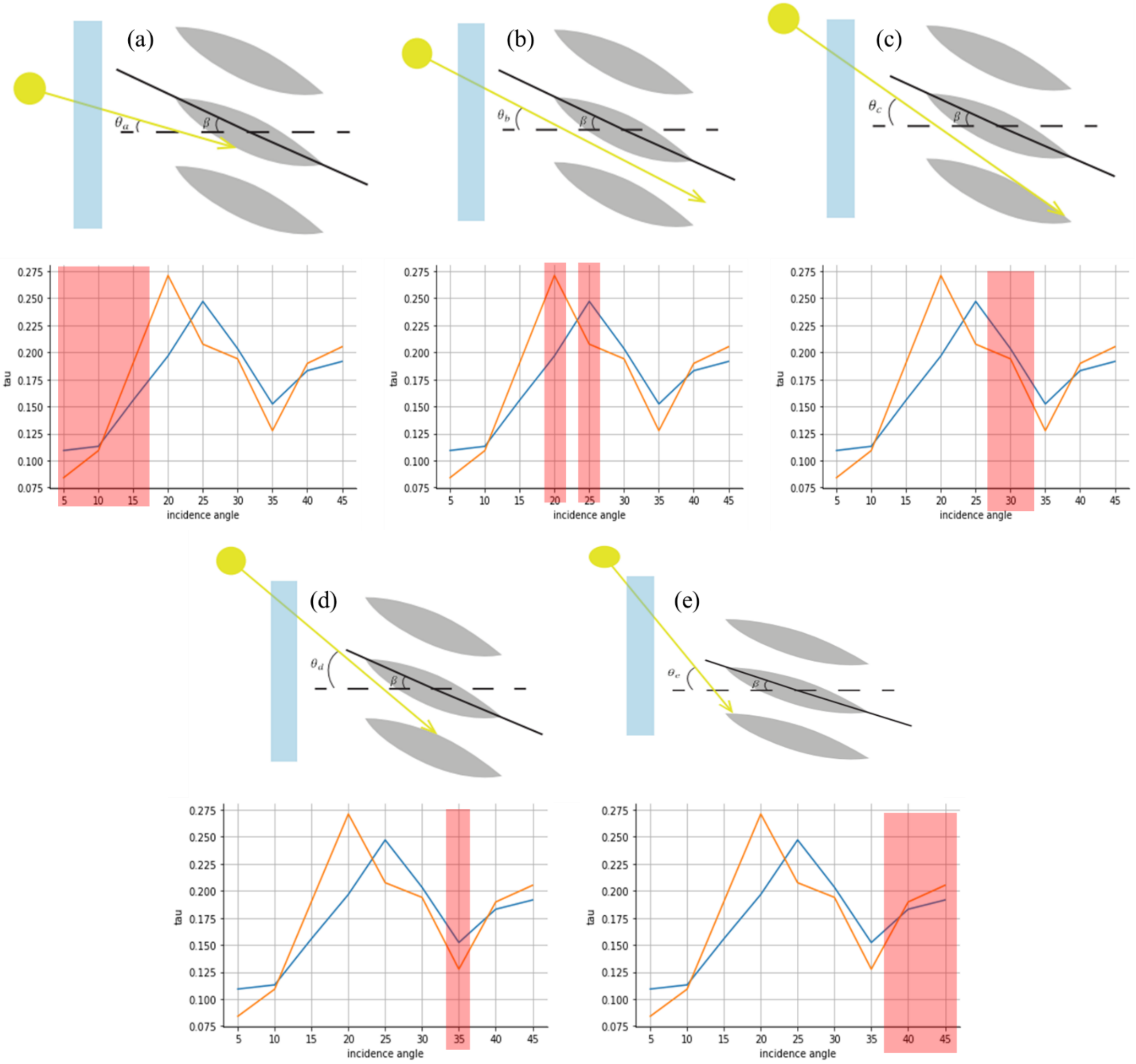

Figure 5.1: *Evolution of the transmittance with respect to θ for small blind tilt angles under clear conditions.*

- Large blind tilt angles (80 degrees and above):

Based on the Figure 5.2, the process of the evolution of the transmittance can be explained as follows. Note that the graph shown in Figure 5.2 is for the blind tilt angles of 80 degrees.

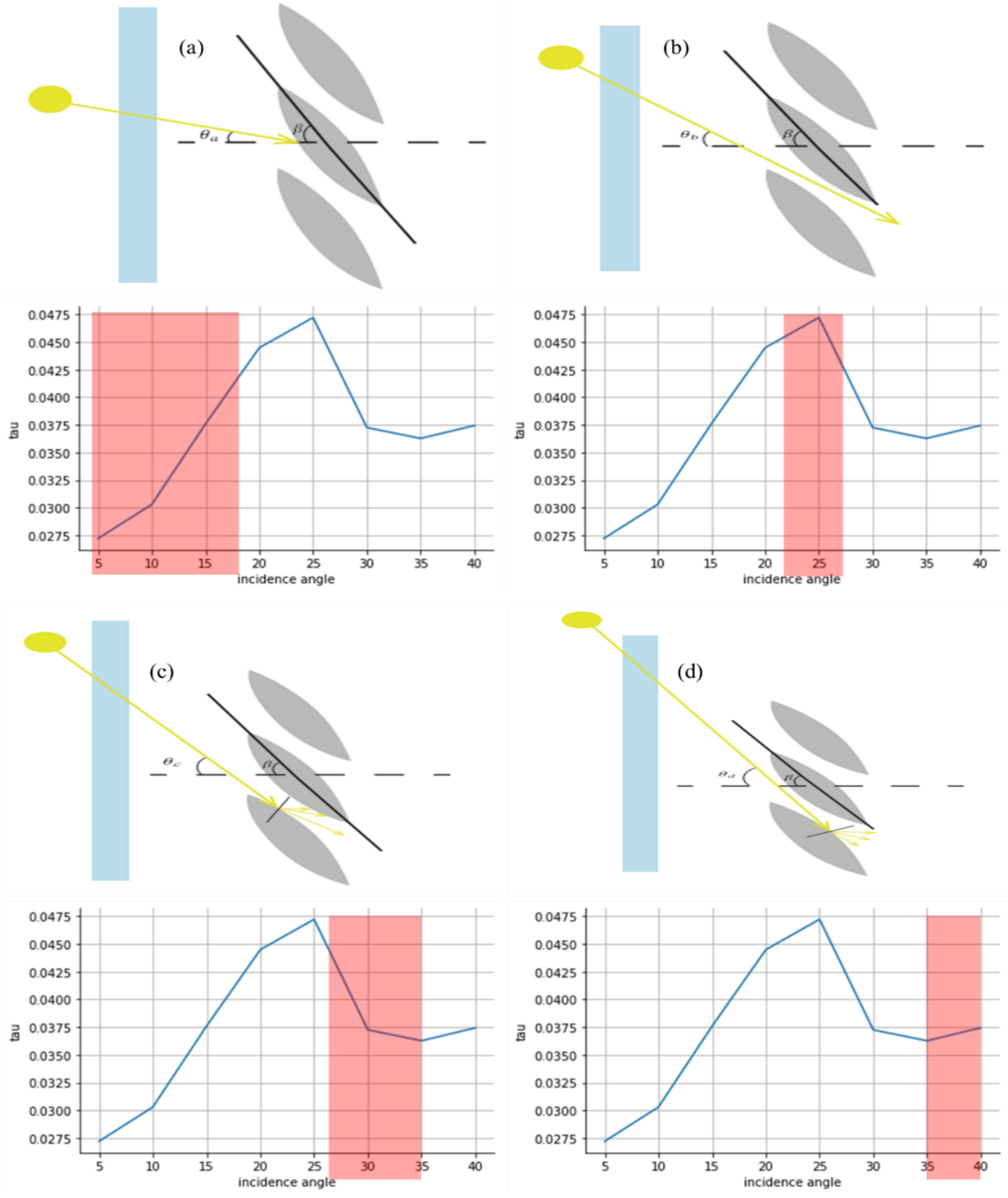

Figure 5.2: *Evolution of the transmittance with respect to* θ *for large blind tilt angles under clear conditions.*

(a) For small incidence angles (0 to 25 degrees), Light hits the center of the slat, which results in the lowest transmittance because of the increased absorption and because the reflected light is redirected outside of the space rather than towards the room. As theta increases in the small range, the light starts moving towards the edges of the slat, decreasing absorption and increasing light reflected into the room.

(b) For medium low incidence angles (25 to 35 degrees), the transmittance reaches its maximum as light passes in between the slats. This increase is due to a lack of absorption. However, in this case, the light being transmitted is specular and not diffuse.

(c) For medium high incidence angles (35 to 40 degrees), the light hits the bottom slat, decreasing the transmittance. This decrease is due to the absorption from the slat, but also reflection: in this position, the normal of the slat causes a significant portion of the reflected light to hit the upper slat instead of penetrating within the space. This is because the large blind tilt angles make them block reflected light coming from the other slats.

(d) For high incidence angles (40 to 45 degrees), as light moves towards the center of the slat (for high incidence angles), transmittance slightly increases. This is caused by the direction at which the reflected light travels: unlike in the previous case, the reflected light is no longer mostly blocked by the upper slate, meaning that the diffuse daylight is transmitted through the glazing into the office space. The transmittance could potentially further increase if it were not for the increased absorption caused by the center of the slat.

- <u>Medium blind tilt angles (30 to 70 degrees):</u>

the way light hits the blind follows the same pattern as for large blind tilt angles as shown by a similarity in the curve's shapes. However, they differ in one crucial aspect: the maximum transmittance. For large betas, the maximum is attained at medium low ranges of the incidence angle. But for medium range betas, the maximum is attained for high theta values. This difference can be explained by the shadowing effect.

The shadowing effect is caused by incoming daylight striking a venetian blind slat, which causes a shadow to be created within the space caused by the blocking of the incoming light. The created shadows are formed on surfaces behind them and affect the amount of daylight that can be transmitted into the space, thus affecting transmittance and comfort. The position, size, and orientation of the shadow depends on the incidence angle, slat dimensions, and slat tilt angle.

For medium range β (between 30 and 70 degrees): For medium range θ, between 25 and 40 degrees, the slats create a shadow that covers the gaps between them, thus reducing the amount of light that can be transmitted within the space at this time (which translates into a smaller value for τ). For values of θ over 40 degrees (when light is being transmitted as diffuse into the room), the shadow produced by the slats does not cover the gap, thus the transmittance is higher. In summary, the shadowing effect causes a decrease in the transmittance at the mid ranges of θ, which makes it seem as if the maximum τ is attained at high theta values.

However, for large range β (80 degrees and over): the shadowing effect is more pronounced at high values of the incidence angle, which is why the maximum transmittance remains at medium range thetas (between 25 and 40 degrees). The impact of the shadowing appears, at high θ (over 40 degrees), through the shape of the curve: Compared to all other blind tilt angles, large β show the smallest increase in τ past an incidence angle of 35 degrees. This is due to the shadowing effect: the shadow created with this combination of θ and β leads to the shadow covering the diffuse transmitted daylight going into the space, leading to a very small increase in τ compared to other tilt angles.

The analysis conducted focuses on the following factors to explain the evolution of the transmittance: Sun's position, blind tilt angle, direct and diffuse daylight, shadowing effect, reflection, and absorption. However, transmittance can also be affected by other factors, which explains some of the variations between the curves. In an experimental setup outside of laboratory conditions, these factors need to be considered. Firstly, the atmospheric conditions: The tests were conducted for sunny days. However, atmospheric conditions can change the intensity and the direction of the incident daylight which can slightly affect the results obtained from the data analysis. Another phenomenon that needs to be considered is re-emission: since the tests were conducted for sunny days (which means that the solar heat gains are high), the potential that the blinds absorb light and re-emit it is possible.

5.2- Clear Sky Transmittance Model

For all the blind tilt angles measured, the proposed model for clear sky conditions reduces the RMSE compared to the previous literature model. This difference is mainly noticeable for the 0 degrees blind tilt angle using the small tilt angle equation, and for the 80 degrees blind tilt angles using the large blind tilt angle equation. At the same time, both models provide a close approximation of the experimental results for $\beta = 40$. On averages, the RMSE decreases by 46% for small blind tilt angles, and by 68% for large blind tilt angle, which further highlights the importance of separating the behavior of the AFS based on β range. However, for both models, the highest RMSE values are obtained for the 70 degrees tilt angle (compared to the RMSEs calculated using the same model for other tilt angles). A potential cause of this could be the illuminance not following a bi-modal distribution at this tilt angle. To confirm this theory, a Shapiro-Wilk test was conducted to analyze whether the data is normally distributed.

The Shapiro-Wilk test is designed to assess whether a set of data follows a normal (or bimodal) distribution. A statistic W is calculated to represent how well the data conforms to a normal distribution. Then, the test provides a p-value which is compared to a significance level (usually equal to 0.05) to determine whether the null hypothesis is true or not. In this case, the null hypothesis states that the population is normally distributed. The Shapiro-Wilk test was run for each blind tilt angle to determine whether the transmittance follows a normal distribution. The obtained histograms are shown in Figure 5.3

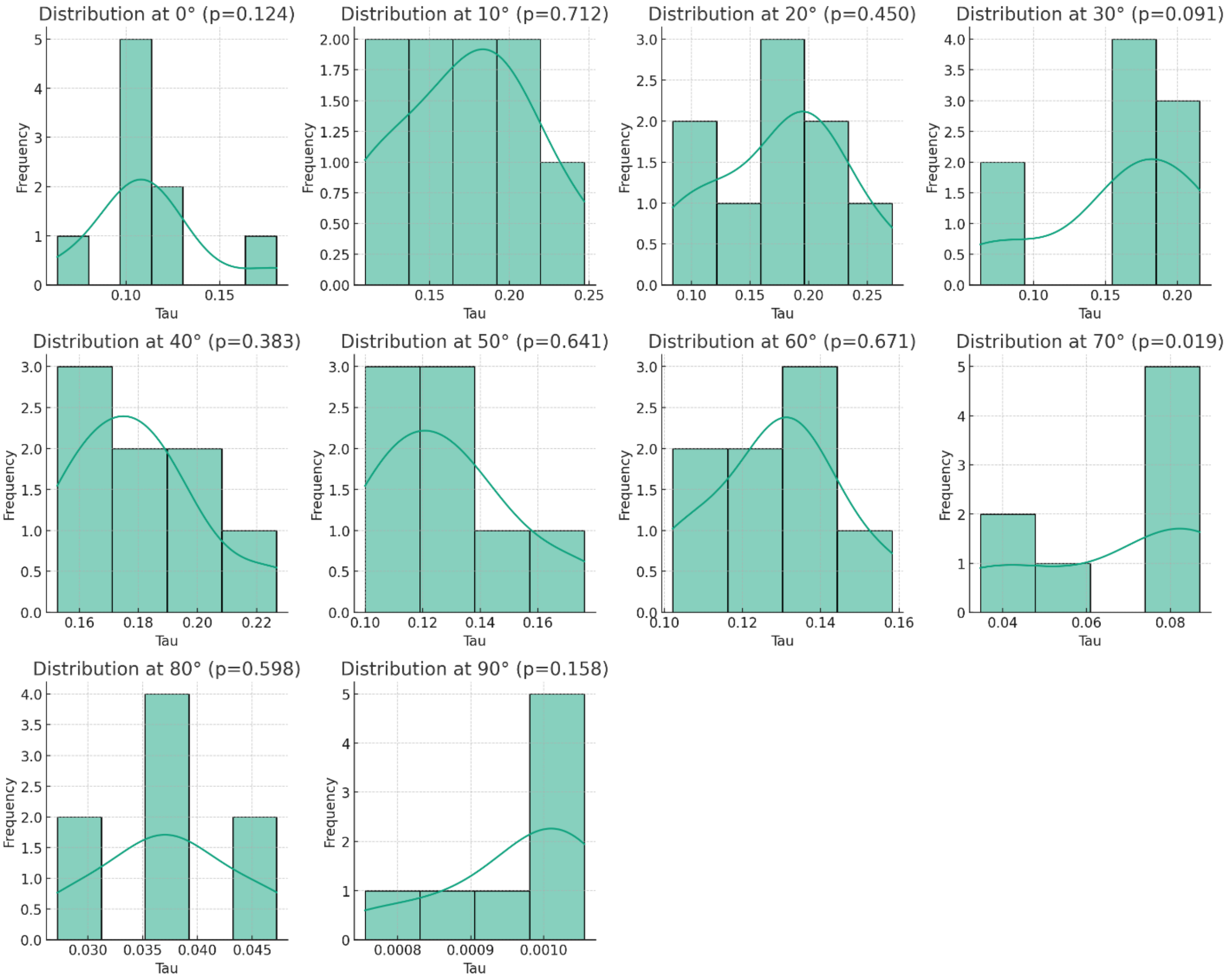
Distribution at 0° (p=0.124)
Distribution at 10° (p=0.712)
Distribution at 20° (p=0.450)
Distribution at 30° (p=0.091)
Distribution at 40° (p=0.383)
Distribution at 50° (p=0.641)
Distribution at 60° (p=0.671)
Distribution at 70° (p=0.019)
Distribution at 80° (p=0.598)
Distribution at 90° (p=0.158)

Figure 5.3: *Output of the Wilk-Shapiro test conducted for the different blind tilt angles under clear conditions.*

The obtained histograms are shown in the above graph. The histograms provide a visual assessment of how well the data aligns with the theoretical normal curve. Where the data seems to fit well under the curve, normality is more likely. The results of the p-values are shown in Table 5.1. A p-value above 0.05 suggests a normal distribution, while a p-value below the significance values suggests that the data is highly unlikely to be normally distributed. The results of the test show that the case where the tilt angle is equal to 70 is the only case where the transmittance does not follow a normal (or bimodal) distribution with regards to the blind tilt angle, thus explaining the highest value of the root mean square error for both the literature model and proposed model. The graph of the experimental illuminance data obtained at $\beta = 70$ is shown in Figure 5.4.

Beta	p-value from the Wilk-Shapiro test	Conclusion
0 degrees	0.124	Data is normally distributed
10 degrees	0.712	Data is normally distributed
20 degrees	0.450	Data is normally distributed
30 degrees	0.091	Data is normally distributed
40 degrees	0.383	Data is normally distributed
50 degrees	0.641	Data is normally distributed
60 degrees	0.671	Data is normally distributed
70 degrees	0.019	Data is NOT normally distributed
80 degrees	0.598	Data is normally distributed
90 degrees	0.158	Data is normally distributed

Table 5.1: *Results of the Wilk-Shapiro test.*

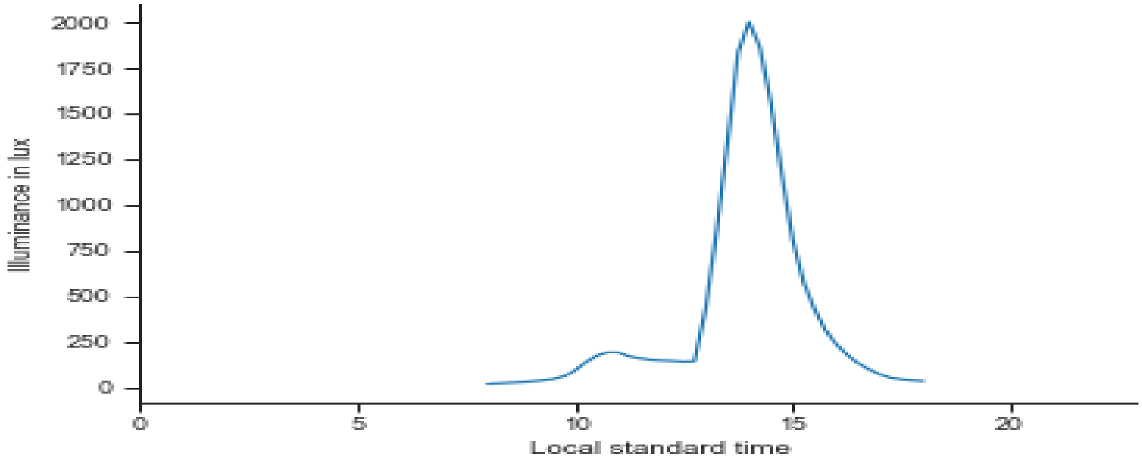

Figure 5.4: *Experimental work plane illuminance for a 70 degrees blind tilt angle under clear conditions.*

The experimental data supports the results from the Wilk-Shapiro test. The illuminance has a very small peak around 10:00 AM, but it is negligeable compared to the second peak around 3:00 PM. The curve is neither a normal nor bi-modal distribution which explains why the proposed model shows a certain margin of error when estimating the illuminance for this blind tilt angle. Since all the other blind tilt angles in the same interval have a bi-modal distribution, it is difficult to pinpoint the exact cause of this anomaly. One possibility is that the shadowing effect has a more complex role at this specific β that differentiates it from the explanation provided in the previous sections. Another possibility could be an error in the data collected by the sensors at that specific time which led to false experimental results. Even though the experiment days were chosen to provide the most uniform outside conditions, a sudden change in the outdoor environment could have caused this anomaly in illuminance levels.

5.3- Dimming Light Approach

The proposed control strategy in section 4.2 only considers the impact of natural daylight on the visual comfort of the office space. Often, artificial lighting sources are used to provide the occupants with another way to control illuminance levels. In office spaces, luminaires allow for a source of diffuse artificial light that does not cause glare. These devices can be used as part of the proposed venetian blinds control strategy through a dimming light approach: a dimming light approach allows for the artificial light to be turned on to a certain percent of its total capacity to offset any light requirements that are not achieved by natural daylight. This can be used for the time periods when the control strategy provides insufficient daylight into the office space (usually at the end of the occupancy period). The dimming light approach can monitor the amount of light entering and function at a certain level of luminosity so that the work plane illuminance reaches the required 300 lux, while also ensuring that glare is within imperceptible levels. At the same time, this approach helps reduce energy consumption for artificial lighting, especially when the full intensity of the luminaires is not required. This strategy coupled with shading device control is common because the same sensors used to monitor the illuminance for the blinds can also be used to determine the artificial light levels needed, thus reducing the overall cost of the setup.

5.4- Impact of Other Parameters on Visual Comfort

The room illuminance is also impacted by other physical factors that were not considered in the sensitivity analysis. As an example, room geometry (as opposed to room dimensions) can play a significant role in determining visual comfort. The most common office space is a rectangular room. However, other configurations can impact the uniformity of lighting within the environment: a good configuration can increase diffuse light on the work plane illuminance, while a bad configuration can create shadows and hotspots that cause visual discomfort and hinder task performance. In addition, the special configuration of the space, including the type of furniture, their position and color, can have an impact on visual comfort.

The visual comfort of the occupants is not only limited to the work plane illuminance and glare levels. Other elements, that are more abstract to quantify numerically, can determine the comfort level of the indoor environment. These elements include but are not limited to the view to the outside and to the perceived control. The view to the outside represents the amount of time during the occupancy period where the user of the space has a clear view to the outside environment. This provides psychological benefits and increased efficiency when it comes to an office space environment. At the same time, perceived control also impacts efficiency in the office space: People generally feel more at ease in settings where they can adjust their lighting conditions. Being able to modify aspects like light intensity or manage window coverings can enhance both their comfort and overall satisfaction.

6. Chapter 6: Conclusion

This thesis presents a heating season control strategy for a triple glazed south facing window with integrated bi-facial silicon photovoltaic cells with inner-pane venetian blinds in a single person office space in Montreal that prioritizes visual comfort and maximizes passive solar heating gains. The strategy is based on two visual transmittance models: one for cloudy sky conditions, and another for clear conditions. The models were developed and validated using experimental data from a test cell located in the Future Building Lab in Loyola Campus.

The first part of the work presents the transmittance models. The equations was developed based on experimental results and are a function of the incidence angle of the sun and the tilt angle of the blinds. The clear model categorizes the visual properties of the AFS based on the range of the blind tilt angles. The experimental results show that it accurately mimics the real time behavior since the average RMSE decrease for small blind tilt angles compared to previous transmittance models found in literature is 46%. For larger blind tilt angles, this decrease is equal to 68%. For cloudy conditions, the impact of the incidence angle is most noticeable during midday. The proposed model slightly improves on previous literature by taking into account θ..

The second part represents the control strategy that automates the blind tilt angle position at every 15-minute timestep to ensure that the work plane illuminance remains above the 300-lux threshold, while glare remains below the 0.35 imperceptible glare threshold. The approach also accounts for the occupancy schedule of the office space to maximize passive solar gains. During a clear day, the results show that applying the control strategy compared to a pre-set tilt position allows for a significant decrease in glare levels while ensuring comfort in terms of blind tilt angle. Under cloudy conditions, the control strategy approach improves the work plane illuminance compared to the pre-set case, while keeping glare in the imperceptible range.

The control strategy was tested within a single person's office space to simulate the outputs and validate the results. Finally, a sensitivity analysis was conducted through simulation to determine the impact of varying the physical properties of the space on the visual comfort. The three key factors analyzed are the window to wall ratio, the room dimensions, and the reflectance of the surfaces. A smaller WWR leads to a decrease in illuminance, going below the established threshold by the end of the occupancy period, while keeping glare at acceptable levels. In terms of room size, a larger space leads to decreased work plane illuminance, while a smaller space increases it. This is because a larger space, thus larger surface areas, increases their absorption and decreases the light intensity as it travels to the center of the space. The reflectance of these surfaces also plays a role in determining the work plane illuminance since opaque surfaces decrease it, while highly reflective surfaces increase it.

6.1- Contributions

- This study analyzes the visual properties of an advanced fenestration system triple glazed south facing window with integrated bi-facial silicon photovoltaic cells with inner-pane venetian blinds to enhance the understanding of its visual properties on an office space setting. The analysis considers each aspect of the AFS and its interactions with the different elements that impact the visual comfort within the indoor environment.

- This study presents visual transmittance models for the studied AFS under clear and overcast sky conditions. The models were compared to transmittance equations from previous literature. They were then validated using experimental results to ensure that they represent the real-life visual properties of the window.

- This study proposes a control strategy to be used in the heating season to optimize the visual comfort of the indoor environment in terms of work plane illuminance and glare levels while also maximizing passive solar gains to reduce energy consumption. The control approach also takes into account the occupancy schedule of the individual and is scalable for different spaces.

- This study simulated the transmittance model and the control strategy into a real-life case study office space located in Montreal, Quebec, in order to validate the obtained outputs.

- This study discusses the impact of different physical parameters on the light levels of the office space. The results of different window to wall ratios, room dimensions, and surfaces reflectance are analyzed and their impact on work plane illuminance and glare levels is presented.

6.2- Limitations

- Due to time constraints, the control strategy was not implemented in the test cell to validate the work plane illuminance and glare levels. Based on the validation of the transmittance model and radiosity analysis, it is assumed that the results of the control strategy are accurate (since the same approach and equations were used in the calculations). Also, a manual change in the tilt angle of the blinds in the case of the control strategy can lead to inaccurate results, especially since the tilt angle must be adjusted every 15 minutes.

- Since the data collected from the test location span over a significant period of time to account for weather and sky conditions (the first test day was the 20th of September 2023 and the last test day was the 30th of April 2024), some sensor calibration might have decreased in accuracy, especially for the sensors located on the outer glazing since they are exposed to outdoor climate conditions like rain and snow.

- The control strategy only considers primarily the visual comfort of the occupants but does not quantify the amount of passive solar gains since it is outside the scope of this work. However, maximizing passive solar gains, even during heating season, can lead to thermal discomfort for the occupants.

- The control strategy calculates the work plane illuminance and simplified daylight glare probability for every blind tilt angle at every time step, which can slow down the performance once it is applied to a controller in a real-life scenario and impact the overall execution of the algorithm. One possibility to bypass this issue would be to increase the time between each iteration (from 15-minute intervals to 30-minute intervals), or to iterate over increments of 10 degrees instead of 5 degrees. This becomes a trade-off between computational performance and accuracy of the optimal tilt angle.

6.3- Future Work

The work presented in this thesis creates a baseline for the visual properties of a unique AFS and shows how it can be integrated within a control strategy to enhance the comfort and reduce energy consumption within a specific space. This can be expanded upon in different ways:

- The control strategy can be implemented with a thermal model to ensure both visual and thermal comfort. An approach like the PMV-PPD, developed by Fanger (1988), can be used to evaluate how comfortable the space is for the occupants. The predicted mean value rates the thermal comfort levels of the occupants within a 7-point scale ranging from hot to cold, while the predicted percentage of dissatisfied PPD uses the PMV to determine how many people are dissatisfied with the thermal conditions of a space. Using the air velocity, air temperature, mean radiant temperature, air humidity, clothing resistance, and activity level at every time step, the PMV can be calculated, and the thermal comfort can be enhanced through the correct management of the passive solar gains and the HVAC system. Figure 6.1 presents the scale and the PMV-PPD curves

Value	Sensation
+3	Hot
+2	Warm
+1	Slightly warm
0	Neutral
-1	Slightly cool
-2	Cool
-3	Cold

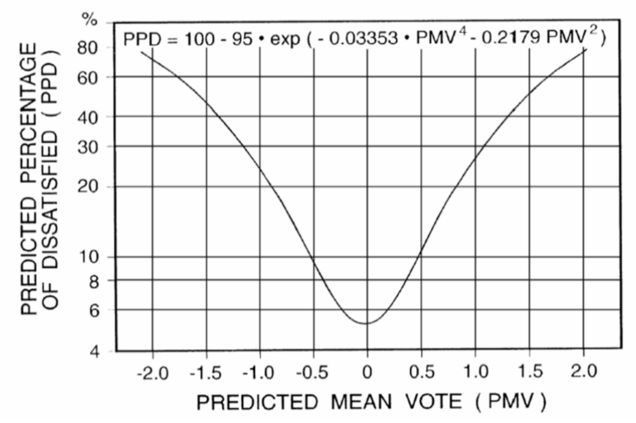

<u>Figure 6.1:</u> *Thermal sensation scale (left) and PPD based on the PMV curve (right). (Source: ASHRAE, 2017).*

- Implementing an energy consumption-production method can help with determining if the space is energy efficient. By calculating the energy produced by the PVs at every time step, and the energy consumed for lighting and climate control, the energy efficiency of the space can be evaluated and improved. This will help with setting up other control strategies parallel to the one considered in this thesis such as a dimming artificial light approach to ensure visual comfort when natural light is not sufficient.

- This study used experimental data to validate the models developed. However, as discussed in the literature review, a common approach is using surveys / questionnaires based on the subjective input of test subjects to solidify visual comfort claims. This approach can be used with the experimental results to solidify the conclusions made in this work.

- The office space studied is south facing. However, an interesting analysis would be to evaluate the window orientation's impact on the visual comfort of the space. Because of the location of the space in Montreal, it is assumed that an East facing window would lead to high illuminance in the morning but with glare potential. For the case of West facing windows, the peak illuminance is expected in the late afternoon with potential for glare. For a North facing window, light levels will be lower throughout the occupancy period, but with the benefits of less glare during the day. These results can be validated through simulation in a future project.

7. References

Aguilar-Santana, J. L., Velasco-Carrasco, M., & Riffat, S. (2020). Thermal Transmittance (U-value) Evaluation of Innovative Window Technologies. Future Cities and Environment, 6(1), 12. https://doi.org/10.5334/fce.99.

Alkhatib, H., Lemarchand, P., Norton, B., & O'Sullivan, D. T. J. (2021). Deployment and control of adaptive building facades for energy generation, thermal insulation, ventilation and daylighting: A review. Applied Thermal Engineering, 185, 116331. https://doi.org/10.1016/j.applthermaleng.2020.116331.

Al-Masrania, S. M., Al-Obaidi, K. M. (2019). Dynamic shading systems: A review of design parameters, platforms and evaluation strategies. Automation in Construction, 102, 195-216.

American Society of Heating, Refrigerating and Air-Conditioning Engineers. (2017). ASHRAE handbook: Fundamentals – SI edition. Atlanta, GA.

ASHRAE. (2016). ASHRAE Standard 90.1 – Performance Rating Method Reference Manual. Atlanta, US: American Society of Heating Refrigeration and Air Conditioning Engineers, Inc.

ASHRAE. (2022). Standard 90.1-2022 (I-P Edition): Energy Standard for Sites and Buildings Except Low-Rise Residential Buildings. American Society of Heating, Refrigerating, and Air-Conditioning Engineers.

Athienitis, A. K., & Tzempelikos, A. (2002). A methodology for simulation of daylight room illuminance distribution and light dimming for a room with a controlled shading device. Solar Energy, 72(4), 271–281. https://doi.org/10.1016/S0038-092X(02)00016-6.

Baril, D. (2023, March 7). Future Buildings Lab image. In S. Hanley, Could planting trees around a building help offset its greenhouse-gas emissions? Yes, says new study, but not enough. Concordia University News. https://www.concordia.ca/cunews/encs/2023/03/07/trees-offset-greenhosuse-gases-buildings.html.

Barkaszi, S. F., & Dunlop, J. P. (2001). Discussion of Strategies for Mounting Photovoltaic Arrays on Rooftops. Solar Engineering 2001: (FORUM 2001: Solar Energy — The Power to Choose), 333–338. https://doi.org/10.1115/SED2001-142.

Barman, S., Chowdhury, A., Mathur, S., & Mathur, J. (2018). Assessment of the efficiency of window integrated CdTe based semi-transparent photovoltaic module. Sustainable Cities and Society, 37, 250–262. https://doi.org/10.1016/j.scs.2017.09.036.

Bellia, L., Fragliasso, F., & Stefanizzi, E. (2017). Daylit offices: A comparison between measured parameters assessing light quality and users' opinions. Building and Environment, 113, 92–106. https://doi.org/10.1016/j.buildenv.2016.08.014.

Bessoudo, M., Athienitis, A., Zmeureanu, R., & Tzempelikos, A. (2010). Indoor thermal environmental conditions near glazed facades with shading devices – Part II: Thermal comfort simulation and impact of glazing and shading properties. Building and Environment, 45, 2517–2525. https://doi.org/10.1016/j.buildenv.2010.05.014.

Biyik, E., Araz, M., Hepbasli, A., Shahrestani, M., Yao, R., Shao, L., Essah, E., Oliveira, A. C., Del Caño, T., Rico, E., Lechón, J. L., Andrade, L., Mendes, A., & Atlı, Y. B. (2017). A key review of building integrated photovoltaic (BIPV) systems. Engineering Science and Technology, an International Journal, 20(3), 833–858. https://doi.org/10.1016/j.jestch.2017.01.009.

BSI. 2014. ISO 9869-1:2014- Thermal insulation — Building elements — Insitu measurement of thermal resistance and thermal transmittance; Part 1: Heat flow meter method, p. 48.

Cannavale, A., Hörantner, M., Eperon, G. E., Snaith, H. J., Fiorito, F., Ayr, U., & Martellotta, F. (2017). Building integration of semitransparent perovskite-based solar cells: Energy performance and visual comfort assessment. Applied Energy, 194, 94–107. https://doi.org/10.1016/j.apenergy.2017.03.011.

Chae, Y. T., Kim, J., Park, H., & Shin, B. (2014). Building energy performance evaluation of building integrated photovoltaic (BIPV) window with semi-transparent solar cells. Applied Energy, 129, 217–227. https://doi.org/10.1016/j.apenergy.2014.04.106.

Chaiwiwatworakul, P., Chirarattananon, S., & Rakkwamsuk, P. (2009). Application of automated blind for daylighting in tropical region. Energy Conversion and Management, 50(12), 2927–2943. https://doi.org/10.1016/j.enconman.2009.07.008.

Chan, Y.-C., & Tzempelikos, A. (2013). Efficient venetian blind control strategies considering daylight utilization and glare protection. Solar Energy, 98, 241–254. https://doi.org/10.1016/j.solener.2013.10.005.

Chen, Y., Athienitis, A. K., & Galal, K. (2010). Modeling, design and thermal performance of a BIPV/T system thermally coupled with a ventilated concrete slab in a low energy solar house: Part 1, BIPV/T system and house energy concept. Solar Energy, 84(11), 1892–1907. https://doi.org/10.1016/j.solener.2010.06.013.

CIE 85 (1989) Technical Report, Solar Spectral Irradiance. CIE Publication no. 85, TC 2.17, Commission Internationale de l’Eclairage.

Cuce, E., & Riffat, S. B. (2015). A state-of-the-art review on innovative glazing technologies. Renewable and Sustainable Energy Reviews, 41, 695–714. https://doi.org/10.1016/j.rser.2014.08.084.

Cuce, E., Young, C.-H., & Riffat, S. B. (2014). Performance investigation of heat insulation solar glass for low-carbon buildings. Energy Conversion and Management, 88, 834–841. https://doi.org/10.1016/j.enconman.2014.09.021.

Cui, Y., Ke, Y., Liu, C., Chen, Z., Wang, N., Zhang, L., Zhou, Y., Wang, S., Gao, Y., & Long, Y. (2018). Thermochromic VO2 for Energy-Efficient Smart Windows. Joule, 2(9), 1707–1746. https://doi.org/10.1016/j.joule.2018.06.018.

Dirnberger, D. (2015). Uncertainties in Energy Rating for Thin-film PV Modules. https://doi.org/10.13140/RG.2.1.3020.1687.

Doulos, L., Tsangrassoulis, A., & Topalis, F. (2005). A CRITICAL REVIEW OF SIMULATION TECHNIQUES FOR DAYLIGHT RESPONSIVE SYSTEMS.

Dounis, A. I., & Caraiscos, C. (2009). Advanced control systems engineering for energy and comfort management in a building environment—A review. Renewable and Sustainable Energy Reviews, 13(6–7), 1246–1261. https://doi.org/10.1016/j.rser.2008.09.015

Einhorn, H.D. (1969). A new method for the assessment of discomfort glare, Lighting Research and Technology 1 (4) 235–247.

Evola, G., Gullo, F., & Marletta, L. (2017). The role of shading devices to improve thermal and visual comfort in existing glazed buildings. Energy Procedia, 134, 346–355. https://doi.org/10.1016/j.egypro.2017.09.543.

F. Reinhart, C., J. Alstan, J. and Ibarra, D. (2013) 'DEFINITION OF A REFERENCE OFFICE FOR STANDARDIZED EVALUATIONS.pdf'.

Fang, Y., Eames, P. C., Norton, B., Hyde, T. J., Zhao, J., Wang, J., & Huang, Y. (2007). Low emittance coatings and the thermal performance of vacuum glazing. Solar Energy, 81(1), 8–12. https://doi.org/10.1016/j.solener.2006.06.011.

Fanger, P. O. (1988). Fundamentals of thermal comfort. In Advances In Solar Energy Technology (pp. 3056-3061). Pergamon.

Favoino, F., Loonen, R. C. G. M., Michael, M., De Michele, G., & Avesani, S. (2022). Advanced fenestration—Technologies, performance and building integration. In Rethinking Building Skins (pp. 117–154). Elsevier. https://doi.org/10.1016/B978-0-12-822477-9.00038-3.

Feng, F., Kunwar, N., Cetin, K., & O’Neill, Z. (2021). A critical review of fenestration/window system design methods for high performance buildings. Energy and Buildings, 248, 111184. https://doi.org/10.1016/j.enbuild.2021.111184.

Galasiu, A. D., Atif, M. R., & MacDonald, R. A. (2004). Impact of window blinds on daylight-linked dimming and automatic on/off lighting controls. Solar Energy, 76(5), 523–544. https://doi.org/10.1016/j.solener.2003.12.007.

Ghosh, A. (2022). Fenestration integrated BIPV (FIPV): A review. Solar Energy, 237, 213–230. https://doi.org/10.1016/j.solener.2022.04.013.

Gong, J., Liang, J., & Sumathy, K. (2012). Review on dye-sensitized solar cells (DSSCs): Fundamental concepts and novel materials. Renewable and Sustainable Energy Reviews, 16(8), 5848–5860. https://doi.org/10.1016/j.rser.2012.04.044.

Green, M., Dunlop, E., Hohl-Ebinger, J., Yoshita, M., Kopidakis, N., & Hao, X. (2021). Solar cell efficiency tables (version 57). Progress in Photovoltaics: Research and Applications, 29(1), 3–15. https://doi.org/10.1002/pip.3371.

Guerrero-Lemus, R., Vega, R., Kim, T., Kimm, A., & Shephard, L. E. (2016). Bifacial solar photovoltaics – A technology review. Renewable and Sustainable Energy Reviews, 60, 1533–1549. https://doi.org/10.1016/j.rser.2016.03.041.

Hassan, Q., Jaszczur, M., Przenzak, E., & Abdulateef, J. (2016). The PV cell temperature effect on the energy production and module efficiency.

Henemann, A. (2008). BIPV: Built-in solar energy. Renewable Energy Focus, 9(6), 14–19. https://doi.org/10.1016/S1471-0846(08)70179-3.

Hirning, M. B., Isoardi, G. L., & Cowling, I. (2014). Discomfort glare in open plan green buildings. Energy and Buildings, 70, 427–440. https://doi.org/10.1016/j.enbuild.2013.11.053.

Huchuk, B., Gunay, H. B., O'Brien, W., & Cruickshank, C. A. (2016). Model-based predictive control of office window shades. Building Research & Information, 44(4), 445–455. https://doi.org/10.1080/09613218.2016.1101949

Iwata, T., Hatao, A., Shukuya, M., & Kimura, K. -i. (1994). Visual comfort in the daylit luminous environment: Structural model for evaluation. Lighting Research and Technology, 26(2), 91–97. https://doi.org/10.1177/096032719402600203.

Jain, S., & Garg, V. (2018). A review of open loop control strategies for shades, blinds and integrated lighting by use of real-time daylight prediction methods. Building and Environment, 135, 352–364. https://doi.org/10.1016/j.buildenv.2018.03.018.

Jain, S., & Garg, V. (2018). A review of open loop control strategies for shades, blinds and integrated lighting by use of real-time daylight prediction methods. Building and Environment, 135, 352–364. https://doi.org/10.1016/j.buildenv.2018.03.018.

Jakubiec, J. A., Srisamranrungruang, T., Kong, Z., Quek, G., & Talami, R. (2019). Subjective and Measured Evidence for Residential Lighting Metrics in the Tropics. 1151–1159. https://doi.org/10.26868/25222708.2019.210898.

Jelle, B. P., & Breivik, C. (2012). The Path to the Building Integrated Photovoltaics of Tomorrow. Energy Procedia, 20, 78–87. https://doi.org/10.1016/j.egypro.2012.03.010.

Jelle, B. P., Hynd, A., Gustavsen, A., Arasteh, D., Goudey, H., & Hart, R. (2012). Fenestration of today and tomorrow: A state-of-the-art review and future research opportunities. Solar Energy Materials and Solar Cells, 96, 1–28. https://doi.org/10.1016/j.solmat.2011.08.010.

Kang, J.-G., Kim, J.-H., & Kim, J.-T. (2013). Performance Evaluation of DSC Windows for Buildings. International Journal of Photoenergy, 2013, 1–6. https://doi.org/10.1155/2013/472086.

Ke, et al., Smart windows: electro-, thermo-, mechano-, photochromics, and beyond, Adv. Energy Mater. 9 (39) (2019) 1902066.

Kim, J.-H., Park, Y.-J., Yeo, M.-S., & Kim, K.-W. (2009). An experimental study on the environmental performance of the automated blind in summer. Building and Environment, 44(7), 1517–1527. https://doi.org/10.1016/j.buildenv.2008.08.006.

Kong, H., Yu, Z., Zhang, J., Han, Y., Wu, L., Wang, H., & Wang, J. (2020). Perspective of CIGS-BIPV's Product Competitiveness in China. International Journal of Photoenergy, 2020, 1–10. https://doi.org/10.1155/2020/5392594.

Kong, Z., Utzinger, D. M., Freihoefer, K., & Steege, T. (2018). The impact of interior design on visual discomfort reduction: A field study integrating lighting environments with POE survey. Building and Environment, 138, 135–148. https://doi.org/10.1016/j.buildenv.2018.04.025.

Korsavi, S. S., Zomorodian, Z. S., & Tahsildoost, M. (2016). Visual comfort assessment of daylit and sunlit areas: A longitudinal field survey in classrooms in Kashan, Iran. Energy and Buildings, 128, 305–318. https://doi.org/10.1016/j.enbuild.2016.06.091.

Kreinin, L., Karsenty, A., Grobgeld, D., & Eisenberg, N. (2016). PV systems based on bifacial modules: Performance simulation vs. design factors. 2016 IEEE 43rd Photovoltaic Specialists Conference (PVSC), 2688–2691. https://doi.org/10.1109/PVSC.2016.7750138.

Kuhn, T. E. (2017). State of the art of advanced solar control devices for buildings. Solar Energy, 154, 112–133. https://doi.org/10.1016/j.solener.2016.12.044.

Lee, E. S., DiBartolomeo, D. L., & Selkowitz, S. E. (1998). Thermal and daylighting performance of an automated venetian blind and lighting system in a full-scale private office. Energy and Buildings, 29(1), 47–63. https://doi.org/10.1016/S0378-7788(98)00035-8.

LI-COR, Inc. (2022a). LI-200R Pyranometer. Lincoln, NE: LI-COR Environmental. Retrieved from https://www.licor.com/env/products/light/pyranometer.

LI-COR, Inc. (2022b). LI-210R Photometric Sensor. Lincoln, NE: LI-COR Environmental. Retrieved from https://www.licor.com/env/products/light/photometric.

Loonen, R. C. G. M., Trčka, M., Cóstola, D., & Hensen, J. L. M. (2013). Climate adaptive building shells: State-of-the-art and future challenges. Renewable and Sustainable Energy Reviews, 25, 483–493. https://doi.org/10.1016/j.rser.2013.04.016.

Lu, L., & Law, K. M. (2013). Overall energy performance of semi-transparent single-glazed photovoltaic (PV) window for a typical office in Hong Kong. Renewable Energy, 49, 250–254. https://doi.org/10.1016/j.renene.2012.01.021.

Maghrabie, H. M., Elsaid, K., Sayed, E. T., Abdelkareem, M. A., Wilberforce, T., & Olabi, A. G. (2021). Building-integrated photovoltaic/thermal (BIPVT) systems: Applications and challenges. Sustainable Energy Technologies and Assessments, 45, 101151. https://doi.org/10.1016/j.seta.2021.101151.

Mahdavi, A., & Spasojevic, B. (2006). An energy-efficient simulation-assisted lighting control system for buildings.

Mangkuto, R. A., Kurnia, K. A., Azizah, D. N., Atmodipoero, R. T., & Soelami, F. X. N. (2017). Determination of discomfort glare criteria for daylit space in Indonesia. Solar Energy, 149, 151–163. https://doi.org/10.1016/j.solener.2017.04.010.

Mende, S., Frontini, F. and Wienold, J. (2011) 'Comfort and building performance analysis of transparent building integrated silicon photovoltaics' p.9.

Ming, Y., Sun, Y., Liu, X., Liu, X., & Wu, Y. (2024). Thermal performance of an advanced smart fenestration systems for low-energy buildings. Applied Thermal Engineering, 244, 122610. https://doi.org/10.1016/j.applthermaleng.2024.122610.

Murdoch J. B. (1985). Illumination Engineering—From Edison's Lamp to the Laser, Macmillan Publishing Inc, New York.

Nabil, A., & Mardaljevic, J. (2005). Useful daylight illuminance: A new paradigm for assessing daylight in buildings. Lighting Research & Technology, 37(1), 41–57. https://doi.org/10.1191/1365782805li128oa.

National Fenestration Rating Council (NFRC). 2017. NFRC 200-2017, Procedure for Determining Fenestration Product Solar Heat Gain Coefficient and Visible Transmittance at Normal Incidence, National Fenestration Rating Council, Inc., Greenbelt, MD.

Natural Resources Canada (2016). Report on Plans and Priorities. Minister of Natural Resources.

Natural Resources Canada (2017). Report on Plans and Priorities. Minister of Natural Resources.

Natural Resources Canada. (2023a). Energy efficiency: An essential part of Canada's net-zero future - Report to Parliament under the Energy Efficiency Act 2021-2022.

Natural Resources Canada. (2023b). 2023-24 Departmental plan. Retrieved from https://www.nrcan.gc.ca/transparency/reporting-and-accountability/plans-and-performance-reports/departmental-plan/205.

Naylor, D., & Lai, B. Y. (2007). Experimental Study of Natural Convection in a Window with a Between-Panes Venetian Blind. Experimental Heat Transfer, 20(1), 1–17. https://doi.org/10.1080/08916150600977358.

Ng, P. K., Mithraratne, N., & Kua, H. W. (2013). Energy analysis of semi-transparent BIPV in Singapore buildings. Energy and Buildings, 66, 274–281. https://doi.org/10.1016/j.enbuild.2013.07.029.

Park, K. E., Kang, G. H., Kim, H. I., Yu, G. J., & Kim, J. T. (2010). Analysis of thermal and electrical performance of semi-transparent photovoltaic (PV) module. Energy, 35(6), 2681–2687. https://doi.org/10.1016/j.energy.2009.07.019.

Piccolo, A., & Simone, F. (2015). Energy Performance of an All-Solid State Electrochromic Prototype for Smart Window Applications. Energy Procedia, 78, 110–115. https://doi.org/10.1016/j.egypro.2015.11.123.

Quesada, G., Rousse, D., Dutil, Y., Badache, M., & Hallé, S. (2012). A comprehensive review of solar facades. Opaque solar facades. Renewable and Sustainable Energy Reviews, 16(5), 2820–2832. https://doi.org/10.1016/j.rser.2012.01.078.

Reinhart, C. F., Mardaljevic, J., & Rogers, Z. (2006). Dynamic Daylight Performance Metrics for Sustainable Building Design. LEUKOS, 3(1), 7–31. https://doi.org/10.1582/LEUKOS.2006.03.01.001.

Richhariya, G., Kumar, A., Tekasakul, P., & Gupta, B. (2017). Natural dyes for dye sensitized solar cell: A review. Renewable and Sustainable Energy Reviews, 69, 705–718. https://doi.org/10.1016/j.rser.2016.11.198.

Robinson, L., & Athienitis, A. (2009). DESIGN METHODOLOGY FOR OPTIMIZATION OF ELECTRICITY GENERATION AND DAYLIGHT UTILIZATION FOR FAÇADE WITH SEMITRANSPARENT PHOTOVOLTAICS. 8.

Robinson, L., & Athienitis, A. (2009). DESIGN METHODOLOGY FOR OPTIMIZATION OF ELECTRICITY GENERATION AND DAYLIGHT UTILIZATION FOR FAÇADE WITH SEMITRANSPARENT PHOTOVOLTAICS. 8.

Russell, T. C. R., Saive, R., Augusto, A., Bowden, S. G., & Atwater, H. A. (2017). The Influence of Spectral Albedo on Bifacial Solar Cells: A Theoretical and Experimental Study. IEEE Journal of Photovoltaics, 7(6), 1611–1618. https://doi.org/10.1109/JPHOTOV.2017.2756068.

Sanati, L., & Utzinger, M. (2013). The effect of window shading design on occupant use of blinds and electric lighting. Building and Environment, 64, 67–76. https://doi.org/10.1016/j.buildenv.2013.02.013.

Santbergen, R., & Van Zolingen, R. J. C. (2008). The absorption factor of crystalline silicon PV cells: A numerical and experimental study. Solar Energy Materials and Solar Cells, 92(4), 432–444. https://doi.org/10.1016/j.solmat.2007.10.005.

Selvaraj, P., Ghosh, A., Mallick, T. K., & Sundaram, S. (2019). Investigation of semi-transparent dye-sensitized solar cells for fenestration integration. Renewable Energy, 141, 516–525. https://doi.org/10.1016/j.renene.2019.03.146.

Shafavi, N. S., Zomorodian, Z. S., Tahsildoost, M., & Javadi, M. (2020). Occupants visual comfort assessments: A review of field studies and lab experiments. Solar Energy, 208, 249–274. https://doi.org/10.1016/j.solener.2020.07.058.

Shirazi, A. M., Zomorodian, Z. S., & Tahsildoost, M. (2019). Techno-economic BIPV evaluation method in urban areas. Renewable Energy, 143, 1235–1246. https://doi.org/10.1016/j.renene.2019.05.105.

Sigounis, A.-M., Vallianos, C., & Athienitis, A. (2023). Model predictive control of air-based building integrated PV/T systems for optimal HVAC integration. Renewable Energy, 212, 655–668. https://doi.org/10.1016/j.renene.2023.05.059.

Stanley, C., Mojiri, A., & Rosengarten, G. (2016). Spectral light management for solar energy conversion systems. Nanophotonics, 5(1), 161–179. https://doi.org/10.1515/nanoph-2016-0035.

Susorova, I., Tabibzadeh, M., Rahman, A., Clack, H. L., & Elnimeiri, M. (2013). The effect of geometry factors on fenestration energy performance and energy savings in office buildings. Energy and Buildings, 57, 6-13.

Tabadkani, A., Roetzel, A., Li, H. X., & Tsangrassoulis, A. (2020). A review of automatic control strategies based on simulations for adaptive facades. Building and Environment, 175, 106801. https://doi.org/10.1016/j.buildenv.2020.106801.

Tzempelikos, A., & Athienitis, A. K. (2007). The impact of shading design and control on building cooling and lighting demand. Solar Energy, 81(3), 369–382. https://doi.org/10.1016/j.solener.2006.06.015.

U.S. Department of Energy. (n.d.). Solar radiation basics. Energy.gov. Retrieved April 2024, from https://www.energy.gov/eere/solar/solar-radiation-basics.

United Nations Environment Programme. (2020). 2020 Global Status Report for Buildings and Construction: Towards a Zero-emission, Efficient, and Resilient Buildings and Construction Sector. United Nations Environment Programme.

Valdivia, C. E., Li, C. T., Russell, A., Haysom, J. E., Li, R., Lekx, D., Sepeher, M. M., Henes, D., Hinzer, K., & Schriemer, H. P. (2017). Bifacial Photovoltaic Module Energy Yield Calculation and Analysis. 2017 IEEE 44th Photovoltaic Specialist Conference (PVSC), 1094–1099. https://doi.org/10.1109/PVSC.2017.8366206.

Vats, K., Tomar, V., & Tiwari, G. N. (2012). Effect of packing factor on the performance of a building integrated semitransparent photovoltaic thermal (BISPVT) system with air duct. Energy and Buildings, 53, 159–165. https://doi.org/10.1016/j.enbuild.2012.07.004.

Wagner, A., O'Brien, W., & Dong, B. (2018). Exploring occupant behavior in buildings. Wagner, A., O'Brien, W., Dong, B., Eds, 55, 1267-1273.

Wienold, J. (2010) Daylight glare in offices. Stuttgart: Fraunhofer-Verl.

Wienold, J., & Christoffersen, J. (2006). Evaluation methods and development of a new glare prediction model for daylight environments with the use of CCD cameras. Energy and Buildings, 38(7), 743–757. https://doi.org/10.1016/j.enbuild.2006.03.017.

Wong and Chan, Smart glass and its potential in energy savings, J. Energy Res. Technol. 136 (1) (2014).

Yu, G., Yang, H., Luo, D., Cheng, X., & Ansah, M. K. (2021). A review on developments and research of building integrated photovoltaic (BIPV) windows and shading blinds. Renewable and Sustainable Energy Reviews, 149, 111355. https://doi.org/10.1016/j.rser.2021.111355.

Yun, G., Yoon, K.C. and Kim, K.S. (2014) 'The influence of shading control strategies on the visual comfort and energy demand of office buildings', Energy and Buildings, 84, pp. 70–85. Available at: https://doi.org/10.1016/j.enbuild.2014.07.040.

Yusufoglu, U. A., Pletzer, T. M., Koduvelikulathu, L. J., Comparotto, C., Kopecek, R., & Kurz, H. (2015). Analysis of the Annual Performance of Bifacial Modules and Optimization Methods. IEEE Journal of Photovoltaics, 5(1), 320–328. https://doi.org/10.1109/JPHOTOV.2014.2364406.

8. Appendix

Appendix A: Experimental Results

A blind tilt angle of 0 degrees is used to represent the data distribution for smaller blind tilt angles (ranging from 0 to 40 degrees), while a tilt of 50 degrees serves as a baseline for larger angles (between 50 and 80 degrees). Some of this data was subsequently utilized to create a visual transmittance model for the studied advanced fenestration system. The rest is used to validate the model for different blind tilt angles and different outdoor conditions.

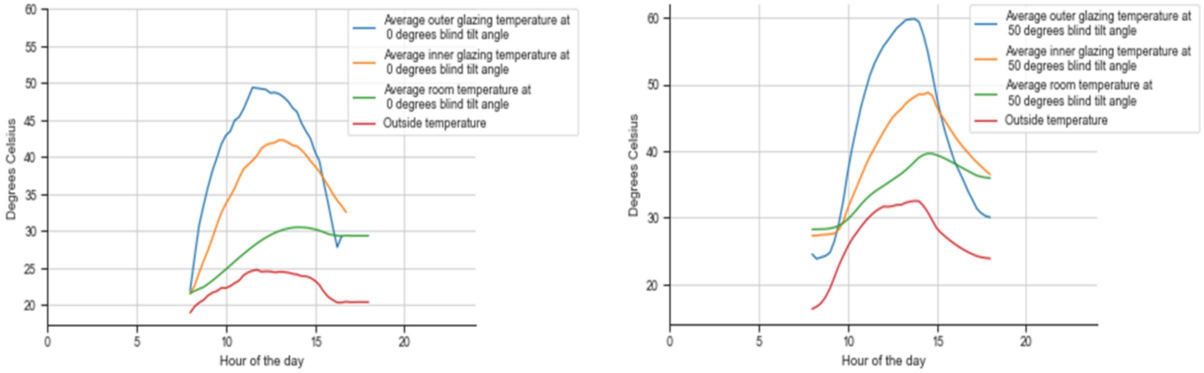

Figure A-8.1: *Experimental temperature outputs for a blind tilt angle of 0 degrees (left) and blind tilt angle of 50 degrees (right) under clear sky conditions.*

The data for the temperatures shown in Figure A-8.1 were taken on two different sunny days. For the blind tilt angle of 0 degrees, the data was collected on the 20th of September 2023, while the blind tilt angle of 50 degrees data was obtained on the 1st of October 2023, which explains the difference in the outside temperature. The results show that the most important factor that determines the temperature of the indoor environment is the outside temperature. Although theoretically, more solar radiation enters the test cell when $\beta = 0$ than at $\beta = 50$, the office space tends to be warmer on average in the latter scenario:

On the 20th of September, the room temperature's maximum is at 31 degrees Celsius but reaches 40 degrees on the 1st of October. This is because the second day is warmer, reaching a peak of 32°C around noon compared to the first day, with a peak at 25°C. The impact of the outdoor environment also appears in the temperature of the inner and outer glazing, with the outer glazing reaching a maximum of 60°C at its peak. However, the temperature results from both days follow similar trends: the highest temperatures are those of the outside glazing, followed by the inner glazing and the indoor space, because of the solar radiation being absorbed as it is transmitted and reflected from one surface to another. The maximum of each curve is reached around solar noon, which is the time of day where the incidence angle of the sun is at its maximum. This translates to the different surfaces being exposed to the greatest amount of solar radiation. The same trends are seen during overcast days, with the outside temperature being higher than the other temperatures because of the less intense exposure to direct solar radiation.

At the same time, the high temperatures of the outer glazing can lead to the silicon PV cells overheating, reducing their efficiency, and damaging their lifetime performance. In fact, if the PV cells are considered independently of the glass around them, their temperature surpasses the temperature of the glass and the average temperature of the glazing as seen in the figures below. On the hotter day ($\beta = 50$), the temperature of the cells can reach a maximum of 65°C. This is because the photovoltaic cells absorb more solar radiation that will later on be converted into electricity. This phenomenon is reflected in the temperature trends of both the glass and the cells: they begin the day at nearly identical temperatures, but as the day progresses, their temperature difference widens, reaching its maximum around solar noon (Figure A-8.2).

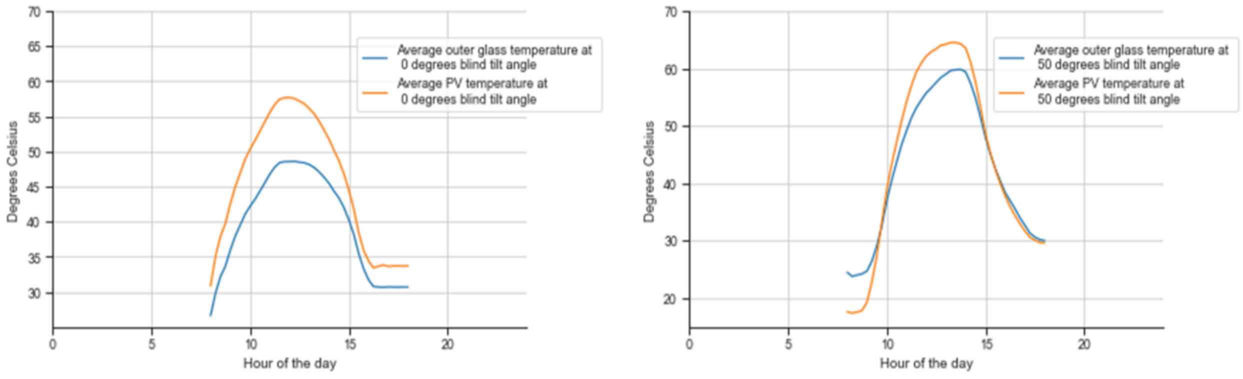

<u>Figure A-8.2:</u> *PV cell temperature and glass temperature throughout the day for a blind tilt angle of 0 degrees (left) and blind tilt angle of 50 degrees (right) under clear sky conditions.*

Another interesting temperature trend that appears in the experimental results is the evolution of the temperature throughout the room. From Figure A-8.3 and Figure A-8.4, it appears that the temperature decreases the further the distance is from the windows. This can be explained by the radiative heat loss from the windows that impact the space closest to them. Furthermore, the different room temperatures start decreasing around 2:00 – 3:00 PM compared to the window which start decreasing right after solar noon. Different cooling periods between the surfaces in the room and the window could explain this change in pattern. However, outside temperature still plays an important role in determining the indoor temperature. The same trends play out in both the clear and overcast conditions. For the overcast cases, the blind tilt angle data was collected on the 30th of April for the 0 degrees blind tilt angle, while the data for the 80 degrees blind tilt angle was collected on the 28th of April.

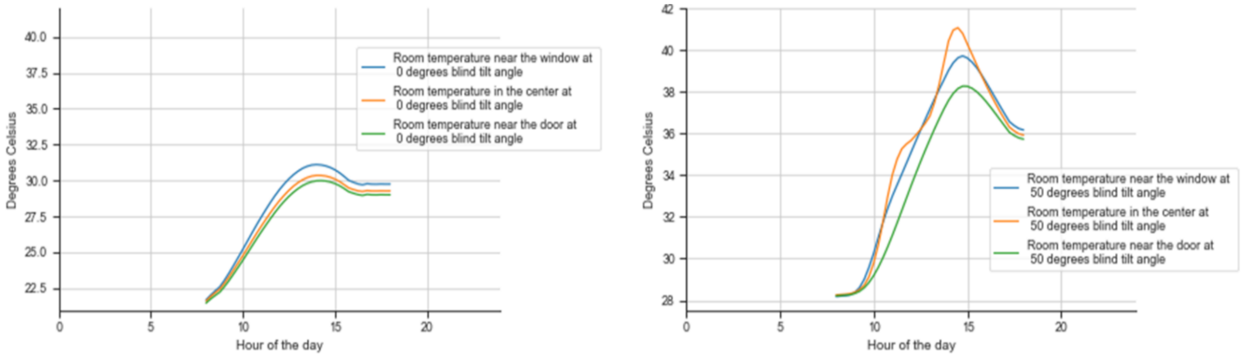

Figure A-8.3: *Room temperature at different points in the space throughout the day at a blind tilt angle of 0 degrees (left) and a blind tilt angle of 50 degrees (right) under clear conditions.*

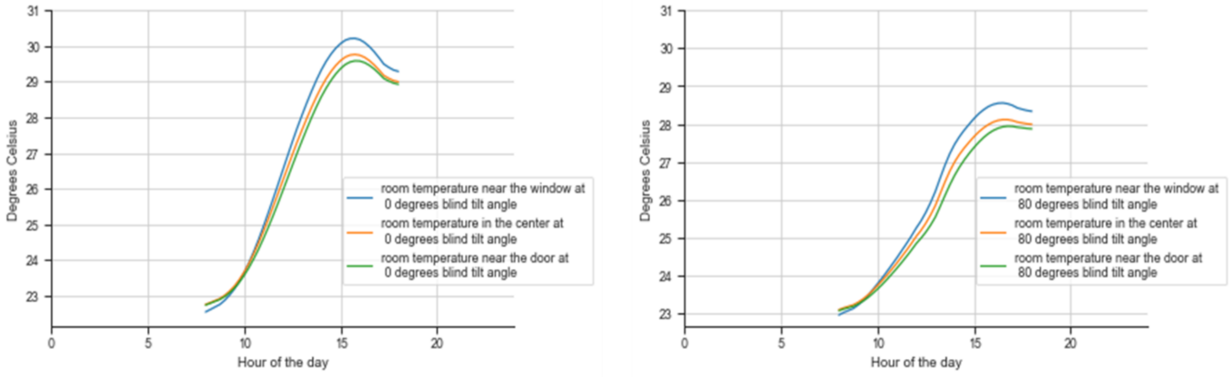

Figure A-8.4: *Room temperature at different points in the space throughout the day at a blind tilt angle of 0 degrees (left) and a blind tilt angle of 80 degrees (right) under cloudy conditions.*

Another interesting temperature trend that appears in the experimental results is the evolution of the temperature throughout the room. From the Figure A-8.5 and Figure A-8.6, it appears that the temperature decreases the further the distance is from the windows. This can be explained by the radiative heat loss from the windows that impact the space closest to them. Furthermore, the different room temperatures start decreasing around 2:00 – 3:00 PM compared to the window which start decreasing right after solar noon. Different cooling periods between the surfaces in the room and the window could explain this change in pattern. However, outside temperature still plays an important role in determining the indoor temperature. The same trends play out in both the clear and overcast conditions. For the overcast cases, the blind tilt angle data was collected on the 30th of April for the 0 degrees blind tilt angle, while the data for the 80 degrees blind tilt angle was collected on the 28th of April.

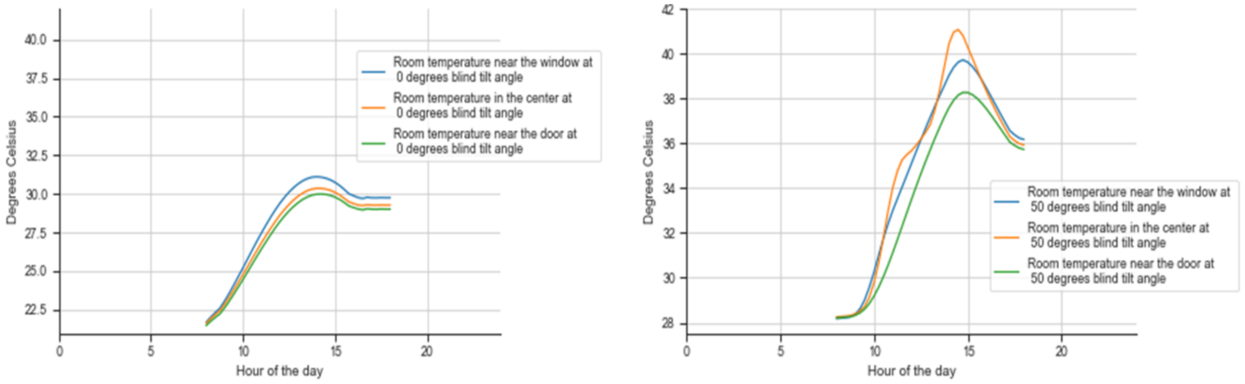

Figure A-8.5: *Room temperature at different points in the space throughout the day at a blind tilt angle of 0 degrees (left) and a blind tilt angle of 50 degrees (right) under clear conditions.*

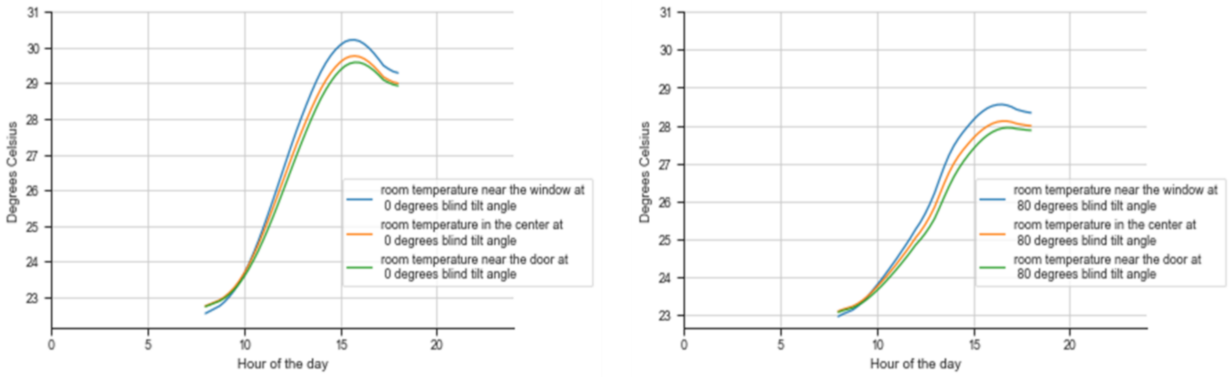

Figure A-8.6: *Room temperature at different points in the space throughout the day at a blind tilt angle of 0 degrees (left) and a blind tilt angle of 80 degrees (right) under cloudy conditions.*

Another interesting aspect that varies with blind tilt angle and outdoor conditions is the illuminance of different types. Figure A-8.7 shows the incident illuminance, transmitted illuminance, and the average room illuminance on different days and different tilt angles.

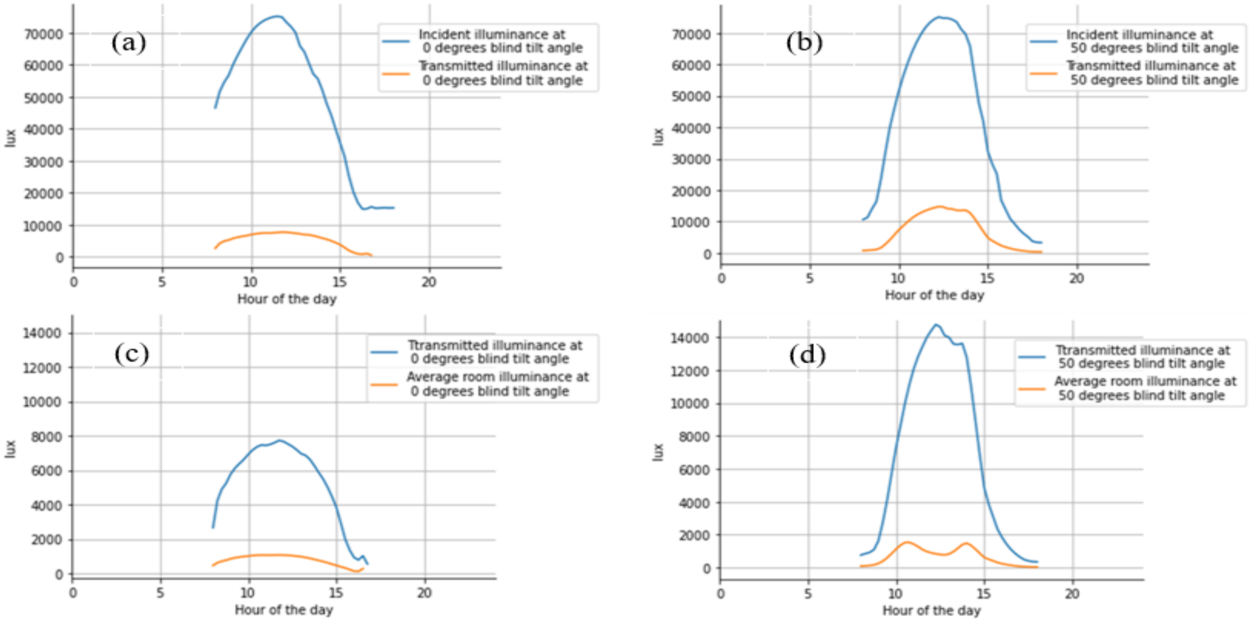

Figure A-8.7: *(a) Incident and transmitted daylight throughout that day at a 0 degrees blind tilt angle. (b) Incident and transmitted daylight throughout that day at a 50 degrees blind tilt angle. (c) Transmitted daylight and room illuminance throughout that day at*

The illuminances are separated into two graphs because of the significant difference between incident and room illuminances that makes the latter seem negligeable. With similar trends between cloudy and clear conditions, only the latter will be discussed to reduce repetitiveness. The incident daylight on the window for both days seem to be similar, with the maximum peaking at around 75 000 lux at the highest incidence angle at solar noon. However, this similarity does not translate to the transmitted daylight: Even though it follows a normal distribution in both cases, it does not reach the same maximum values. At $\beta = 0$, the maximum transmitted daylight is around 8000 lux. For $\beta = 50$, this value surpasses 14 000 lux. While one might expect that a horizontal blind angle would allow more light to pass through, this is not necessarily the case. The complex nature of the Advanced Fenestration System (AFS) and the interactions among its various components, such as shadowing effects, can significantly influence the transmitted illuminance in ways that are challenging to quantify. The blind tilt angle also has a significant impact on the different levels of illuminance within the indoor environment as seen in the below graphs.

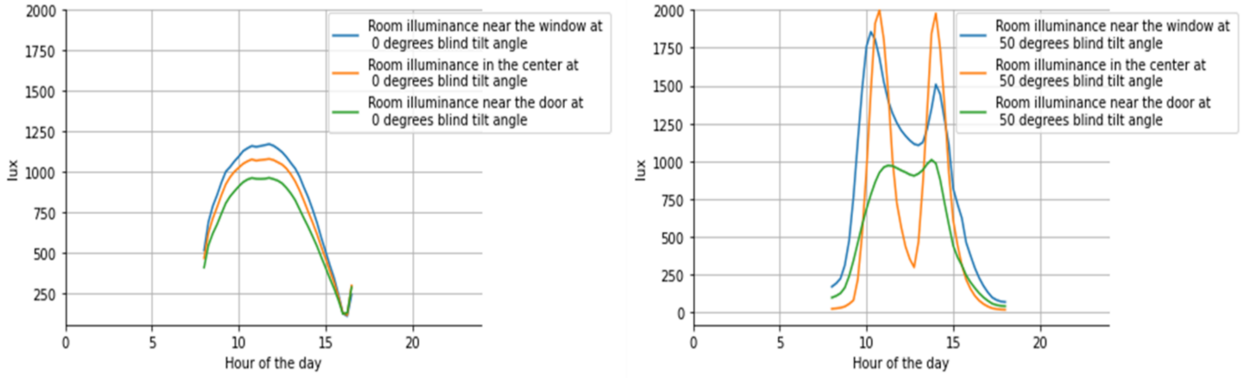

Figure A-8.8: *work plane illuminance at different points in the room at a blind tilt angle of 0 degrees (left) and blind tilt angle of 50 degrees (right).*

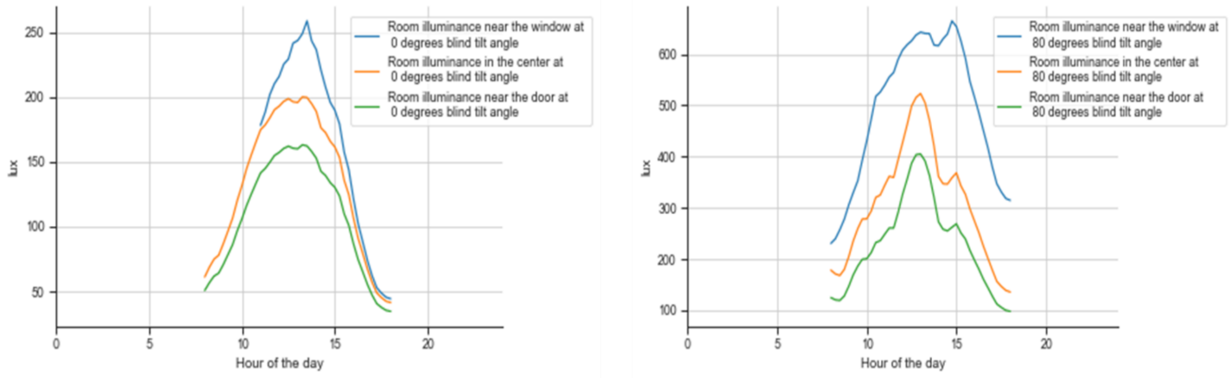

Figure A-8.9: *work plane illuminance at different points in the room at a blind tilt angle of 0 degrees (left) and blind tilt angle of 80 degrees (right) under cloudy conditions.*

At $\beta = 0$, the work plane illuminance in the room follows a normal distribution approximation where the closest point to the window has the highest illuminance. The difference in daylight levels at each point is negligeable at the beginning and end of day, but this difference peaks during the middle of the day, suggesting that the incidence angle of the sun is significant to determine the work plane illuminance during a sunny day: large θ leads to larger variations in the work plane illuminance compared to smaller θ. However, the work plane illuminance follows a bimodal distribution for a larger blind tilt angle. This is also the case for $\beta = 0$ on an overcast day. At $\beta = 50$, the work plane illuminance peaks at medium to high ranges of incidence angle ($25 < \theta < 40$) which can be caused by the shadowing effect and interreflections between the different elements of the advanced fenestration system. On average, the illuminance is higher near the window, but the highest value is reached at the center of the room, with an illuminance of 2000 lux. The irradiance also follows a similar pattern, with the larger blind tilt angles having the higher irradiance level transmitted through the window and on the work plane. At the same time, the indoor illuminance is always greater when considering a clear day compared to a sunny day, no matter the blind tilt angle.

Appendix B: Sun Position Calculations Code Sample

```
#constants needed for the calculation:
location_data = {
    "LAT": 45,  # Latitude of Montreal
    "LON": 73.6,  # Longitude of Montreal
    "LSM": 75,  # Local Standard Meridian of Montreal
    "psi": 0,  # The facade is facing South
    "beta_window": 90  # The windows are vertical
}

#Necessary functions:
def ET_f(n):
    '''Calculates equation of time'''
    return 9.87 * np.sin(4 * np.pi * (n - 81) / 364) - 7.53 * np.cos(2 *
np.pi * (n - 81) / 364) - 1.5 * np.sin(2 * np.pi * (n - 81) / 364 )

def AST_f(LST, ET, LSM, LON):
    '''Calculates apparent solar time'''
    return (LST * 60 + ET + 4 * (LSM - LON)) / 60

def h_f(AST):
    '''Calculates hour angle'''
    return (AST - 12) * 15

def delta_f(n):
    '''Calculates declination angle'''
    return 23.45 * np.sin(np.deg2rad(360 * (284 + n) / 365))

def alpha_f(L, delta, h):
    '''Calculates solar altitude'''
    return np.rad2deg(np.arcsin(np.cos(np.deg2rad(L)) *
np.cos(np.deg2rad(delta)) * np.cos(np.deg2rad(h)) + np.sin(np.deg2rad(L)) *
np.sin(np.deg2rad(delta))))

def phi_f(alpha, L, delta, h):
    '''Calculates solar azimuth'''
    h = np.array(h)
    result = np.zeros(h.shape)
    result[h!=0] = np.arccos((np.sin(np.deg2rad(alpha[h!=0])) *
np.sin(np.deg2rad(L)) - np.sin(np.deg2rad(delta))) /
(np.cos(np.deg2rad(alpha[h!=0])) * np.cos(np.deg2rad(L))))* np.sign(h[h!=0])
    return result

def gamma_f(phi, psi):
    '''Calculates surface solar azimuth'''
    return phi - psi

def theta_f(alpha, gamma, beta):
    '''Calculates incidence angle'''
```

```
    return np.clip(np.rad2deg(np.arccos(np.cos(np.deg2rad(alpha)) *
np.cos(np.absolute(np.deg2rad(gamma))) * np.sin(np.deg2rad(beta)) +
np.sin(np.deg2rad(alpha)) * np.cos(np.deg2rad(beta)))), 0, 90)

def d_f(alpha, phi):
    return (np.degrees(np.arctan(np.tan(np.deg2rad(alpha)) /
np.deg2rad(np.deg2rad(phi)))))

#Incidence angle calculation:

def theta_calculation():
    for i in range(len(weather_data)):
        weather_data['ET'][i] = ET_f(weather_data['n'][i])
        weather_data['AST'][i] = AST_f(weather_data['decimal
hour'][i],weather_data['ET'][i],location_data['LSM'],location_data['LON'])
        weather_data['h'][i] = h_f(weather_data['AST'][i])
        weather_data['delta'][i] = delta_f(weather_data['n'][i])
        weather_data['alpha'][i] =
alpha_f(location_data['LAT'],weather_data['delta'][i],weather_data['h'][i])
        weather_data['phi'][i] =
phi_f(weather_data['alpha'][i],location_data['LAT'],weather_data['delta'][i],
weather_data['h'][i])
        weather_data['gamma'][i] =
gamma_f(weather_data['phi'][i],location_data['psi'])
        weather_data['d'][i] = d_f(weather_data['alpha'][i] ,
weather_data['phi'][i])
        weather_data['theta'][i] =
theta_f(weather_data['alpha'][i],weather_data['gamma'][i],location_data['beta
_window'])
    return(weather_data)
```

Appendix C: View Factor & Configuration Factor Calculations

```
# COMPUTE VIEW FACTORS BETWEEN PARALLEL SURFACES WITH SAME AREA DIRECTLY
FACING EACH OTHER IMAGE 1.1
def F_pl(a,b,c):
    # INTERIM VARIABLES
    X, Y = a/c, b/c
    A = np.sqrt(1 + X ** 2)
    B = np.sqrt(1 + Y ** 2)
    # CALCULATION
    F = np.log(A*B/np.sqrt(1 + X**2 + Y**2))
    F += B * X * np.arctan(X/B)
    F += A * Y * np.arctan(Y/A)
    F -= X * np.arctan(X)
    F -= Y * np.arctan(Y)
    F *= 2/(np. pi * X * Y)
    return F

# COMPUTE VIEW FACTOR BETWEEN PERPENDICULAR SURFACES WITH WITH A SHARED EDGE
(l) IMAGE 1.2
def F_pp(w,h,l):
    # INTERIM VARIABLES
    W = w / l
    H = h / l
    A = 1 + H ** 2
    B = 1 + W ** 2
    C = H ** 2 + W ** 2
    # CALCULATION
    F = W * np.arctan(1/W)
    F += H * np.arctan(1/H)
    F -= np.sqrt(C) * np.arctan(1 / np.sqrt(C))
    F += 0.25 * np.log((A * B / (C+1)) * ((W**2*(C+1)/B/C)**(W**2) *
((H**2*(C+1)/A/C)**(H**2))))
    F *= 1/(W*np.pi)

    return F

# COMPUTE VIEW FACTOR BETWEEN TWO FINITE RECTANGLES PERPENDICULAR TO EACH
OTHER IMAGE 1.3
def Fg_pp(x1, x2, y1, y2, xi1, xi2, eta1, eta2):
    # MESH GRID GENERATION FOR ALL COMBINATIONS OF x, y, xi, and eta
    grid = np.stack(np.meshgrid([x1, x2], [xi1, xi2], [y1, y2], [eta1,
eta2]), -1).reshape(-1, 4)
    ix  = np.stack(np.meshgrid([0, 1],[0, 1], [0, 1],[0, 1]), -1).reshape(-1,
4)
    # INTERIM VARIABLES
    A = grid[:,0] - grid[:,1]
    B = grid[:,2] - grid[:,3]
    C = grid[:,0]**2 + grid[:,1]**2
    D = np.sqrt(C)
    # CALCULATION
```

```
    E = B* (D*np.arctan(B/D)) - 0.25 * (C - B**2) * np.log(C + B**2)
    E *= (-1)**ix.sum(axis=1)/(2*np.pi)
    E /=(x2-x1)*(y2-y1)
    F = E.sum()

    return F

# COMPUTE VIEW FACTOR BETWEEN TWO FINITE RECTANGLES PARALLEL TO EACH OTHER
IMAGE 1.4
def Fg_pl(x1, x2, y1, y2, xi1, xi2, eta1, eta2, z):
    # MESH GRID GENERATION FOR ALL COMBINATIONS OF x, y, xi, and eta
    grid = np.stack(np.meshgrid([x1, x2], [xi1, xi2], [y1, y2], [eta1,
eta2]), -1).reshape(-1, 4)
    ix  = np.stack(np.meshgrid([0, 1],[0, 1], [0, 1],[0, 1]), -1).reshape(-1,
4)
    # INTERIM VARIABLES
    A = grid[:,0] - grid[:,1]  # x_i - xi_l
    B = grid[:,2] - grid[:,3]  # y_j - eta_k
    C = np.sqrt(A**2+z**2)
    D = np.sqrt(B**2+z**2)
     # CALCULATION
    E = B*C*np.arctan(B/C) + A*D*np.arctan(A/D) -
0.5*z**2*np.log(A**2+B**2+z**2)
    E *= (-1)**ix.sum(axis=1)/(2*np.pi)
    E /=(x2-x1)*(y2-y1)
    F = E.sum()
    return F

# ANALYTICAL SOLUTION OF C-FACTOR BETWEEN A POINT FACING UP AND PERPENDICULAR
FACE TOWARDS THE POINT
def f_1(x,y,z):
    A = np.sqrt(y**2 + z **2)
    f = np.arctan(x/(z+1e-10))
    f -= z/A*np.arctan(x/A)
    f *= 1/(2*np.pi)

    return f

# ANALYTICAL SOLUTION OF C-FACTOR BETWEEN A POINT AND PERPENDICULAR SURFACE
FACING DIRECTLY EACH OTHER (only for ceiling)
def f_2(x,y,z):
    A = np.sqrt(y**2 + z**2)
    B = np.sqrt(x**2 + z**2)
    f = y/A*np.arctan(x/A)
    f += x/B*np.arctan(y/B)
    f *= 1/(2*np.pi)
    return f


def calculate_factors():
    rl = 3.402 #room length
    rw = 3.050 #room width
    rh = 3.048 #room height
```

```
    wl = 0.986 #window length
    wh = 1.954 #window height
    wbh = 0.547 #distance between floor and window bottom

    area = np.zeros(10)
    area[[0,1,2]] = wl * wh
    area[3] = (rw*rh) - (area[0] + area[1] + area[2])
    area[[4,7]] = rw*rl
    area[[5,6]] = rl*rh
    area[[8,9]] = rw*rh

    #view factor
    F = np.zeros([10,10])

F[[0,0,0,0,0,1,1,1,1,1,2,2,2,2,2,3,3,3,3,3,9,9,9,9,9],[0,1,2,3,9,0,1,2,3,9,0,
1,2,3,9,0,1,2,3,9,0,1,2,3,9]] = 0
    #floor
    F[4,0] = Fg_pp(0,rl,0,rw,wbh,wh+wbh,rw-wl,rw)
    F[0,4] = (area[4]/area[0])*F[4,0]
    F[4,1] = Fg_pp(0,rl,0,rw,wbh,wh+wbh,wl+0.046,wl+0.046+wl)
    F[1,4] = (area[4]/area[1])*F[4,1]
    F[4,2] = Fg_pp(0,rl,0,rw,wbh,wh+wbh,0,wl)
    F[2,4] = (area[4]/area[2])*F[4,2]
    F[[4,4],[8,9]] = F_pp(rl,rh,rw)
    F[9,4] = (area[4]/area[9])*F[4,9]
    F[8,4] = (area[4]/area[8])*F[4,8]
    F[4,3] = F[4,9] - (F[4,0] + F[4,1] + F[4,2])
    F[3,4] = (area[4]/area[3])*F[4,3]
    F[[4,4],[5,6]] = F_pp(rw,rh,rl)
    F[5,4] = (area[4]/area[5])*F[4,5]
    F[6,4] = (area[4]/area[6])*F[4,6]
    F[[4,7],[7,4]] = F_pl(rw,rl,rh)
    #ceiling
    F[7,0] = Fg_pp(0,rl,0,rw,wbh,wh+wbh,rw-wl,rw)
    F[0,7] = (area[7]/area[0])*F[7,0]
    F[7,1] = Fg_pp(0,rl,0,rw,wbh,wh+wbh,wl+0.046,wl+0.046+wl)
    F[1,7] = (area[7]/area[1])*F[7,1]
    F[7,2] = Fg_pp(0,rl,0,rw,wbh,wh+wbh,0,wl)
    F[2,7] = (area[7]/area[2])*F[7,2]
    F[[7,7],[8,9]] = F_pp(rl,rh,rw)
    F[9,7] = (area[7]/area[9])*F[7,9]
    F[8,7] = (area[7]/area[8])*F[7,8]
    F[7,3] = F[7,9] - (F[7,0] + F[7,1] + F[7,2])
    F[3,7] = (area[7]/area[3])*F[7,3]
    F[[7,7],[5,6]] = F_pp(rw,rh,rl)
    F[5,7] = (area[7]/area[5])*F[7,5]
    F[6,7] = (area[7]/area[6])*F[7,6]
    #North Wall
    F[8,0] = Fg_pl(0,rw,0,rh,0,wl,wbh,wbh+wh,rl)
    F[0,8] = (area[8]/area[0])*F[8,0]
    F[8,1] = Fg_pl(0,rw,0,rh,wl+0.046,wl+0.046+wl,wbh,wbh+wh,rl)
    F[1,8] = (area[8]/area[1])*F[8,1]
    F[8,2] = Fg_pl(0,rw,0,rh,wl+wl+0.046+0.046,rw,wbh,wbh+wh,rl)
```

```
    F[2,8] = (area[8]/area[2])*F[8,2]
    F[[8,9],[9,8]] = F_pl(rw,rh,rl)
    F[8,3] = F[8,9] - (F[8,0] + F[8,1] + F[8,2])
    F[3,8] = (area[8]/area[3])*F[8,3]
    F[[8,8],[5,6]] = F_pp(rw,rl,rh)
    F[5,8] = (area[8]/area[5])*F[8,5]
    F[6,8] = (area[8]/area[6])*F[8,6]
    #West Wall
    F[[5,6],[6,5]] = F_pl(rh,rl,rw)
    F[6,0] = Fg_pp(0,rl,0,rh,0,wl,wbh,wbh+wh) #
    F[0,6] = (area[6]/area[0])*F[6,0]
    F[6,1] = Fg_pp(0,rl,0,rh,wl+0.046,wl+0.046+wl,wbh,wbh+wh)
    F[1,6] = (area[6]/area[1])*F[6,1]
    F[6,2] = Fg_pp(0,rl,0,rh,wl+0.046+wl+0.046,rw,wbh,wbh+wh)
    F[2,6] = (area[6]/area[2])*F[6,2]
    F[[6,9,5,9],[9,6,9,5]] = F_pp(rl,rw,rh)
    F[6,3] = F[6,9] - (F[6,0] + F[6,1] + F[6,2])
    F[3,6] = (area[6]/area[3])*F[6,3]
    #East Wall
    F[5,0] = Fg_pp(0,rl,0,rh,rw-wl,rw,wbh,wh+wbh)
    F[0,5] = (area[5]/area[0])*F[5,0]
    F[5,1] = Fg_pp(0,rl,0,rh,wl+0.046,wl+0.046+wl,wbh,wbh+wh)
    F[1,5] = (area[5]/area[1])*F[5,1]
    F[5,2] = Fg_pp(0,rl,0,rh,0,wl,wbh,wbh+wh)
    F[2,5] = (area[5]/area[2])*F[5,2]
    F[5,3] = F[5,9] - (F[5,0] + F[5,1] + F[5,2])
    F[3,5] = (area[5]/area[3])*F[5,3]

    #Exclude the south wall (surface 10)
    F = F[:9,:9]

    #configuration factor
    f = np.zeros(10)
    f[4] = 2 * f_2(rw/2 , rl/2 , rh-0.8)
    f[5] = 0 #the east wall is behind eyesight, so it does not contribute
    f[6] = 2 * f_1(rh-0.8 , rl/2 , rw/2) + 2 * f_1(0.8 , rl/2, rw/2)
    f[7] = 2 * f_2(rw/2 , rl/2 , rh-0.8)
    f[8] = f_1(rh-0.8 , rw/2 , rl/2) + f_1(0.8 , rw/2 , rl/2)
    f[9] = f_1(rh-0.8 , rw/2 , rl/2) + f_1(0.8 , rw/2 , rl/2)
    f[1] = f_1(rw-(wbh+wbh+(0.8-wbh)) , wl/2 , rl/2) + f_1(0.8-wbh , wl/2 ,
rl/2)
    f[0] = (f_1(rw-(wbh+wbh+(0.8-wbh)) , rw/2 , rl/2) - f_1(rw-(wbh+wbh+(0.8-
wbh)) , (wl/2)+0.046 , rl/2))
    + (f_1(0.8-wbh , rw/2 , rl/2) - f_1(0.8-wbh , (wl/2)+0.046 , rl/2))
    f[2] = 0
    f[3] = f[9] - (f[0] + f[1] + f[2])
    f = f[:9]
    return(F, f)
F, f = calculate_factors()
```

Appendix D: Incident and Transmitted Daylight Calculations

```
def outer_transmittance_f(theta):
    # Calculate the transmittance of the PV layer
    refractive_index_glass = 1.51
    refractive_index_silicon = 3.88
    thickness = 0.006 #in meters
    k_glass = 6.96
    k_silicon = 0.019
    theta_prime_glass = np.rad2deg(np.arcsin(np.sin(np.deg2rad(theta)) /
refractive_index_glass))
    theta_prime_silicon = np.rad2deg(np.arcsin(np.sin(np.deg2rad(theta)) /
refractive_index_silicon))
    reflectivity_glass = (((np.sin(np.deg2rad(theta - theta_prime_glass))) /
(np.sin(np.deg2rad(theta + theta_prime_glass))))**2
                          + ((np.tan(np.deg2rad(theta - theta_prime_glass)))
/ (np.tan(np.deg2rad(theta + theta_prime_glass))))**2)* 0.5
    reflectivity_silicon = (((np.sin(np.deg2rad(theta -
theta_prime_silicon))) / (np.sin(np.deg2rad(theta +
theta_prime_silicon))))**2
                        + ((np.tan(np.deg2rad(theta - theta_prime_silicon)))
/ (np.tan(np.deg2rad(theta + theta_prime_silicon))))**2)* 0.5
    thickness_prime_glass = thickness / ((1 - ((np.sin(np.deg2rad(theta) /
theta_prime_glass))**2))**0.5)
    thickness_prime_silicon = thickness / ((1 - ((np.sin(np.deg2rad(theta) /
theta_prime_silicon)**2)))**0.5)
    a_glass = np.exp(-1 * k_glass * thickness_prime_glass)
    a_silicon = np.exp(-1 * k_silicon * thickness_prime_silicon)
    transmittance_glass = (((1 - reflectivity_glass)**2) * a_glass) / (1 -
(a_glass**2 * reflectivity_glass**2))
    transmittance_silicon = (((1 - reflectivity_silicon)**2) * a_silicon) /
(1 - (a_silicon**2 * reflectivity_silicon**2))
    return (0.4591 * transmittance_silicon + 0.54 * transmittance_glass)

def middle_transmittance_f(theta):
    # Calculate the transmittance of the middle window
    refractive_index_glass = 1.51
    thickness = 0.006 #in meters
    k_glass = 6.96
    theta_prime_glass = np.rad2deg(np.arcsin(np.sin(np.deg2rad(theta)) /
refractive_index_glass))
    reflectivity_glass = (((np.sin(np.deg2rad(theta - theta_prime_glass))) /
(np.sin(np.deg2rad(theta + theta_prime_glass))))**2
                            + ((np.tan(np.deg2rad(theta -
theta_prime_glass))) / (np.tan(np.deg2rad(theta + theta_prime_glass))))**2)*
0.5
    thickness_prime_glass = thickness / ((1 - ((np.sin(np.deg2rad(theta) /
theta_prime_glass))**2))**0.5)
    a_glass = np.exp(-1 * k_glass * thickness_prime_glass)
    transmittance_glass = (((1 - reflectivity_glass)**2) * a_glass) / (1 -
(a_glass**2 * reflectivity_glass**2))
```

```
    return (transmittance_glass**3)

def clear_transmitted_daylight_f(clear_transmittance , alpha , n , theta ,
outer_transmittance):
    # Calculate incident and transmitted daylight through the two glazings
for a clear sky
    E_zero = 133800 #lux: average illuminance on a surface perpendicular to
the sun's rays
    extinction_coefficient = 0.21 #value for a clear day
    f_wg = 0.5 #view factor between the ground and the window
    f_wsky = 0.5 #view factor between the sky and the window
    ground_reflectance = 0.5 #reflectance of the ground
    E_hor_sky = 800 + 15500 * math.sin(np.deg2rad(theta))**0.5 #horizontal
illuminance due to the sky
    correction_factor = 1 + 0.033 * math.cos(360 * n / 365) #accounting for
elliptical shape of the orbit of the earth
    relative_air_mass = 1 / math.sin(np.deg2rad(theta)) #relative optical air
mass
    E_sol_hor = E_zero * correction_factor * math.exp((-1 *
extinction_coefficient) * relative_air_mass) * math.sin(np.deg2rad(alpha))
#solar horizontal illuminance
    E_total_hor = E_hor_sky + E_sol_hor #total horizontal illuminance
    E_wg = f_wg * ground_reflectance * E_total_hor #daylight incident on the
window from the ground
    E_wsky = f_wsky * E_hor_sky #daylight incident on the window from the sky
    E_wsun = E_zero * correction_factor * math.exp((-1 *
extinction_coefficient) * relative_air_mass) * math.cos(np.deg2rad(theta))
#daylight incident on the window from the sun
    E_total_incident = E_wg + E_wsky + E_wsun #total incident daylight on the
window
    return (E_total_incident * clear_transmittance * outer_transmittance)

def middle_clear_transmitted_daylight_f(middle_transmittance , alpha , n ,
theta):
    # Calculate incident and transmitted daylight through the middle window
on a clear sky
    E_zero = 133800 #lux: average illuminance on a surface perpendicular to
the sun's rays
    extinction_coefficient = 0.21 #value for a clear day
    f_wg = 0.5 #view factor between the ground and the window
    f_wsky = 0.5 #view factor between the sky and the window
    ground_reflectance = 0.5 #reflectance of the ground
    E_hor_sky = 800 + 15500 * math.sin(np.deg2rad(theta))**0.5 #horizontal
illuminance due to the sky
    correction_factor = 1 + 0.033 * math.cos(360 * n / 365) #accounting for
elliptical shape of the orbit of the earth
    relative_air_mass = 1 / math.sin(np.deg2rad(theta)) #relative optical air
mass
    E_sol_hor = E_zero * correction_factor * math.exp((-1 *
extinction_coefficient) * relative_air_mass) * math.sin(np.deg2rad(alpha))
#solar horizontal illuminance
    E_total_hor = E_hor_sky + E_sol_hor #total horizontal illuminance
```

```
    E_wg = f_wg * ground_reflectance * E_total_hor #daylight incident on the
window from the ground
    E_wsky = f_wsky * E_hor_sky #daylight incident on the window from the sky
    E_wsun = E_zero * correction_factor * math.exp((-1 *
extinction_coefficient) * relative_air_mass) * math.cos(np.deg2rad(theta))
#daylight incident on the window from the sun
    E_total_incident = E_wg + E_wsky + E_wsun #total incident daylight on the
window
    return (E_total_incident * middle_transmittance)

def cloudy_transmitted_daylight_f(alpha , cloudy_transmittance ,
optimal_tilt_angle_cloudy , outer_transmittance):
    # Calculate incident and transmitted daylight through the two glazings
for a cloudy sky
    ground_reflectance = 0.4 #reflectance of concrete / cement
    incident_daylight = 500 * (0.3 + (21 * np.sin(np.deg2rad(alpha)))) * (1 +
ground_reflectance)
    return (incident_daylight * cloudy_transmittance * outer_transmittance)

def middle_cloudy_transmitted_daylight_f(alpha , middle_transmittance):
    # Calculate incident and transmitted daylight through the middle window
on a cloudy sky
    ground_reflectance = 0.4 #reflectance of concrete / cement
    incident_daylight = 500 * (0.3 + (21 * np.sin(np.deg2rad(alpha)))) * (1 +
ground_reflectance)
    return (incident_daylight * middle_transmittance)


def cal_M(M0, F, rho):
    # Calculate the final luminous exitance matrix
    # INVERSE MATRIX OF  I - (rho x F)
    A = np.linalg.inv(np.eye(9) - np.multiply(F, rho))
    # FINAL LUMINOUS EXITANCE AFTER INTER-REFLECTION
    M = np.matmul(A, M0)
    return M
```

Appendix E: Control Strategy Sample Code

```
def main():
    for i in range(len(weather_data)):
        final_data['outer_transmittance'][i] =
outer_transmittance_f(weather_data['theta'][i])
        final_data['middle_transmittance'][i] =
middle_transmittance_f(weather_data['theta'][i])
        # Sunny time step
        if weather_data['cloud_cover'][i] <= 4:
            # Calculate daylight transmitted by the middle window
            final_data['middle_transmitted_daylight'][i] =
middle_clear_transmitted_daylight_f(final_data['middle_transmittance'][i],

weather_data['alpha'][i] , weather_data['n'][i],

weather_data['theta'][i])*control_constants['blackout_shade_transmittance']
            # During occupied hours
            if 9 <= weather_data['decimal hour'][i] < 12 or 14 <
weather_data['decimal hour'][i] <= 17:
                # Profile angle calculation and choice of the optimal tilt
angle
                if weather_data['d'][i] > 45:
                    final_data['optimal_tilt_angle'][i] = 0
                    final_data['transmittance'][i] =
((1/((2.32*10**13)*(np.sqrt(2.506628)))) * (np.exp((-
0.5)*((final_data['optimal_tilt_angle'][i] -
(2.38*10**13))/(2.32*10**13))**2))) * ((-
2.91*10**7)*weather_data['theta'][i]**3 +
(6.39*10**9)*weather_data['theta'][i]**2 + (-
6.63*10**9)*weather_data['theta'][i]  + (-1.73*10**11))
                    final_data['transmitted_daylight'][i] =
clear_transmitted_daylight_f(final_data['transmittance'][i],
weather_data['alpha'][i] ,  weather_data['n'][i] ,  weather_data['theta'][i]
, final_data['outer_transmittance'][i])
                    final_data['total_transmitted_daylight'][i] =
final_data['middle_transmitted_daylight'][i] +
final_data['transmitted_daylight'][i]
                    M0 = np.zeros([9,1])
                    for b in range(8):
                        if b == 0:
                            M0[b] = final_data['transmitted_daylight'][i]
                        elif b == 1:
                            M0[b] =
final_data['middle_transmitted_daylight'][i]
                        elif b == 2:
                            M0[b] = final_data['transmitted_daylight'][i]
                        else:
                            M0[b] = 0
                    M = cal_M(M0 , F, control_constants['rho'])
                    # Work plane illuminance calculation
```

```
                    final_data['Ep'][i] = f[0]*M[0] + f[1]*M[1] + f[2]*M[2] +
f[3]*M[3] + f[4]*M[4] + f[5]*M[5] + f[6]*M[6] + f[7]*M[7] + f[8]*M[8]
                    # DGPs calculation
                    temp_E_ceiling =  F[7][0]*M[0] + F[7][1]*M[1] +
F[7][2]*M[2] + F[7][3]*M[3] + F[7][4]*M[4] + F[7][5]*M[5]
                    + F[7][6]*M[6] + F[7][7]*M[7] + F[7][8]*M[8]
                    temp_E_floor = F[4][0]*M[0] + F[4][1]*M[1] + F[4][2]*M[2]
+ F[4][3]*M[3] + F[4][4]*M[4] + F[4][5]*M[5]
                    + F[4][6]*M[6] + F[4][7]*M[7] + F[4][8]*M[8]
                    temp_E_westwall = F[6][0]*M[0] + F[6][1]*M[1] +
F[6][2]*M[2] + F[6][3]*M[3] + F[6][4]*M[4] + F[6][5]*M[5]
                    + F[6][6]*M[6] + F[6][7]*M[7] + F[6][8]*M[8]
                    temp_E_northwall = F[8][0]*M[0] + F[8][1]*M[1] +
F[8][2]*M[2] + F[8][3]*M[3] + F[8][4]*M[4] + F[8][5]*M[5]
                    + F[8][6]*M[6] + F[8][7]*M[7] + F[8][8]*M[8]
                    temp_E_window1 = F[0][0]*M[0] + F[0][1]*M[1] +
F[0][2]*M[2] + F[0][3]*M[3] + F[0][4]*M[4] + F[0][5]*M[5]
                    + F[0][6]*M[6] + F[0][7]*M[7] + F[0][8]*M[8]
                    temp_E_window2 = F[1][0]*M[0] + F[1][1]*M[1] +
F[1][2]*M[2] + F[1][3]*M[3] + F[1][4]*M[4] + F[1][5]*M[5]
                    + F[1][6]*M[6] + F[1][7]*M[7] + F[1][8]*M[8]
                    temp_E_southwall = F[3][0]*M[0] + F[3][1]*M[1] +
F[3][2]*M[2] + F[3][3]*M[3] + F[3][4]*M[4] + F[3][5]*M[5]
                    + F[3][6]*M[6] + F[3][7]*M[7] + F[3][8]*M[8]
                    final_data['Ev'][i] = (temp_E_ceiling / 2) +
(temp_E_floor / 2) + (temp_E_westwall) + (temp_E_northwall / 2) +
(temp_E_window1) + (temp_E_window2 / 2) + (temp_E_southwall / 2)
                    final_data['DGPs'][i] = float(6.22*10**-5 *
final_data['Ev'][i] + 0.184)
                elif weather_data['d'][i] <= 45:
                    # Hyperparameter optimization
                    # intermediate arrays creation
                    temp_transmittance =
np.zeros(len(control_constants['blind_tilt_angle']))
                    temp_transmitted_daylight =
np.zeros(len(control_constants['blind_tilt_angle']))
                    temp_Ev =
np.zeros(len(control_constants['blind_tilt_angle']))
                    temp_Ep =
np.zeros(len(control_constants['blind_tilt_angle']))
                    temp_DGPs =
np.zeros(len(control_constants['blind_tilt_angle']))
                    temp_total_transmitted_daylight =
np.zeros(len(control_constants['blind_tilt_angle']))
                    for idx, tilt in
enumerate(control_constants['blind_tilt_angle']):
                        if 0 <= tilt <= 45:
                            temp_transmittance[idx] =
((1/((2.32*10**13)*(np.sqrt(2.506628)))) * (np.exp((-0.5)*((tilt -
(2.38*10**13))/(2.32*10**13))**2))) * ((-
2.91*10**7)*weather_data['theta'][i]**3 +
(6.39*10**9)*weather_data['theta'][i]**2 + (-
6.63*10**9)*weather_data['theta'][i]  + (-1.73*10**11))
```

```
                        elif 45 < tilt <= 85:
                            temp_transmittance[idx] =
np.maximum((((0.931)*((1 / ((2.95*10**8) * np.sqrt(2.506628))) * np.exp(-0.5
* ((tilt - (1.65*10**9)) / (2.95*10**8))**2))) + \
                                                                ((1-
0.931)*((1 / ((2.19*10**8) * np.sqrt(2.506628))) * np.exp(-0.5 * ((tilt -
(7.28*10**8)) / (2.19*10**8))**2)))) * \
                                                                ((-
6.57*10**7) * weather_data['theta'][i]**3 + (4.19*10**9) *
weather_data['theta'][i]**2 + (-6.36*10**10) * weather_data['theta'][i] +
(1.85*10**11)),0)
                        elif tilt == 90:
                            temp_transmittance[idx] = 0
                        temp_transmitted_daylight[idx] =
clear_transmitted_daylight_f(temp_transmittance[idx],
weather_data['alpha'][i] ,  weather_data['n'][i] ,  weather_data['theta'][i]
, final_data['outer_transmittance'][i])
                        temp_total_transmitted_daylight[idx] =
temp_transmitted_daylight[idx] + final_data['middle_transmitted_daylight'][i]
                        #radiosity matrix
                        M0 = np.zeros([9 ,
len(control_constants['blind_tilt_angle'])])
                        for m in range
(len(control_constants['blind_tilt_angle'])):
                            for l in range(9):
                                if l == 0:
                                    M0[l][m] = temp_transmitted_daylight[m]
                                elif l == 1:
                                    M0[l][m] =
final_data['middle_transmitted_daylight'][i]
                                elif l == 2:
                                    M0[l][m] = temp_transmitted_daylight[m]
                                else:
                                    M0[l][m] = 0
                        M = cal_M(M0 , F, control_constants['rho'])
                        for k in range(len(M[0])):
                            temp_Ep[k]  = f[0]*M[0][k] + f[1]*M[1][k] +
f[2]*M[2][k] + f[3]*M[3][k] + f[4]*M[4][k] + f[5]*M[5][k] + f[6]*M[6][k] +
f[7]*M[7][k] + f[8]*M[8][k]
                            temp_E_ceiling =  F[7][0]*M[0][k] +
F[7][1]*M[1][k] + F[7][2]*M[2][k] + F[7][3]*M[3][k] + F[7][4]*M[4][k] +
F[7][5]*M[5][k]
                            + F[7][6]*M[6][k] + F[7][7]*M[7][k] +
F[7][8]*M[8][k]
                            temp_E_floor = F[4][0]*M[0][k] + F[4][1]*M[1][k]
+ F[4][2]*M[2][k] + F[4][3]*M[3][k] + F[4][4]*M[4][k] + F[4][5]*M[5][k]
                            + F[4][6]*M[6][k] + F[4][7]*M[7][k] +
F[4][8]*M[8][k]
                            temp_E_westwall = F[6][0]*M[0][k] +
F[6][1]*M[1][k] + F[6][2]*M[2][k] + F[6][3]*M[3][k] + F[6][4]*M[4][k] +
F[6][5]*M[5][k]
                            + F[6][6]*M[6][k] + F[6][7]*M[7][k] +
F[6][8]*M[8][k]
```

```
                            temp_E_northwall = F[8][0]*M[0][k] +
F[8][1]*M[1][k] + F[8][2]*M[2][k] + F[8][3]*M[3][k] + F[8][4]*M[4][k] +
F[8][5]*M[5][k]
                            + F[8][6]*M[6][k] + F[8][7]*M[7][k] +
F[8][8]*M[8][k]
                            temp_E_window1 = F[0][0]*M[0][k] +
F[0][1]*M[1][k] + F[0][2]*M[2][k] + F[0][3]*M[3][k] + F[0][4]*M[4][k] +
F[0][5]*M[5][k]
                            + F[0][6]*M[6][k] + F[0][7]*M[7][k] +
F[0][8]*M[8][k]
                            temp_E_window2 = F[1][0]*M[0][k] +
F[1][1]*M[1][k] + F[1][2]*M[2][k] + F[1][3]*M[3][k] + F[1][4]*M[4][k] +
F[1][5]*M[5][k]
                            + F[1][6]*M[6][k] + F[1][7]*M[7][k] +
F[1][8]*M[8][k]
                            temp_E_southwall = F[3][0]*M[0][k] +
F[3][1]*M[1][k] + F[3][2]*M[2][k] + F[3][3]*M[3][k] + F[3][4]*M[4][k] +
F[3][5]*M[5][k]
                            + F[3][6]*M[6][k] + F[3][7]*M[7][k] +
F[3][8]*M[8][k]
                            temp_Ev[k] = (temp_E_ceiling / 2) + (temp_E_floor
/ 2) + (temp_E_westwall/2) + (temp_E_northwall / 2) + (temp_E_window1/2) +
(temp_E_window2 / 2) + (temp_E_southwall / 2)
                            temp_DGPs[k] = float(6.22*10**-5 * temp_Ev[k] +
0.184)
                    mask = (temp_DGPs < 0.35)
                    # Apply the mask to temp_Ep to filter values
                    filtered_temp_Ep = temp_Ep[mask]
                    # Find the index of the maximum value in the
filtered_temp_Ep
                    max_value_index = np.argmax(filtered_temp_Ep)
                    # Now find the corresponding index in the original array
(temp_Ep)
                    original_index = np.where(temp_Ep ==
filtered_temp_Ep[max_value_index])[0][0]
                    # Assign the max value to the final_data using the
original index
                    final_data['Ep'][i] = temp_Ep[original_index]
                    final_data['DGPs'][i] = temp_DGPs[original_index]
                    final_data['transmittance'][i] =
temp_transmittance[original_index]
                    final_data['transmitted_daylight'][i] =
temp_transmitted_daylight[original_index]
                    final_data['total_transmitted_daylight'][i] =
temp_total_transmitted_daylight[original_index]
                    final_data['optimal_tilt_angle'][i] =
control_constants['blind_tilt_angle'][original_index]
            # During unoccupied hours
            if 12 <= weather_data['decimal hour'][i] <= 14 or 17 <
weather_data['decimal hour'][i] <=23 or 0 <= weather_data['decimal hour'][i]
< 8:
                # intermediate arrays creation
```

```
                temp_transmittance =
np.zeros(len(control_constants['blind_tilt_angle']))
                temp_transmitted_daylight =
np.zeros(len(control_constants['blind_tilt_angle']))
                temp_Ev =
np.zeros(len(control_constants['blind_tilt_angle']))
                temp_Ep =
np.zeros(len(control_constants['blind_tilt_angle']))
                temp_DGPs =
np.zeros(len(control_constants['blind_tilt_angle']))
                temp_total_transmitted_daylight =
np.zeros(len(control_constants['blind_tilt_angle']))
                # looping through the tilt angles to find the optimal one
with the highest transmittance
                for idx, tilt in
enumerate(control_constants['blind_tilt_angle']):
                    if 0 <= tilt <= 45:
                        temp_transmittance[idx] =
((1/((2.32*10**13)*(np.sqrt(2.506628)))) * (np.exp((-0.5)*((tilt -
(2.38*10**13))/(2.32*10**13))**2))) * ((-
2.91*10**7)*weather_data['theta'][i]**3 +
(6.39*10**9)*weather_data['theta'][i]**2 + (-
6.63*10**9)*weather_data['theta'][i]  + (-1.73*10**11))
                    elif 45 < tilt <= 85:
                        temp_transmittance[idx] = np.maximum((((0.931)*((1 /
((2.95*10**8) * np.sqrt(2.506628))) * np.exp(-0.5 * ((tilt - (1.65*10**9)) /
(2.95*10**8))**2))) + \
                                                             ((1-0.931)*((1 /
((2.19*10**8) * np.sqrt(2.506628))) * np.exp(-0.5 * ((tilt - (7.28*10**8)) /
(2.19*10**8))**2)))) * \
                                                             ((-6.57*10**7) *
weather_data['theta'][i]**3 + (4.19*10**9) * weather_data['theta'][i]**2 + (-
6.36*10**10) * weather_data['theta'][i] + (1.85*10**11)),0)
                    elif tilt == 90:
                        temp_transmittance[idx] = 0
                    temp_transmitted_daylight[idx] =
clear_transmitted_daylight_f(temp_transmittance[idx],
weather_data['alpha'][i] ,  weather_data['n'][i] ,  weather_data['theta'][i]
, final_data['outer_transmittance'][i])
                    temp_total_transmitted_daylight[idx] =
temp_transmitted_daylight[idx] + final_data['middle_transmitted_daylight'][i]
                    #radiosity matrix
                    M0 = np.zeros([9 ,
len(control_constants['blind_tilt_angle'])])
                    for m in range
(len(control_constants['blind_tilt_angle'])):
                        for l in range(9):
                            if l == 0:
                                M0[l][m] = temp_transmitted_daylight[m]
                            elif l == 1:
                                M0[l][m] =
final_data['middle_transmitted_daylight'][i]
                            elif l == 2:
```

```
                                M0[l][m] = temp_total_transmitted_daylight[m]
                            else:
                                M0[l][m] = 0
                    M = cal_M(M0 , F, control_constants['rho'])
                    for k in range(len(M[0])):
                        temp_Ep[k] = f[0]*M[0][k] + f[1]*M[1][k] +
f[2]*M[2][k] + f[3]*M[3][k] + f[4]*M[4][k] + f[5]*M[5][k] + f[6]*M[6][k] +
f[7]*M[7][k] + f[8]*M[8][k]
                        temp_E_ceiling =  F[7][0]*M[0][k] + F[7][1]*M[1][k] +
F[7][2]*M[2][k] + F[7][3]*M[3][k] + F[7][4]*M[4][k] + F[7][5]*M[5][k]
                        + F[7][6]*M[6][k] + F[7][7]*M[7][k] + F[7][8]*M[8][k]
                        temp_E_floor = F[4][0]*M[0][k] + F[4][1]*M[1][k] +
F[4][2]*M[2][k] + F[4][3]*M[3][k] + F[4][4]*M[4][k] + F[4][5]*M[5][k]
                        + F[4][6]*M[6][k] + F[4][7]*M[7][k] + F[4][8]*M[8][k]
                        temp_E_westwall = F[6][0]*M[0][k] + F[6][1]*M[1][k] +
F[6][2]*M[2][k] + F[6][3]*M[3][k] + F[6][4]*M[4][k] + F[6][5]*M[5][k]
                        + F[6][6]*M[6][k] + F[6][7]*M[7][k] + F[6][8]*M[8][k]
                        temp_E_northwall = F[8][0]*M[0][k] + F[8][1]*M[1][k]
+ F[8][2]*M[2][k] + F[8][3]*M[3][k] + F[8][4]*M[4][k] + F[8][5]*M[5][k]
                        + F[8][6]*M[6][k] + F[8][7]*M[7][k] + F[8][8]*M[8][k]
                        temp_E_window1 = F[0][0]*M[0][k] + F[0][1]*M[1][k] +
F[0][2]*M[2][k] + F[0][3]*M[3][k] + F[0][4]*M[4][k] + F[0][5]*M[5][k]
                        + F[0][6]*M[6][k] + F[0][7]*M[7][k] + F[0][8]*M[8][k]
                        temp_E_window2 = F[1][0]*M[0][k] + F[1][1]*M[1][k] +
F[1][2]*M[2][k] + F[1][3]*M[3][k] + F[1][4]*M[4][k] + F[1][5]*M[5][k]
                        + F[1][6]*M[6][k] + F[1][7]*M[7][k] + F[1][8]*M[8][k]
                        temp_E_southwall = F[3][0]*M[0][k] + F[3][1]*M[1][k]
+ F[3][2]*M[2][k] + F[3][3]*M[3][k] + F[3][4]*M[4][k] + F[3][5]*M[5][k]
                        + F[3][6]*M[6][k] + F[3][7]*M[7][k] + F[3][8]*M[8][k]
                        temp_Ev[k] = (temp_E_ceiling / 2) + (temp_E_floor /
2) + (temp_E_westwall/2) + (temp_E_northwall / 2) + (temp_E_window1/2) +
(temp_E_window2 / 2) + (temp_E_southwall / 2)
                        temp_DGPs[k] = float(6.22*10**-5 * temp_Ev[k] +
0.184)
                index = np.argmax(temp_Ep)
                final_data['Ep'][i] = temp_Ep[index]
                final_data['DGPs'][i] = temp_DGPs[index]
                final_data['transmittance'][i] = temp_transmittance[index]
                final_data['transmitted_daylight'][i] =
temp_transmitted_daylight[index]
                final_data['total_transmitted_daylight'][i] =
temp_total_transmitted_daylight[index]
                final_data['optimal_tilt_angle'][i] =
control_constants['blind_tilt_angle'][index]
        # Cloudy time step (occupancy is not important)
        elif weather_data['cloud_cover'][i] > 4:
            final_data['middle_transmitted_daylight'][i] =
middle_cloudy_transmitted_daylight_f(weather_data['alpha'][i],
final_data['middle_transmittance'][i])
            # intermediate arrays creation
            temp_transmittance =
np.zeros(len(control_constants['blind_tilt_angle']))
```

```
            temp_transmitted_daylight =
np.zeros(len(control_constants['blind_tilt_angle']))
            temp_Ev = np.zeros(len(control_constants['blind_tilt_angle']))
            temp_Ep = np.zeros(len(control_constants['blind_tilt_angle']))
            temp_DGPs = np.zeros(len(control_constants['blind_tilt_angle']))
            temp_total_transmitted_daylight =
np.zeros(len(control_constants['blind_tilt_angle']))
            for idx, tilt in
enumerate(control_constants['blind_tilt_angle']):
                temp_transmittance[idx] = ((4.231*10**12 *tilt**-
6.58)/(np.exp(3.752*10**2/tilt)-1))*(0.45* weather_data['theta'][i] + 0.9773)
                temp_transmitted_daylight[idx] =
cloudy_transmitted_daylight_f(weather_data['alpha'][i],
temp_transmittance[idx], tilt, final_data['outer_transmittance'][i])
                temp_total_transmitted_daylight[idx] =
temp_transmitted_daylight[idx] + final_data['middle_transmitted_daylight'][i]
                #radiosity matrix
                M0 = np.zeros([9 ,
len(control_constants['blind_tilt_angle'])])
                for m in range (len(control_constants['blind_tilt_angle'])):
                    for l in range(9):
                        if l == 0:
                            M0[l][m] = temp_transmitted_daylight[m]
                        elif l == 1:
                            M0[l][m] =
final_data['middle_transmitted_daylight'][i]
                        elif l == 2:
                            M0[l][m] = temp_total_transmitted_daylight[m]
                        else:
                            M0[l][m] = 0
                M = cal_M(M0 , F, control_constants['rho'])
                for k in range(len(M[0])):
                    temp_Ep[k] = f[0]*M[0][k] + f[1]*M[1][k] + f[2]*M[2][k] +
f[3]*M[3][k] + f[4]*M[4][k] + f[5]*M[5][k] + f[6]*M[6][k] + f[7]*M[7][k] +
f[8]*M[8][k]
                    temp_E_ceiling =  F[7][0]*M[0][k] + F[7][1]*M[1][k] +
F[7][2]*M[2][k] + F[7][3]*M[3][k] + F[7][4]*M[4][k] + F[7][5]*M[5][k]
                    + F[7][6]*M[6][k] + F[7][7]*M[7][k] + F[7][8]*M[8][k]
                    temp_E_floor = F[4][0]*M[0][k] + F[4][1]*M[1][k] +
F[4][2]*M[2][k] + F[4][3]*M[3][k] + F[4][4]*M[4][k] + F[4][5]*M[5][k]
                    + F[4][6]*M[6][k] + F[4][7]*M[7][k] + F[4][8]*M[8][k]
                    temp_E_westwall = F[6][0]*M[0][k] + F[6][1]*M[1][k] +
F[6][2]*M[2][k] + F[6][3]*M[3][k] + F[6][4]*M[4][k] + F[6][5]*M[5][k]
                    + F[6][6]*M[6][k] + F[6][7]*M[7][k] + F[6][8]*M[8][k]
                    temp_E_northwall = F[8][0]*M[0][k] + F[8][1]*M[1][k] +
F[8][2]*M[2][k] + F[8][3]*M[3][k] + F[8][4]*M[4][k] + F[8][5]*M[5][k]
                    + F[8][6]*M[6][k] + F[8][7]*M[7][k] + F[8][8]*M[8][k]
                    temp_E_window1 = F[0][0]*M[0][k] + F[0][1]*M[1][k] +
F[0][2]*M[2][k] + F[0][3]*M[3][k] + F[0][4]*M[4][k] + F[0][5]*M[5][k]
                    + F[0][6]*M[6][k] + F[0][7]*M[7][k] + F[0][8]*M[8][k]
                    temp_E_window2 = F[1][0]*M[0][k] + F[1][1]*M[1][k] +
F[1][2]*M[2][k] + F[1][3]*M[3][k] + F[1][4]*M[4][k] + F[1][5]*M[5][k]
                    + F[1][6]*M[6][k] + F[1][7]*M[7][k] + F[1][8]*M[8][k]
```

```
                    temp_E_southwall = F[3][0]*M[0][k] + F[3][1]*M[1][k] +
F[3][2]*M[2][k] + F[3][3]*M[3][k] + F[3][4]*M[4][k] + F[3][5]*M[5][k]
                    + F[3][6]*M[6][k] + F[3][7]*M[7][k] + F[3][8]*M[8][k]
                    temp_Ev[k] = (temp_E_ceiling / 2) + (temp_E_floor / 2) +
(temp_E_westwall) + (temp_E_northwall / 2) + (temp_E_window1) +
(temp_E_window2 / 2) + (temp_E_southwall / 2)
                    temp_DGPs[k] = float(6.22*10**-5 * temp_Ev[k] + 0.184)
            index = np.argmax(temp_Ep)
            final_data['Ep'][i] = temp_Ep[index]
            final_data['DGPs'][i] = temp_DGPs[index]
            final_data['transmittance'][i] = temp_transmittance[index]
            final_data['transmitted_daylight'][i] =
temp_transmitted_daylight[index]
            final_data['total_transmitted_daylight'][i] =
temp_total_transmitted_daylight[index]
            final_data['optimal_tilt_angle'][i] =
control_constants['blind_tilt_angle'][index]
        # Excluding unnecessary data
        if weather_data['decimal hour'][i] <= 8  or weather_data['decimal
hour'][i] >= 18:
            final_data['transmitted_daylight'][i] = 0
            final_data['optimal_tilt_angle'][i] = 0
            final_data['transmittance'][i] = 0
            final_data['middle_transmitted_daylight'][i] = 0
            final_data['Ep'][i] = 0
            final_data['DGPs'][i] = 0
            final_data['total_transmitted_daylight'][i] = 0

main()
```